Cell Reports
Methods

Article

Detection of fluorescent protein mechanical switching *in cellulo*

Graphical abstract

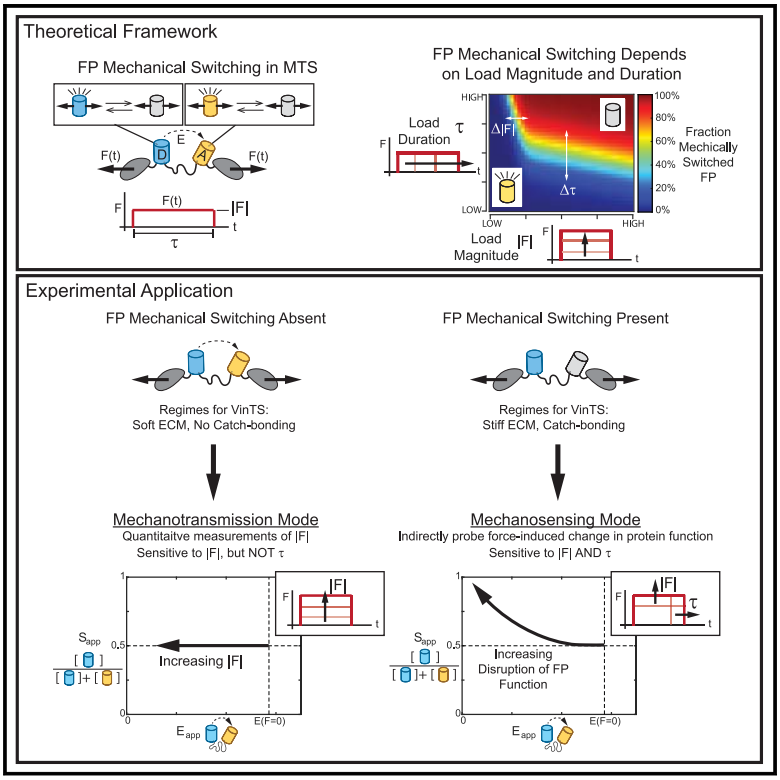

Highlights

- An approach to probe the effect of cellular forces on fluorescent protein (FP) function
- FP function is sensitive to load magnitude and dynamics (e.g., duration)
- FP function in biosensors is affected by bond dynamics and substrate stiffness
- Force-induced changes in FP function can be used to indirectly probe mechanosensing

Authors

T. Curtis Shoyer, Kasie L. Collins, Trevor R. Ham, ..., Benjamin A. Johns, Jennifer L. West, Brenton D. Hoffman

Correspondence

brenton.hoffman@duke.edu

In brief

Shoyer et al. develop an approach to probe how mechanical forces affect the function of fluorescent proteins inside living cells and leverage it to study mechanosensitive molecular processes. Fluorescent protein mechanical switching is manipulated by perturbations to force-activate bonds and substrate stiffness, consistent with its sensitivity to protein loading dynamics.

Shoyer et al., 2024, Cell Reports Methods *4*, 100815
July 15, 2024
https://doi.org/10.1016/j.crmeth.2024.100815

CellPress

Cell Reports Methods

CellPress
OPEN ACCESS

Article

Detection of fluorescent protein mechanical switching *in cellulo*

T. Curtis Shoyer,[1,4] Kasie L. Collins,[2,4,5] Trevor R. Ham,[1,4,6] Aaron T. Blanchard,[1] Juilee N. Malavade,[1,7] Benjamin A. Johns,[1] Jennifer L. West,[1,3] and Brenton D. Hoffman[1,8,*]

[1]Department of Biomedical Engineering, Duke University, Durham NC 27708, USA
[2]Department of Chemistry, Duke University, Durham NC 27708, USA
[3]Department of Biomedical Engineering, University of Virginia, Charlottesville, VA 22908, USA
[4]These authors contributed equally
[5]Present address: Georgia Institute of Technology, Atlanta, GA 30332, USA
[6]Present address: Atlantic Fish Company, Research Triangle Park, NC 27607, USA
[7]Present address: DeciBio, Los Angeles, CA 90067, USA
[8]Lead contact
*Correspondence: brenton.hoffman@duke.edu
https://doi.org/10.1016/j.crmeth.2024.100815

MOTIVATION Cells sense mechanical cues via force-induced alterations in protein structure and function, but elucidation of the molecular mechanisms is hindered by the lack of approaches to probe the effect of forces on protein structure and function inside cells. Motivated by *in vitro* observations of reversible fluorescent protein mechanical switching, we developed an approach for detecting fluorescent protein mechanical switching *in cellulo*. This enables the visualization of force-sensitive protein function inside living cells.

SUMMARY

The ability of cells to sense and respond to mechanical forces is critical in many physiological and pathological processes. However, determining the mechanisms by which forces affect protein function inside cells remains challenging. Motivated by *in vitro* demonstrations of fluorescent proteins (FPs) undergoing reversible mechanical switching of fluorescence, we investigated whether force-sensitive changes in FP function could be visualized in cells. Guided by a computational model of FP mechanical switching, we develop a formalism for its detection in Förster resonance energy transfer (FRET)-based biosensors and demonstrate its occurrence *in cellulo* within a synthetic actin crosslinker and the mechanical linker protein vinculin. We find that *in cellulo* mechanical switching is reversible and altered by manipulation of cell force generation, external stiffness, and force-sensitive bond dynamics of the biosensor. This work describes a framework for assessing FP mechanical stability and provides a means of probing force-sensitive protein function inside cells.

INTRODUCTION

The ability of cells to sense and respond to mechanical forces is critical in many developmental and physiological processes, and its dysregulation is involved in the progression of several disease states, including fibrosis and cancer.[1] To sense mechanical stimuli, cells must convert forces into biochemically detectable signals, which occurs through a multi-step molecular process.[1–4] Forces are first transmitted across specific proteins (termed mechanotransmission). This results in force-induced changes in protein structure and function (termed mechanosensing), such as the unfolding of a domain to expose a cryptic binding site.[3] Such protein conformational changes are then recognized biochemically (termed mechanotransduction), often through the binding/unbinding of transducer proteins. These new protein complexes drive downstream alterations in cell signaling and gene expression (termed mechanoresponse).[3] Despite significant progress in our understanding of the initial and final steps of this process, elucidating the molecular mechanisms of mechanosensing and mechanotransduction remains challenging.[1,5]

In vitro single-molecule techniques have provided a physical understanding of mechanosensitive molecular mechanisms. Using these techniques, the extension and unfolding of mechanosensitive protein domains, such as those in talin and α-catenin, as well as the subsequent binding of transducer proteins, such as vinculin, have been directly characterized.[6–8] However, determining where, when, and in which proteins these processes occur in cells is still challenging. Increased understanding of the spatiotemporal regulation of mechanosensitive processes

inside cells has largely come from the emergence of imaging techniques.[9] The development of molecular tension sensors (MTSs) to visualize loads across specific proteins inside cells has advanced our understanding of mechanotransmission, elucidating which proteins transmit loads and how these loads vary across biological contexts.[10] Progress in mechanosensing has been enabled by techniques to label unfolded protein domains via the binding of secondary probes, including antibodies that recognize the extended conformations of p130Cas or α-catenin,[11,12] and STReTCh (sensing tension by reactive tag characterization), which operates by the force-induced exposure of SpyTag and subsequent covalent binding of SpyCatcher.[13] Likewise, advances in mechanotransduction have been made by monitoring the localization of endogenous transducer proteins in response to molecular tension across a load-bearing protein.[14] However, labeling could affect protein function or compete with the binding of endogenous mechanotransducers, and these tools are often limited to fixation and/or depend on target protein-specific reagents that can be difficult to develop. Furthermore, these *in cellulo* techniques are based on the binding of a secondary probe (a synthetic marker or a labeled natural protein) to force-exposed domains, which conflates the steps of mechanotransduction and mechanosensing. Currently, there are no approaches analogous to *in vitro* techniques that can report mechanosensing (i.e., force-induced conformation changes in protein domains) inside cells.

To begin to address this technological gap, we asked whether the function of MTSs could be extended. MTSs were designed to measure the magnitude of loads on proteins (i.e., mechanotransmission). The largest class of MTSs used in cells are genetically encoded Förster resonance energy transfer (FRET)-based MTSs.[10,15] They consist of two fluorescent proteins (FPs) separated by an extensible linker domain.[16] Load across the MTS deforms the extensible linker domain, altering the distance between the FPs and the FRET efficiency. The FPs inside MTSs are also subject to loading, but their photophysical properties have been assumed to be force insensitive. However, recent *in vitro* experiments have demonstrated that GFP fluorescence can be switched on and off by cycles of mechanical loading.[17] This process is reversible and associated with an intermediate transition that is distinct from the complete unfolding or denaturation of the FP.[17,18] Therefore, FP mechanical switching is a reversible, force-sensitive transition between two structural/functional states. Additionally, FP mechanical switching is a kinetic process that inherently depends on both the magnitude and dynamics of loading (e.g., load duration or rate). This is important because both the magnitude and the dynamics of mechanical forces are known to drive mechanosensing by endogenous protein domains,[5,8,19–21] as well as cell-level responses to mechanical stimuli.[3,4] A properly functioning sensor of mechanotransmission will never accurately report the presence of mechanosensing. This is because the linker extends on a nearly instantaneous timescale, rendering the sensor's signals independent of load duration/dynamics. In contrast, FP mechanical switching, like force-induced conformational changes in mechanosensitive domains, responds to a combination of load magnitude and load duration/dynamics. We thus hypothesized that FP mechanical switching within an FRET-based MTS for a protein of interest could be used to indirectly probe if, when, and where mechanically similar domains within the protein of interest undergo force-induced conformational changes, without the need for fixation or secondary probe binding. At the same time, we also reasoned that the continued use and design of MTSs to measure mechanotransmission requires an understanding of FP mechanical switching.

Here, we investigated whether FP mechanical switching occurs inside cells. To create a physical framework, we first developed a kinetic model of FP mechanical switching in the context of FRET-based MTSs and then simulated expected experimental readouts. This revealed the effect of FP mechanical switching on FRET-based MTSs and predicted unique data signatures for the detection of FP mechanical switching *in cellulo*. Guided by this framework, we found that a synthetic actin-binding domain tension sensor (ABDTS) exhibited strong signatures of FP mechanical switching. The effect was reverted by pharmacological disruption of F-actin, indicating the reversibility of FP mechanical switching *in cellulo*. We also found less, but detectable, FP mechanical switching in a tension sensor for the mechanical linker protein vinculin (VinTS). FP mechanical switching in vinculin was sensitive to both manipulations of the vinculin-actin catch bond and mechanical stiffness of the external microenvironment. Together, this work describes an experimental paradigm for detecting the effect of mechanical loads on FP function in cells. This enables the visualization of force-dependent changes in FP structure/function, which can be leveraged to indirectly probe mechanosensitive processes *in cellulo* independent of secondary probe binding.

RESULTS

Development of a framework to assess FP mechanical switching *in cellulo*

To investigate FP mechanical switching in the context of fusion proteins in cells, we first considered a single FP within a load-bearing protein (Figure S1; Note S1, section II). Specifically, we modeled a load-bearing protein with a single FP in the line of loading subject to dynamic loading parameterized by a load magnitude F and a characteristic load duration τ. The load duration is governed by unbinding from the loading source with rate constant k_{unbind} (where $\tau \equiv 1/k_{unbind}$) (Figure S1A). The FP can reversibly switch between functional and non-functional states in a force-sensitive manner. Informed by single-molecule studies on the response of GFP to mechanical loading, FP mechanical switching is modeled as a two-step, sequential process (Figure S1B; Note S1, section II.A; Equation S1; and Table S1). The first step is a fast, near-equilibrium transition at a characteristic force,[22] which is permissive for the second step. The second step is a transition to a non-fluorescent state, which is described by a Bell model force-dependent rate constant.[17] The kinetics of this second step are expected to be slower and a potential source of non-equilibrium effects (e.g., loading rate or load duration dependence). As a large number of FPs with different structures, photophysical properties, and mechanical stabilities exist, and the integration of FPs into fusion proteins in the cellular environment can alter these properties, we assessed the extent of FP mechanical switching over a large

parameter space.[16,22–24] The model identified regions of the mechanical switching parameter space where FP mechanical switching was likely or unlikely to occur as a function of the load magnitudes and durations estimated for protein loading in cells[10,25] (Figures S1C–S1O; Note S1, section II.B). These analyses indicate that FP mechanical switching is sensitive to changes in both load magnitude and load duration, suggesting that mechanical switching of an FP inside a load-bearing protein could, in principle, be suitable for indirectly probing if, when, and where the protein of interest supports mechanosensing.

To investigate the detection of FP mechanical switching in FRET-based MTSs, we had to extend the model of FP mechanical switching to an MTS, specify an imaging modality, and establish a framework for displaying the data. To mediate FRET, two FPs must have distinct photophysical properties, where one FP (the donor) can non-radiatively transfer energy to the other FP (the acceptor).[26] In our model, MTSs are subject to dynamic loading parameterized by a load magnitude F and a characteristic load duration τ, during which the acceptor and donor FP can reversibly switch between functional and non-functional states in force-sensitive manners (Figures 1A, 1B, and S2; Note S1, sections III.A.1–III.A2; Equations S4 and S5; Table S2). Therefore, within a population of MTSs, each sensor exists in one of four states: D1A1, D1A0, D0A1, and D0A0, where "D" represents the donor FP, "A" represents the acceptor FP, and "0" or "1" indicates whether an FP is in the non-fluorescent or fluorescent state, respectively (Figure 1C).

To understand how mechanical switching affects FRET measurements, we needed to select an imaging modality. As sensitized emission is the most widely used imaging modality for measuring FRET-based sensors *in cellulo*, we chose to focus on it.[27–29] In this approach, FRET-based sensors are imaged in three channels (DD: donor excitation, donor emission; DA: donor excitation, acceptor emission; AA: acceptor excitation, acceptor emission). Using calibration methods, the apparent FRET efficiency, E_{app}, and FP stoichiometry (abundance of donor relative to total FPs), S_{app}, can be computed from these images[27–29] (Figure 1D; Note S1, section III.A.3). E_{app} and S_{app} are calculated using the following equations[29]:

$$E_{app} = \frac{I_{DA,corr}}{I_{DA,corr}+\gamma^{M}\cdot I_{DD}} \quad \text{(Equation 1)}$$

$$S_{app} = \frac{I_{DA,corr}+\gamma^{M}\cdot I_{DD}}{I_{DA,corr}+\gamma^{M}\cdot I_{DD}+I_{AA}/\beta^{X}} \quad \text{(Equation 2)}$$

where I_{DD} is the intensity in the DD-channel, I_{AA} is the intensity in the AA-channel, $I_{DA,corr}$ is the intensity in the DA-channel corrected for donor bleedthrough and acceptor direct excitation, and γ^{M} and β^{X} are constants for calibrated measurements of three-channel FRET[27–29] (see Note S1, section III.A.3 and STAR Methods).

A framework for displaying FRET data based on two-dimensional histograms of E_{app} and S_{app} was recently developed to visualize and understand the effect of FP stoichiometry on three-channel FRET measurements.[29] For one-piece intramolecular FRET sensors, the ES-histogram framework provides a data quality control, as sensors with one donor and one acceptor FP should, by design, exhibit $S_{app} = 0.5$. Deviations indicate a lack of FP function due to photobleaching, maturation, or other processes. To investigate the detection and effects of FP mechanical switching in MTSs, we extended the ES-histogram framework to include the force-sensitive, continuously variable FRET signal of FRET-based MTSs and the mechanical switching of acceptor and donor FPs (Figures S3 and S4; Note S1, section III.B.1). Sensors in the D1A1 state (both FPs in the functional state) undergo intramolecular FRET with a FRET efficiency (E_0), which depends on the magnitude of molecular tension across the MTS, F, according to the FRET efficiency-force calibration, $E_0 = f(F)$, of the tension sensor module.[16,30] Here, the previously determined FRET efficiency-force calibration for the original tension sensor module (TSMod) (mTFP1-$(GPGGA)_8$-mVenus) was used to facilitate comparisons to experimental data in this work[16,30] (Figure 1E). To simulate three-channel FRET measurements analogous to experimental data, we considered the three-channel FRET signal contribution from each of the four states to determine E_{app} and S_{app} for a population of MTSs containing a specified number of sensors in each state (n_{D1A1}, n_{D1A0}, n_{D0A1}, n_{D0A0}) (Note S1, section III.A.3; Tables S3 and S4; Equations S12–S19).

To build intuition, we derived simplified expressions for an MTS population containing a specified number of sensors in each state in which all sensors are subject to constant loading at a magnitude, F:

$$E_{app} = \frac{E_0}{1+\left(\frac{n_{D1A0}}{n_{D1A1}}\right)} \quad \text{(Equation 3)}$$

$$S_{app} = \frac{n_{D1A1}+n_{D1A0}}{(n_{D1A1}+n_{D1A0})+(n_{D1A1}+n_{D0A1})} \quad \text{(Equation 4)}$$

where $E_0 = f(F)$ is the FRET efficiency-force calibration for sensors in the D1A1 state, and a non-zero number of sensors in the D1A1 state ($n_{D1A1} > 0$) is assumed. Equations 3 and 4 indicate how FP mechanical switching should affect three-channel FRET measurements of MTSs and quantitative estimates of molecular tension magnitude. In the absence of FP mechanical switching, all MTSs exist in the D1A1 state ($n_{D1A0} = n_{D0A1} = n_{D0A0} = 0$), so $E_{app} = E_0$ and $S_{app} = 0.5$. The resulting relationship $E_{app} = E_0$ indicates that quantitative measurements of molecular tension magnitude using the $E_0 = f(F)$ calibration are valid in the absence of FP mechanical switching. In the presence of FP mechanical switching, (E_{app}, S_{app}) curves can be constructed for MTS populations subject to the same load magnitude, F, and having variable amounts of acceptor-only (some D1A0) or donor-only (some D0A1) mechanical switching (referred to as tension isoclines; Figures 1F, S4C, and S4D; Note S1, section III.B.1). Increasing levels of acceptor mechanical switching move the data up/left with decreasing E_{app} coupled to increasing S_{app}. Increasing levels of donor mechanical switching move the data directly downward with decreasing S_{app}. These trends are consistent with the known effects of excess

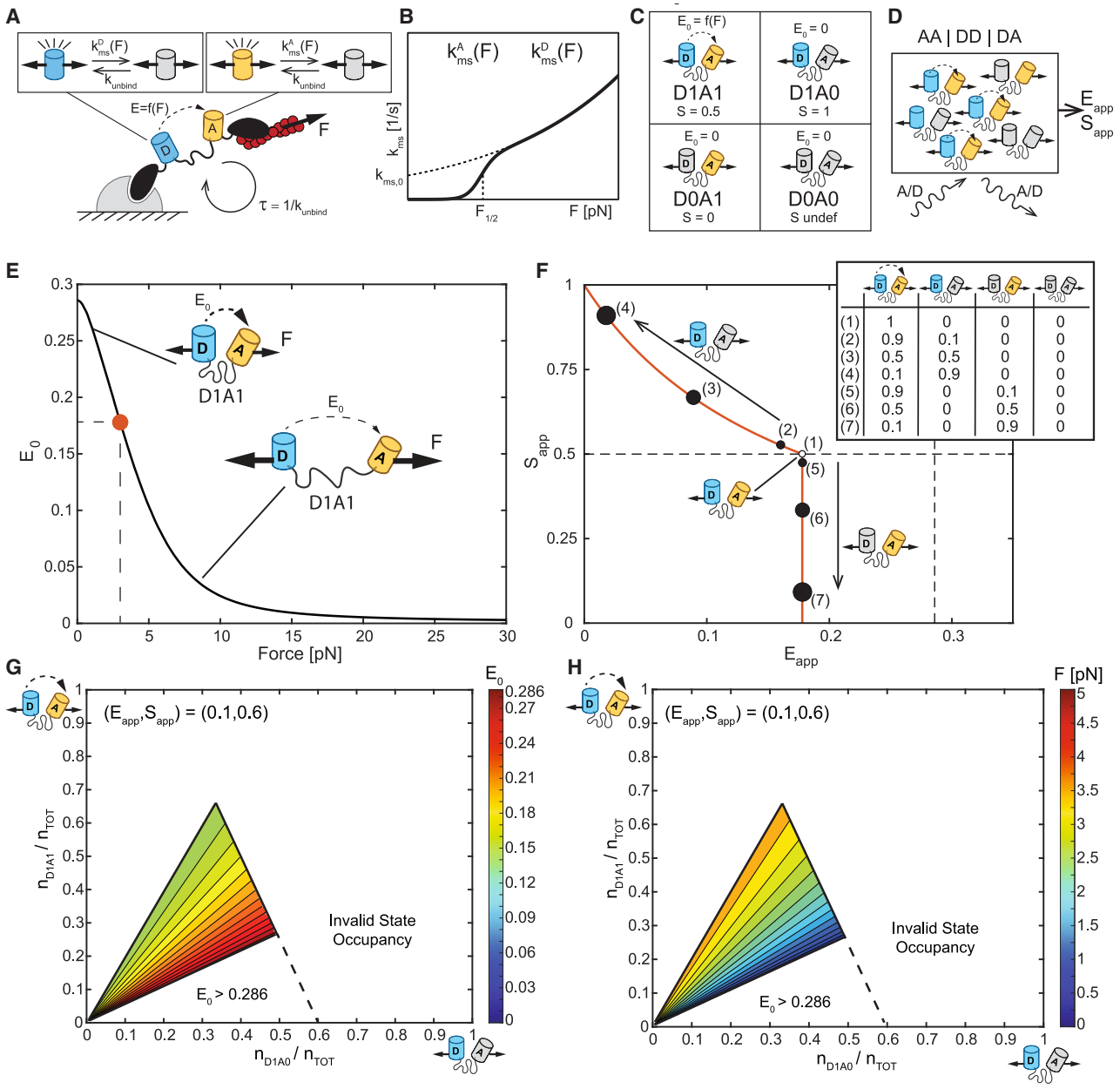

Figure 1. Framework for FP mechanical switching in FRET-based MTSs

(A and B) (A) Model of FP mechanical switching in MTSs. MTSs are subject to dynamic loading parameterized by a load magnitude F and a characteristic load duration τ, which is governed by unbinding from the loading source with rate constant k_{unbind}. Donor and acceptor FPs are in the line of loading and undergo FP mechanical switching with force-dependent rate constants $k^D_{MS}(F)$ and $k^A_{MS}(F)$. $k^D_{MS}(F)$ and $k^A_{MS}(F)$ have the same functional form, shown in (B), but different parameters.

(C) Four possible MTS states based on the status of the donor and acceptor FP. For each state, the FRET efficiency, E_0, and FP stoichiometry, S, are indicated.

(D) Schematic of 3-channel FRET measurements of a simulated population of MTSs.

(E) FRET efficiency-force calibration, $E_0 = f(F)$, for an MTS in the D1A1 state, with dot indicating F of 3 pN.

(F) Plot of S_{app} versus E_{app} containing the (E_{app}, S_{app}) curve for MTS populations subject to constant loading at magnitude F of 3 pN for cases of acceptor-only mechanical switching (varying amounts of D1A1 and D1A0 states) or donor-only mechanical switching (varying amounts of D1A1 and D0A1 states). The fraction of sensors in each state is indicated in the key.

(G) Contour plot of E_0 on the (fraction of sensors in D1A0 state, fraction of sensors in D1A1 state) plane demonstrating all E_0 values consistent with the single point (E_{app}, S_{app}) of (0.1, 0.6). White indicates regions with invalid state occupancies and/or E_0 values.

(H) Corresponding contour plot of F using the $E_0 = f(F)$ calibration in (E). Levels are in increments of 0.01 for (F) and 0.025 for (H).

The plots in (F)–(H) relate to Equations 3 and 4.

See also Note S1 and Figures S1–S4.

donors and acceptors, respectively, in other force-insensitive FRET-based biosensors.[29] In the presence of FP mechanical switching, quantitative measurements of molecular tension magnitude are not possible for two reasons. The first reason is, because both the acceptor and donor FPs can undergo mechanical switching, the actual occupancy of sensors in each of the possible four states (D1A1, D1A0, D0A1, and D0A0) cannot be uniquely determined from the experimentally measurable quantities (E_{app} and S_{app}). In the presence of FP mechanical switching, a single (E_{app}, S_{app}) data point is consistent with many possible values of E_0, and hence, F (demonstrated for an example data point in Figures 1G and 1H). Therefore, $E_{app} \neq E_0$, and quantitative measurements of molecular tension magnitude are invalidated. We note that formalisms assuming donor-only or acceptor-only mechanical switching would reduce the number of unknowns, but we are hesitant to utilize such approaches at this time. It is challenging to experimentally eliminate the possibility of donor mechanical switching in the presence of acceptor mechanical switching (or vice versa) because sensors harboring two non-fluorescent FPs are not optically detectable. The second reason is that FP mechanical switching is more likely at higher versus lower tension magnitudes, which could bias measurements of tension magnitude distributions (Note S1, section VI). Overall, $E_{app} = E_0$, which is required for quantitative measurements of molecular tension magnitude, can only be assumed in the absence of both acceptor and donor mechanical switching, which is confirmed via the ES-histogram by confirming that $S_{app} \sim 0.5$ across the full range of E_{app} values.

We next assessed the suitability of the ES-histogram framework for detecting FP mechanical switching in MTSs that undergo dynamic binding, loading, and unbinding (Note S1, sections III.B.2–III.B.5 and IV). We first asked how the three-channel FRET signals for MTSs with FP mechanical switching responded to variations in load magnitude at constant load duration or variations in load duration at constant load magnitude. To do so, we simulated three-channel FRET measurements for populations of MTSs subject to variations in load magnitude F or load duration τ with no (Figures 2A and 2B), acceptor-only (Figures 2C and 2D), or donor-only mechanical switching (Figures 2E and 2F). In the absence of FP mechanical switching, the MTS responds only to variations in load magnitude (Figure 2A) and is not sensitive to variations in load duration (Figure 2B). Therefore, in the absence of mechanical switching, an MTS functions according to the original design intention—in other words, as a quantitative probe for mechanotransmission ($E_{app} = E_0$) due to the extension of the deformable linker domain within the tension sensor module. In the presence of acceptor or donor mechanical switching, the sensor now responds to both variations in load magnitude (Figures 2C, 2E, S7C, and S7D; Note S1, section III.B.4) and load duration (Figures 2D, 2F, S7A, and S7B; Note S1, section III.B.4). Therefore, the ES-histogram provides additional information, indicating force-sensitive changes in FP structure/function resulting from the loading dynamics of the protein of interest that contains the MTS. However, contributions from load magnitude and duration cannot be decoupled from the ES-histogram (Figures S7 and S9; Note S1, sections III.B.4 and IV), and quantitative measurements of molecular tension magnitude are no longer possible ($E_{app} \neq E_0$).

Lastly, we generated signatures for all cases of FP mechanical switching that would be analogous to experimental data, where both the load magnitudes and durations vary. To do so, we simulated three-channel FRET measurements for populations of MTSs subject to variations in both load magnitude F and characteristic load duration τ that exhibit no (Figure 3A), acceptor-only (Figure 3B), donor-only (Figure 3C), or both donor and acceptor (Figure 3D) mechanical switching. In the absence of FP mechanical switching, both acceptor and donor FPs are functional (D1A1 state), and the data are distributed along $S_{app} = 0.5$ and $E_{app} = E_0$ (Figure 3A). Thus, the spread in E_{app} is solely due to the extension of the deformable linker domain within the tension sensor module, and load magnitudes can be accurately inferred. FP mechanical switching results in deviations in S_{app} from 0.5. Increased acceptor mechanical switching increases S_{app} and decreases E_{app}, resulting in an up/left-slanting data signature (Figure 3B). This trend is observed for a wide range of FP mechanical switching parameters and is distinct from constitutive acceptor loss of function (e.g., due to photobleaching or large differences in FP maturation time [Figure S5; Note S1, section III.B.2]). Increased donor mechanical switching decreases S_{app}, with larger effects at lower E_{app} values, resulting in a down/left-slanting data signature (Figure 3C). This trend is conserved for a wide range of FP parameters and is distinct from constitutive donor loss of function (e.g., due to photobleaching or large differences in FP maturation time [Figure S6; Note S1, section III.B.3]). Lastly, we considered when both acceptor and donor FPs undergo mechanical switching. If the acceptor and donor exhibit identical FP mechanical switching kinetics, then S_{app} values deviate from 0.5 positively and negatively (Figure 3D), producing a signature that is distinct from cases where one or both FPs lack mechanical switching. In the case where both FPs undergo mechanical switching but with non-identical parameters, dominant mechanical switching of acceptor or donor remains detectable in the presence of lower levels of mechanical switching in the other species (Figure S8; Note S1, section III.B.5). Therefore, we conclude that minor and substantial FP mechanical switching in either donor and/or acceptor FPs in response to diverse aspects of mechanical loading are detectable using the ES-histogram framework.

Taken together, these analyses demonstrate the effect of FP mechanical switching on three-channel FRET measurements of MTSs, predict unique data signatures for the detection of FP mechanical switching *in cellulo*, and indicate that additional information related to loading dynamics/duration can be obtained from FP mechanical switching in MTSs.

Synthetic actin-binding tension sensor exhibits FP mechanical switching *in cellulo*

Next, we investigated whether FP mechanical switching could be detected *in cellulo*. To begin, we sought to assess this with a structurally simple MTS that is loaded directly by the actin cytoskeleton and is not subject to biochemical regulation. Therefore, we created the synthetic ABDTS by attaching the F-actin binding domain F-tractin[31,32] to both ends of the original TSMod,[30] which is composed of mTFP1-$(GPGGA)_8$-mVenus (Figure 4H). This sensor is anticipated to act like an actin cross-linking protein and report forces that promote the relative translocation of two

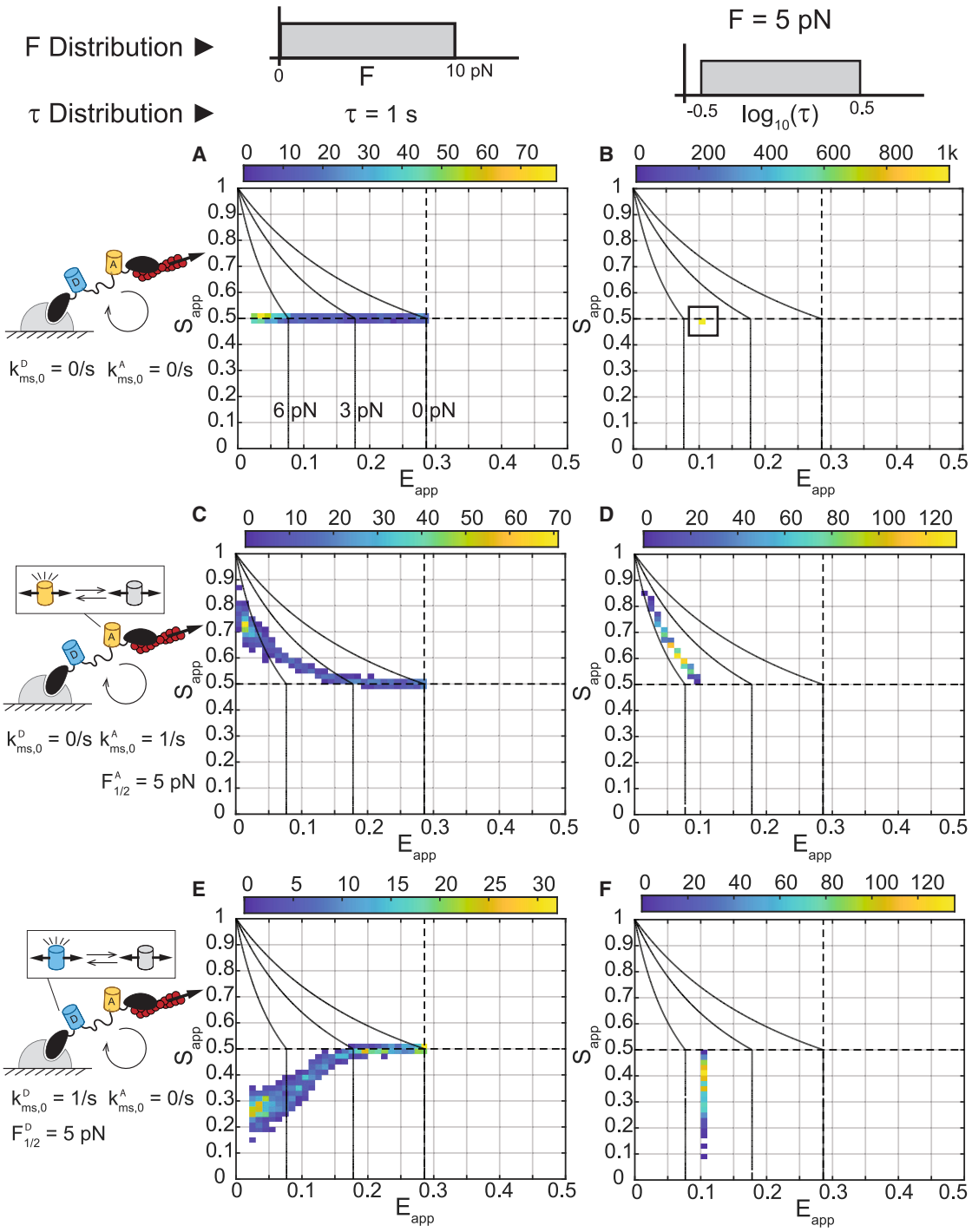

Figure 2. Response of MTSs to variation in load magnitude or load duration

(A–F) ES-histograms for 1,000 simulated populations of MTSs subject to a (A, C, and E) load magnitude (F) drawn from a uniform distribution between 0 and 10 pN and a characteristic load duration (τ) of 1 s, or (B, D, and F) F of 5 pN and τ drawn from a log-uniform distribution from $10^{-0.5}$ to $10^{0.5}$ s for cases of (A and B) no FP mechanical switching, (C and D) acceptor mechanical switching only, or (E and F) donor mechanical switching only, according to base model parameters given in Note S1 and Table S2. Each MTS population comprises 50 sensors having the same FP parameters, F values, and τ values. The color bars indicate bin counts. In all plots, reference black lines are tension isoclines for acceptor-only or donor-only mechanical switching at F of 0, 3, and 6 pN (from right to left).
See also Note S1 and Figures S5–S12.

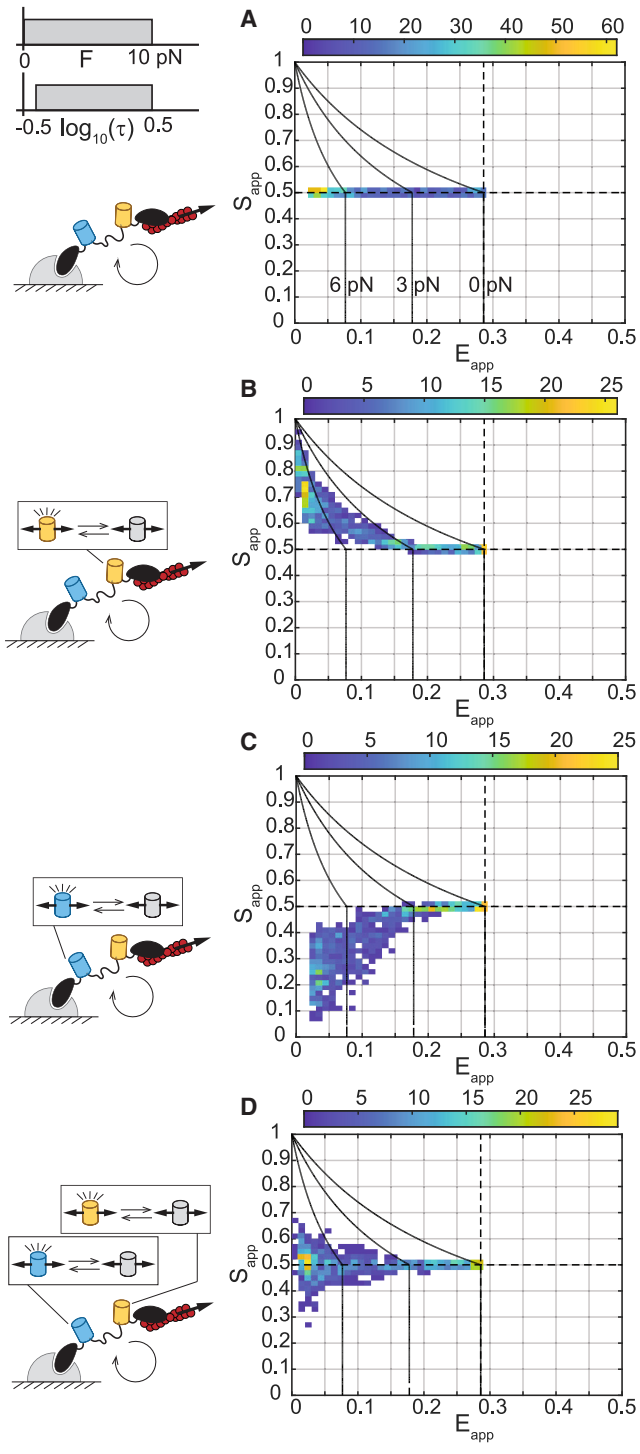

Figure 3. Data signatures of FP mechanical switching in MTSs

(A–D) ES-histograms for 1,000 simulated populations of MTSs subject to a load magnitude (F) drawn from a uniform distribution between 0 and 10 pN and a characteristic load duration (τ) drawn from a log-uniform distribution from $10^{-0.5}$ to $10^{0.5}$ s for cases of (A) no FP mechanical switching, (B) acceptor mechanical switching only, (C) donor mechanical switching only, or (D) identical acceptor and donor mechanical switching, according to base model parameters given in Note S1 and Table S2. Each MTS population comprises 50 sensors having the same FP parameters, F values, and τ values. The color bars indicate bin counts. In all plots, reference black lines are tension isoclines for acceptor-only or donor-only mechanical switching at F of 0, 3, and 6 pN (from right to left).

See also Note S1 and Figures S5–S12.

cross-linked F-actin filaments. As an unloaded control, we used a version containing a single F-tractin domain (ABDTL, actin-binding domain tailless control) (Figure 4A). We performed three-channel FRET imaging of these constructs in NIH3T3 cells. F-tractin reversibly binds filamentous actin (F-actin), while having a low affinity for monomeric actin.[31,33] F-tractin has been shown to localize to F-actin networks in the lamellipod, lamellum, and cortex, and to stress fibers in many cell types.[32] Consistent with this, both constructs localized to stress fibers and F-actin networks at the cell edge in NIH3T3 cells (Figures 4B–4D and 4I–4K). However, it should be noted that the acceptor signal can only provide a quantitative estimate of sensor concentration in the absence of acceptor mechanical switching, which can only be assumed by design for ABDTL.

ABDTL exhibited a spatially uniform FRET efficiency of ~0.285, corresponding to the unloaded value for TSMod,[28] and stoichiometry of ~0.5 (Figures 4E, 4F, S13A, and S13B; note that all experimental FRET measurements are inherently apparent FRET efficiency and FP stoichiometry, but are indicated as E and S without the subscript to match previous conventions[16,27,28,34]). Both E and S had no dependence on acceptor intensity, an estimate of ABDTL concentration, and E did not exceed the unloaded value for TSMod across the full concentration range (Figures S14A, S14C, and S14E), supporting an absence of intermolecular FRET due to the bystander effect in the actin-binding sensor system at the expression levels used here. ES-histograms of single cells expressing ABDTL and the whole-cell population contained a single major density centered on $E \sim 0.285$ and $S \sim 0.5$ (Figures 4G and 4O), resembling the predicted signature for an unloaded MTS with no FP mechanical switching from the model (Figure S4B). The increased spread in the ABDTL data (Figures 4G and 4O) compared to the theoretical prediction (Figure S4B) likely arises from experimental noise in live cells, such as due to height variations, local differences in index of refraction, different pHs in various sub-cellular compartments, or small differences in E_{app} and S_{app} as the protein is produced/degraded. Additionally, the imaging and FRET correction process introduce and propagate noise in the system. This variation is common in FRET imaging data,[16,26,28,29] and similar variations have been reported previously for the unloaded cytoplasmic TSMod.[28] Together, these data confirmed proper function of ABDTL as an unloaded control.

ABDTS exhibited regions of lower FRET efficiency ($E < 0.285$) and higher stoichiometry ($S > 0.5$) (Figures 4L–4M), consistent with the presence of acceptor mechanical switching. Regions of low E and high S were consistently near the cell edge in areas of positive curvature. E was closer to 0.285 and S was closer to 0.5 in the center of the cells and within stress fibers (Figures S13C and S13D). This suggests that loading and FP mechanical switching in ABDTS occurs most strongly in lamellar actin networks, where actin filaments may be more likely to move relative to one another. The lack of loading in stress fibers is possibly due

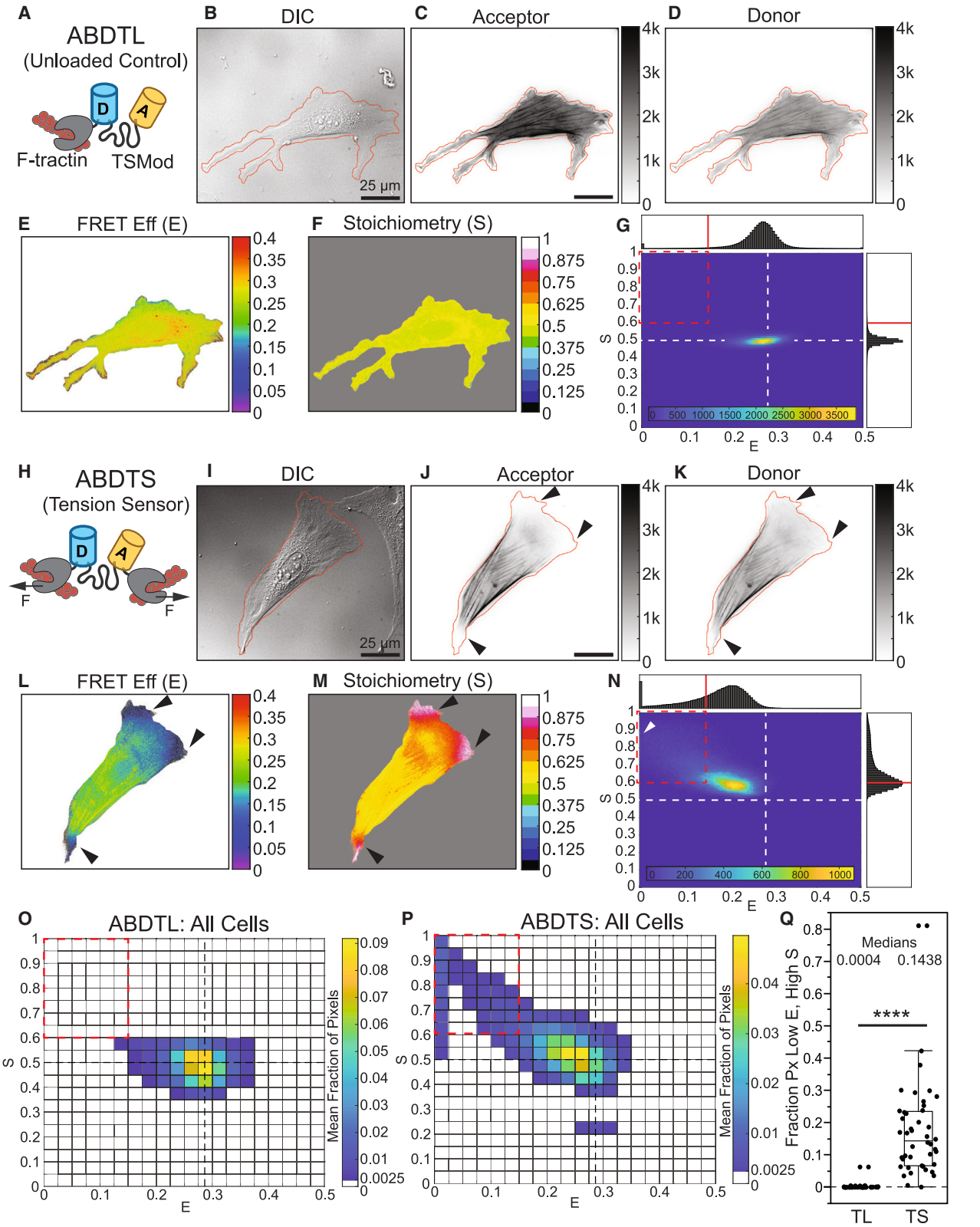

(legend on next page)

to differences in the density, alignment, or relative motion of F-actin in these structures[35,36] and/or issues related to the size of the sensor. At the edge of the cell, we observed that the acceptor signal was nearly completely lost, while the donor signal was only partially reduced (Figures S13E–S13H). We verified that these patterns were not due to an ABDTS-induced alteration in, or loss of, F-actin in these regions by fixing and labeling ABDTL- and ABDTS-expressing cells with phalloidin (Figures S15A–S15J). We also assessed the relationship between E or S and acceptor intensity, analogous to the analysis we performed on ABDTL (Figure S14). Importantly, in the presence of FP mechanical switching, the acceptor intensity is no longer an estimate of sensor concentration. At the lowest acceptor intensities, E was lowest and S was highest, further supporting that regions of low E and high S were due to acceptor mechanical switching (Figures S14B, S14D, and S14F). ES-histograms of a single cell (Figure 4N) and the whole-cell population (Figure 4P) contained a major up/left-slanting density extending to lower FRET efficiencies ($E < 0.285$) and higher stoichiometries ($S > 0.5$). These data resemble the predicted signature of a loaded MTS with dominant acceptor mechanical switching from the model (Figure 3B). The spread in the ABDTS experimental data (Figures 4N and 4P) compared to the theoretical prediction (Figure 3B) likely arises from the increased complexity of a cellular environment (e.g., unknown and spatially variable load magnitudes, loading durations, and load rates) as well as experimental noise, which is inherent in FRET imaging data.[16,26,28,29] Furthermore, at the lowest FRET efficiency values ($E \sim 0$–0.025, coming mainly from pixels at the very edge of the cell), the ES-histogram had a wider range of S spanning between 0.5 and 1. This resembles the biphasic trends observed in the model for two different mechanisms: (1) acceptor mechanical switching with a lower force threshold combined with donor mechanical switching with a higher force threshold (Figure S8C; Note S1, section III.B.5), or (2) acceptor mechanical switching with force-induced unbinding (Figures S10H and S10K; Note S1, section V.B.1). Our observation of partial loss of donor signal (in addition to near-complete loss of acceptor signal) at the very edge of ABDTS- but not ABDTL-containing cells (Figures S13E–S13H) supports the first explanation. To quantitatively compare ABDTS versus ABDTL, we computed the fraction of pixels in each cell in a low E, high S bin ($E < 0.15$, $S > 0.60$; cutoffs indicated by the red dashed box in Figures 4G and 4N–4P) and found that ABDTS had a significantly higher fraction of pixels than ABDTL (Figure 4Q). The trends in E and S for ABDTL and ABDTS were also not altered by fixation (Figures S15K–S15M). Together, these data indicate that FP mechanical switching occurs in ABDTS, with mechanical switching of mVenus (acceptor) being dominant over mTFP1 (donor).

To test the feasibility of mVenus and mTFP1 having different mechanical stabilities, we performed steered molecular dynamics (SMD) simulations on the two FPs, an approach previously applied to GFP.[18] In agreement with our experimental observations, we found that mTFP1 had a higher mechanical stability than mVenus in the SMD simulations (Figures S16–S18; Note S2; Videos S1, S2, and S3). This is broadly consistent with previous single-molecule experimental work showing that even FPs derived from the same species, GFP and enhanced yellow FP, have different mechanical stabilities *in vitro*.[22,23]

To determine whether acceptor mechanical switching in ABDTS was manipulable, we used latrunculin A to disrupt the actin cytoskeleton of fully spread cells containing ADBTL or ABDTS (Figure 5). Latrunculin A treatment caused no changes in ABDTL-expressing cells in comparison to the vehicle control (Figures 5A–5H), and the ES-histograms for vehicle versus latrunculin A treatment were similar for ABDTL-expressing cells (Figures 5Q and 5R). In comparison to vehicle treatment, latrunculin A treatment of ABDTS-expressing cells caused an increase in E toward 0.285 and a decrease in S toward 0.5 within the regions at the edge of the cell, indicating a reduction in acceptor mechanical switching (Figures 5I–5P). Comparisons of ES-histograms for vehicle versus latrunculin A-treated cells revealed that actin disruption caused a loss of density at low E, high S for ABDTS-expressing cells (Figures 5S and 5T). Furthermore, ES-histograms for latrunculin A-treated ABDTS-expressing cells resembled those for vehicle and latrunculin A-treated ABDTL-expressing cells (Figures 5Q, 5R, and 5T). Quantification revealed that latrunculin A-treated ABDTS-expressing cells had a significant reduction in the fraction of pixels in the low E, high S bin compared to vehicle exposed ABDTS-expressing cells and were not statistically different from latrunculin A-treated ABDTL-expressing cells (Figure 5U). Taken together, these data demonstrate the presence of reversible FP mechanical switching in a synthetic actin-binding sensor in living cells.

FP mechanical switching is detectable in vinculin tension sensor and is sensitive to force-activated bond dynamics and external stiffness

We next asked whether FP mechanical switching could be detected in an MTS within a naturally occurring protein. We focused on the mechanical linker protein vinculin, which couples the actin cytoskeleton to focal adhesions (FAs) to mediate adhesion

Figure 4. Synthetic actin-binding tension sensor exhibits FP mechanical switching *in cellulo*

(A) Schematic of ABDTL.

(B–G) Representative NIH3T3 cell expressing ABDTL, showing images of differential interference contrast (DIC) used to create cell outline, acceptor and donor intensities with cell outline overlaid in red, FRET efficiency and stoichiometry in cell mask, and ES-histogram of pixels in the cell.

(H) Schematic of ABDTS.

(I–N) Images and histogram for a representative NIH3T3 cell expressing ABDTS, analogous to those in (B)–(G). For single-cell ES-histograms in (G) and (N), the color bars indicate pixel counts.

(O and P) ES-histograms for whole-cell populations of ABDTL (O) and ABDTS (P), where color bars indicate the cell-averaged fraction of pixels in each bin ($N = 38/44$ cells for ABDTL/ABDTS over 5 experimental days).

(Q) Boxplot of fraction of pixels in each cell in the low E, high S bin ($E < 0.15, S > 0.60$) for ABDTL and ABDTS. The difference between the groups was detected using the Wilcoxon rank-sum test; $^{****}p < 0.0001$. p values are given in Note S3.

See also Figures S13–S15.

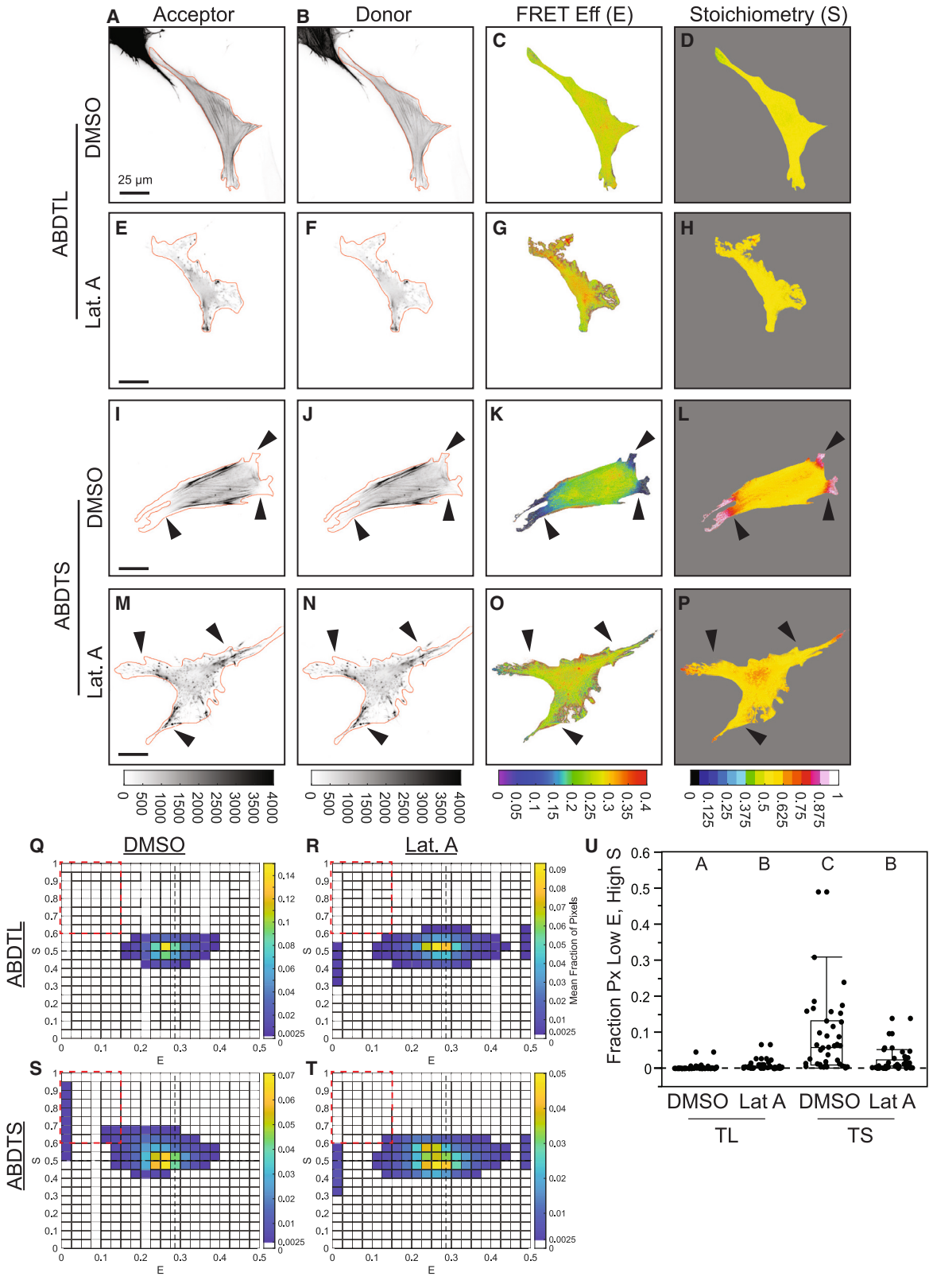

(legend on next page)

reinforcement and stiffness sensing.[30,37,38] We focused on vinculin because it has been widely studied with an existing tension sensor (VinTS),[2,10,14,16,39,40] and VinTS variants that unload vinculin[38,41] as well as progressively disrupt vinculin-actin catch-bonding[39] have been developed recently. Applying our framework, we re-analyzed existing datasets of VinTS and these mutants expressed in vinculin$^{-/-}$ mouse embryonic fibroblasts (MEFs).[38,39] As the tension-insensitive control, we used VinTS-I997A, which contains a point mutation that disrupts vinculin's binding to actin and has been shown to unload vinculin.[38,41] VinTS-I997A in FAs showed E corresponding to unloaded TSMod and S corresponding to no FP mechanical switching at both the single-cell (Figures 6A–6E and S19A–S19E) and cell population levels (Figure 6Z), as expected for a tension-insensitive control. In contrast, VinTS in FAs exhibited a spectrum of behaviors. At one end of this spectrum, VinTS in the FAs of some cells exhibited lower FRET efficiency ($E < 0.285$) with no apparent FP mechanical switching ($S \sim 0.5$) (Figures S19F–S19J), matching the model prediction for MTS loading without FP mechanical switching (Figure 3A). At the other end of this spectrum, VinTS in the FAs of other cells exhibited both a lower FRET efficiency ($E < 0.285$) and a higher stoichiometry ($S > 0.5$) with an up/left-sloping ES-histogram shape (Figures 6F–6J and S19K–S19O). This matches the prediction for MTS loading with acceptor mechanical switching (Figure 3B). Despite the cell-to-cell heterogeneity, the presence of mechanical switching in VinTS is also apparent at the cell population level (Figure 6Z). To quantify this, we again looked at the fraction of pixels in each cell in a low E, high S bin ($E < 0.15, S > 0.60$), indicating a significant difference between VinTS and VinTS-I997A (Figure 6AA). This is consistent with acceptor mechanical switching in VinTS but not in the unloaded VinTS-I997A.

To attempt to discern the origin of the heterogeneous responses in the VinTS data, we assessed whether acceptor mechanical switching in VinTS correlated with aspects of cell or FA morphology (Figure S20). We found no significant correlations with any of 10 distinct metrics, suggesting that individual aspects of cell or FA morphology do not explain the observed cell-to-cell variability. The heterogeneity could be due to cell-to-cell variability in vinculin phosphorylation levels, which have been shown to affect the ability of vinculin to bear loads and the turnover dynamics of vinculin as measured by FRAP,[37,40,42,43] but further work will be required to determine the basis of the heterogeneous responses in VinTS.

To probe the subcellular relationship between E and S, we examined large FAs that we previously reported to exhibit gradients in VinTS FRET efficiency.[16] We find that gradients in E along single FAs (lower at cell edge) were accompanied by gradients in S (higher at cell edge) (Figure S21). This indicates a gradient in acceptor mechanical switching in VinTS along single FAs (higher at cell edge). Thus, the previously reported[16] gradients in vinculin tension are more precisely described as gradients in vinculin tension magnitude and/or duration.

Force-activated bond dynamics play an important role in mechanosensitive processes at FAs,[2,4] and vinculin is known to form a strong catch bond with F-actin, whose duration increases with force up to a certain point.[44] Our modeling indicated that FP mechanical switching can be sensitive to changes in load duration (Figures 2, S1, and S7), as well as alterations to force-sensitive bond dynamics of the MTS (Figures S10 and S11; Note S1, section V). To assess whether manipulating vinculin catch-bonding affects FP mechanical switching, we re-analyzed the data of VinTS harboring single (VinTS-E1015A and VinTS-E1021A; Figures 6K–6T) and double (VinTS-E1015A-E1021A; Figures 6U–6Y) point mutations that were previously shown to progressively disrupt vinculin catch-bonding while retaining other key aspects of vinculin function.[39] The ES-histograms at both single-cell and cell population levels demonstrate that the acceptor mechanical switching signature of VinTS was partially reduced in the single mutants and completely eliminated in the double mutant, which is thought to greatly reduce or eliminate vinculin catch-bonding[39] (Figure 6Z). The fraction of pixels in the low E, high S bin ($E < 0.15$, $S > 0.60$) for VinTS-E1015A-E1021A was significantly lower than that for VinTS and was similar to VinTS-I997A (Figure 6AA), indicating an elimination of acceptor mechanical switching in the double mutant. However, while both VinTS-E1015A-E1021A and VinTS-I997A had no apparent FP mechanical switching ($S \sim 0.5$), the ES-histogram of VinTS-E1015A-E1021A was shifted to a slightly lower E than VinTS-I997A (Figure 6Z), consistent with the VinTS-E1015A-E1021A double mutant remaining partially loaded, as previously reported.[39] We also found that the double mutant (VinTS-E1015A-E1021A) exhibited a small E gradient along single FAs (lower at cell edge) but no S gradient (Figures 6W and 6X). This demonstrates the existence of tension magnitude gradients independent of mechanical switching. Together, these analyses indicate that FP mechanical switching occurs in VinTS and requires vinculin catch-bonding, suggesting that variations in S are a biologically relevant readout.

We lastly sought to determine whether FP mechanical switching in VinTS responds to alterations in mechanical stimuli. Altering ECM stiffness is thought to affect the loading dynamics of mechanical proteins within FAs.[2,4] In molecular clutch models of the FA, substrate stiffness is a major determinant of protein loading rate, with lower loading rates typically occurring on softer substrates.[4] In the context of our model, the degree of FP mechanical switching in MTSs was also predicted to respond to changes in loading rates (Figure S12; Note S1, section V).

Figure 5. Pharmacological disruption of actin reverses FP mechanical switching in ABDTS

(A–D) Representative NIH3T3 cells expressing ABDTL with vehicle control, (E–H) ABDTL treated with latrunculin A (Lat. A), (I–L) ABDTS with vehicle control, or (M–P) ADBTS treated with latrunculin A. Images are acceptor and donor intensities, with cell outline overlaid in red and FRET efficiency and stoichiometry in cell mask. (Q–T) ES-histograms for whole-cell populations of ABDTL with vehicle control (Q, N = 43 cells), ABDTL treated with latrunculin A (R, N = 40 cells), ABDTS with vehicle control (S, N = 39 cells), and ADBTS treated with latrunculin A (T, N = 40 cells) over 3 experimental days, where color bars indicate the cell-averaged fraction of pixels in each bin.

(U) Boxplot of fraction of pixels in each cell in the low E, high S bin ($E < 0.15, S > 0.60$) for the indicated conditions. Differences between groups were detected using the Steel-Dwass test. Levels not connected by the same letter are significantly different at $p < 0.05$. p values are given in Note S3.

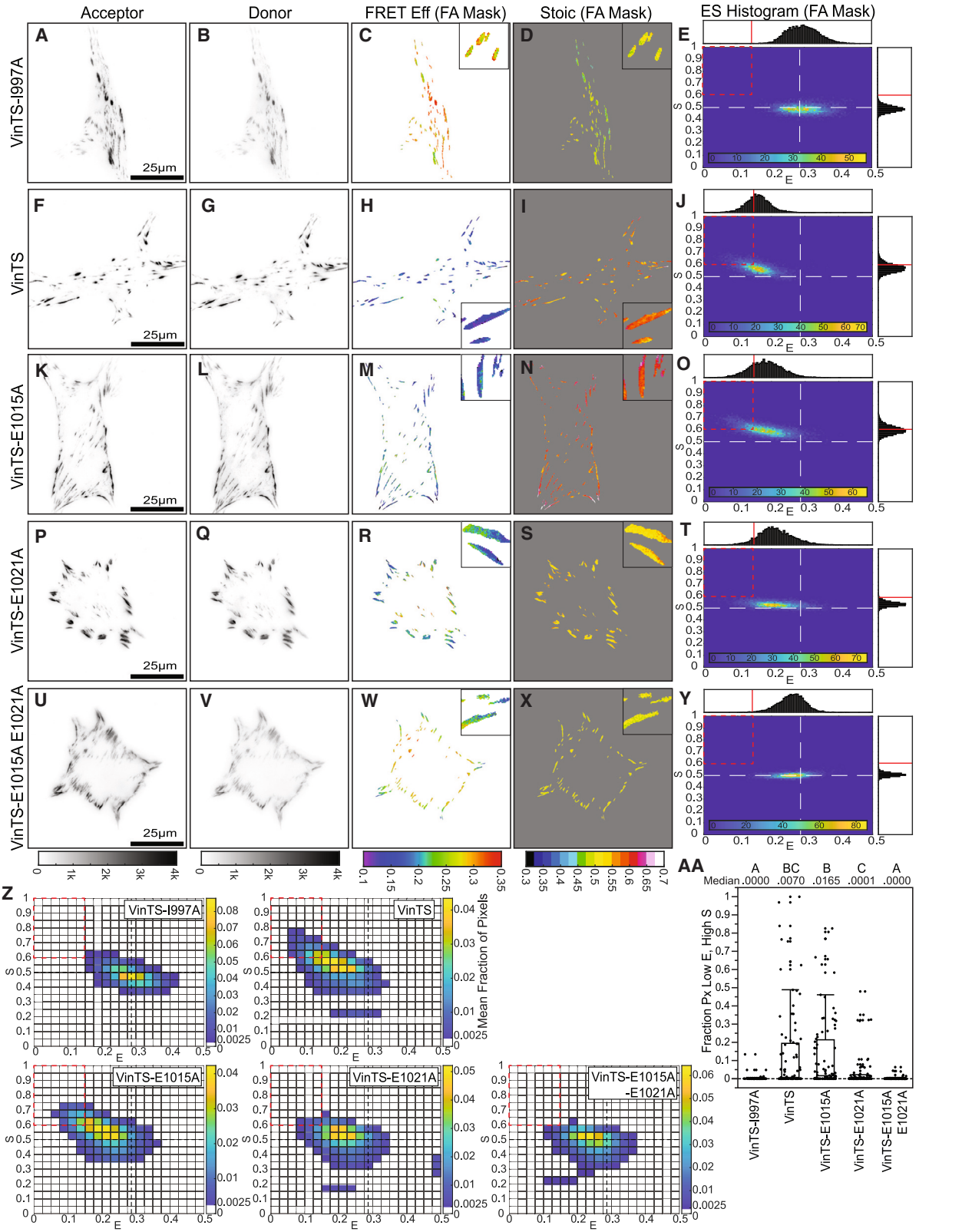

(legend on next page)

Therefore, we experimentally tested the hypothesis that changing the stiffness of the substrate that cells were plated on would alter FP mechanical switching in vinculin. To do so, we seeded vinculin$^{-/-}$ MEFs stably expressing VinTS or VinTS-E1015A-E1021A on fibronectin (FN)-coated polyacrylamide (PA) gels (Figure 7). Previous work indicated that the E of VinTS did not change on 10 kPa gels compared to glass, but did not assess S[16]. Therefore, we chose a softer gel (of approximately 3.5 kPa stiffness; Figure S22) and directly assessed E and S. In VinTS-expressing cells plated on PA gels, we observed changes in the ES-histogram shape consistent with a loss of FP mechanical switching (Figures 7A–7E and 7K). In contrast, the ES-histogram shapes for VinTS-E1015A-E1021A expressing cells on PA gels and glass were similar and consistent with little to no FP mechanical switching (Figures 7F–7J and 7L). Furthermore, we found no statistical difference in the fraction of pixels in the low E, high S bin between the two constructs in cells plated on 3.5-kPa PA gels (Figure 7M), suggesting that the soft substrate eliminated acceptor mechanical switching in vinculin.

Taken together, these results demonstrate that FP mechanical switching occurs in an MTS within a naturally occurring mechanical linker protein, vinculin, and is sensitive to key cell-intrinsic (force-activated bond dynamics) and cell-extrinsic (substrate stiffness) factors underlying mechanosensitive processes at FAs.

DISCUSSION

Uncovering the molecular mechanisms of mechanosensitive signaling requires characterizing multiple steps: mechanotransmission, mechanosensing, mechanotransduction, and mechanoresponse.[3] A current challenge is understanding the spatiotemporal regulation of these steps. Progress has been limited by the lack of tools to probe the various steps inside cells, especially mechanosensing (force-induced changes in protein structure and function). Motivated by *in vitro* experiments demonstrating that FPs undergo reversible, force-induced changes in their structure/function in response to mechanical loading,[17] we hypothesized that FP mechanical switching within an FRET-based MTS for a protein of interest could be used to indirectly probe if, when, and where mechanically similar domains within the protein of interest could mediate mechanosensing. We also reasoned that the continued use and design of MTSs to measure mechanotransmission requires an understanding of FP mechanical switching. Therefore, we use computational modeling to develop a formalism to detect FP mechanical switching in FRET-based biosensors *in cellulo* by three-channel imaging of sensitized emission. Guided by this formalism, we demonstrate that FP mechanical switching occurs *in cellulo* in both a synthetic actin cross-linking protein and the mechanical linker protein vinculin. *In cellulo* mechanical switching is reversible and sensitive to manipulations of cell-generated forces, force-sensitive bond dynamics of the biosensor, and external mechanical stiffness. Together, this work describes an experimental paradigm for detecting the effect of mechanical loads on FPs in cells.

These findings demonstrate that genetically encoded FRET-based MTSs can operate in two modes. The first is measuring mechanotransmission (i.e., the original design intention of MTSs), which requires the absence of FP mechanical switching. In the mechanotransmission mode, quantitative measurements of molecular tension magnitude using the FRET efficiency-force relationship $E_0 = f(F)$ for calibrated MTSs[10,15] are possible because $E_{app} = E_0$ in the absence of FP mechanical switching. In the presence of FP mechanical switching, the calibration becomes inaccurate ($E_{app} \neq E_0$), and alterations in E_{app} due to load magnitude or load duration cannot be decoupled.

To use an MTS in mechanotransmission mode, the framework developed here should be used to ensure the absence of FP mechanical switching in the MTS. Specifically, it should be shown using the ES-histogram that the MTS maintains $S_{app} \sim 0.5$ across the full range of E_{app} values. The absence of FP mechanical switching ensures the accuracy of quantitative measurements of load magnitude using the FRET efficiency-force calibration. However, we note that in the presence of most deviations in S_{app}, a reduction in E_{app} is still indicative of loading, meaning relative comparisons between loaded and unloaded states are still possible, even though the effects of load magnitude and load duration cannot be separated. Additionally, the existing guidelines for force-insensitive FRET-based biosensors established by Coullomb et al. (i.e., the unloaded control should have S_{app} of approximately 0.5 and E_{app} of approximately the unloaded E_0 value for the tension sensor module) should also be applied to the unloaded control to rule out factors not related to FP mechanical switching.[29]

Additionally, we posited that in the presence of substantial FP mechanical switching, MTSs can also operate in a mechanosensing mode. In this mode, the MTS provides a readout of force-induced changes in FP function in response to the load magnitude and load dynamics across the protein of interest. Conceptually, this resembles the force-induced conformational changes of mechanosensing domains that are thought to mediate mechanosensing.[5–8,45] We note that, like some mechanosensing domains, FP mechanical switching depends on both

Figure 6. FP mechanical switching in VinTS is sensitive to manipulation of the vinculin-actin catch bond

(A–Y) Representative vinculin$^{-/-}$ MEFs expressing VinTS-I997A (A–E), VinTS (F–J), VinTS-E1015A (K–O), VinTS- E1021A (P–T), or VinTS-E1015A-E1021A (U–Y) on FN-coated glass, showing images of acceptor intensity, donor intensity, FRET efficiency in the FA mask, stoichiometry in the FA mask, and an ES-histogram of FA-masked pixels for the cell. For single-cell ES-histograms in (E), (J), (O), (T), and (Y), the color bars indicate pixel counts.

(Z) ES-histograms for whole-cell populations (N = 59/89/92/88/101 cells over 2/4/3/3/3 experimental days for VinTS-I997A/VinTS/VinTS-E1015A/VinTS-E1021A/VinTS-E1015A-E1021A), where color bars indicate the cell-averaged fraction of FA-masked pixels in each bin.

(AA) Boxplot of fraction of pixels in each cell in the low E, high S bin ($E < 0.15, S > 0.60$) for each construct. Differences between groups were detected using the Steel-Dwass test. Levels not connected by the same letter are significantly different at $p < 0.05$. p values are given in Note S3.

The data are a new analysis of the 3-channel FRET images from an experiment in a previous publication.[39]

See also Figures S19–S21.

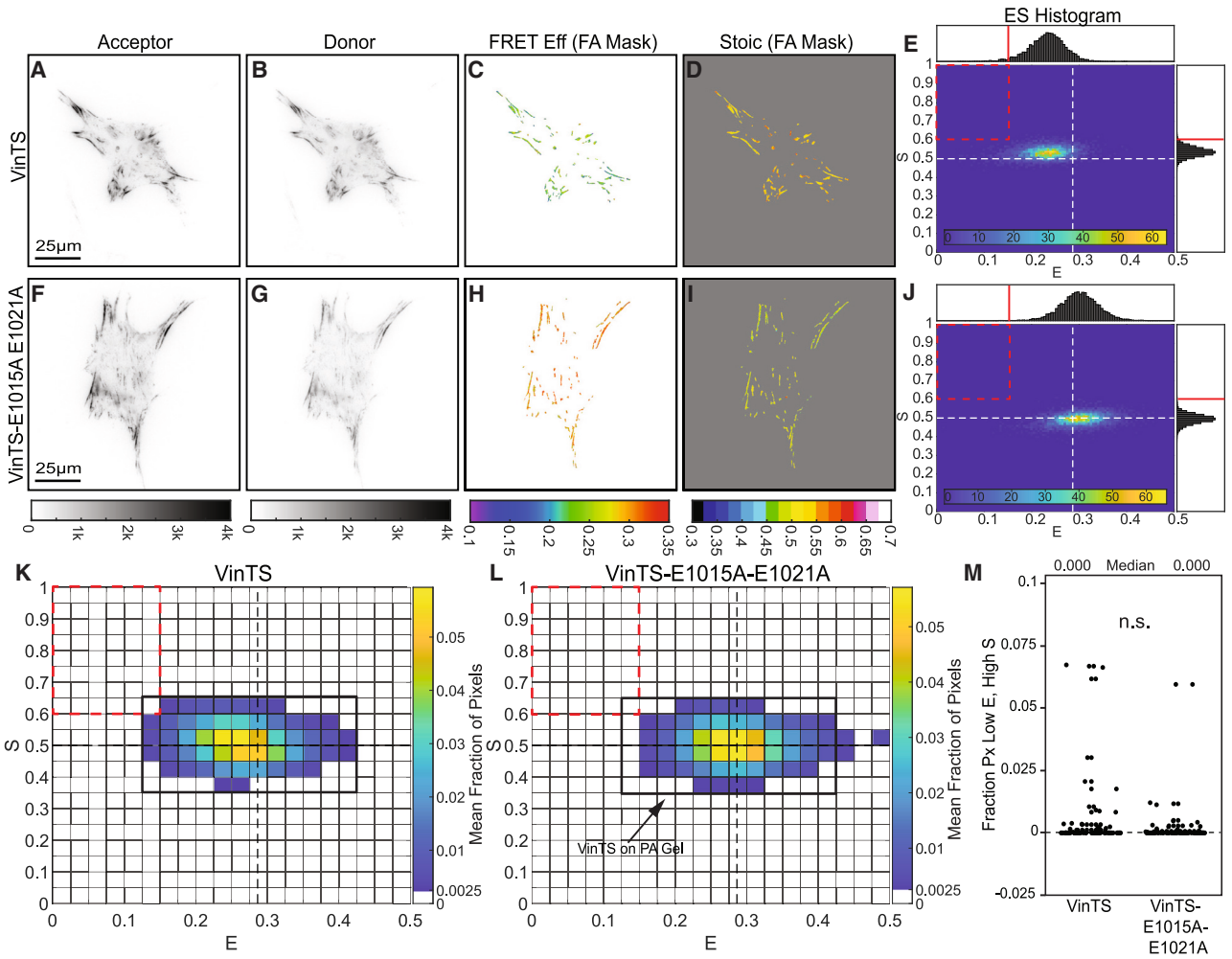

Figure 7. Acceptor mechanical switching in VinTS is eliminated on soft substrates

(A–J) Representative vinculin$^{-/-}$ MEFs expressing VinTS (A–E) or VinTS-E1015A-E1021A (F–J) on FN-coated PA gels, showing images of acceptor intensity, donor intensity, FRET efficiency in the FA mask, stoichiometry in the FA mask, and an ES-histogram of FA-masked pixels for the cell. For single-cell ES-histograms in (E) and (J), the color bars indicate pixel counts.

(K and L) ES-histograms for whole-cell populations of vinculin$^{-/-}$ MEFs expressing VinTS or VinTS-E1015A-E1021A on PA gels (N = 87/92 cells over 3 experimental days for VinTS/VinTS-E1015A-E1021A), where color bars indicate the cell-averaged fraction of FA-masked pixels in each bin. The black outline for VinTS from (K) is overlaid on the histogram for VinTS-E1015A-E1021A in (L) as a guide for the eye.

(M) Boxplot of fraction of FA-masked pixels in each cell in the low E, high S bin ($E < 0.15, S > 0.60$). The difference between the groups was detected using the Wilcoxon rank-sum test; n.s., not significant. p values are given in Note S3.

See also Figure S22.

the load magnitude and load dynamics (e.g., load duration or rate), which is evidenced by the kinetics of GFP mechanical switching from *in vitro* experiments.[17] Thus, FP mechanical switching is not another means to measure load magnitude. Instead, it is an approach to assess whether certain force-induced conformation changes are occurring in a specific load-bearing protein and biological context. Compared to other imaging-based techniques for mechanosensing,[11–13] which rely on labeling unfolded protein domains with secondary binding probes, our approach based on FP mechanical switching has the advantage of being independent of secondary probe binding. Additionally, our approach is suited for measurements of mechanosensing in live cells. The main disadvantage is that the readout is of an FP in the line of loading within the protein of interest and not of endogenous domains. Thus, our approach is an indirect measurement of the capability of the protein of interest to support mechanosensing. To be biologically relevant, the FP undergoing mechanical switching and the mechanosensing domain of interest must have similar mechanical properties. The relevance of mVenus mechanical switching to the force-induced conformational changes of mechanosensitive protein domains characterized previously at the single molecule level is currently unclear. Therefore, we consider this first demonstration of the mechanosensing mode to be analogous to the first examples of uncalibrated MTSs used in mechanotransmission mode,[46] in that these measurements were indicative of loading but the

magnitudes were not known. We do note that, excitingly, mechanical switching of mVenus in VinTS responded to a variety of biologically interesting manipulations, such as manipulation of catch-bonding and the stiffness of the substrate. Determining the relationships between FP mechanical switching and force-sensitive conformational changes in endogenous mechanosensitive domains will be a key topic for the future.

A broad consequence of this work is that the identity of FPs (and thus mechanical properties), as well as their placement (with respect to the line of loading), are critical design elements of any probe or biosensor for a load-bearing protein. Even when different FPs or placements are tolerated biologically, altering either aspect could have unintended consequences on the performance of the sensor or probe when it is placed under mechanical load. Therefore, unless the lack of mechanical switching has been demonstrated in both systems, results from MTSs for the same protein but with different FPs may not be directly comparable even when using FRET efficiency measurements. This is one potential explanation for discrepancies in sets of vinculin[38,47] or E-cadherin[48,49] tension measurements, each based on MTSs with two different FP pairs. Additionally, the consequences of FP identity and placement apply to other probes and sensors that put FPs in the line of mechanical loading but were not explicitly designed to be force sensitive. One example is synthetic cross-linkers harboring a single FP between binding domains, such as the membrane-actin cortex linkers that have been previously used to image membrane proximal actin or manipulate membrane-cortex adhesion.[50,51] Another example is conformation sensors that were designed for reporting the relief of head-tail inhibition (also commonly referred to as autoinhibition), which is often found in load-bearing proteins.[52] This includes the vinculin conformation sensor (VinCS), in which one FP is inserted in the line of force between the head and tail and the other is outside the line of force at the C terminus. For instance, multiple versions of VinCS exist that use different FP FRET pairs and change if the donor or acceptor FP is placed in the loaded versus unloaded positions in the sensor,[30,53,54] suggesting that each version could be affected by FP mechanical switching differently.

An important future direction suggested by this work is the screening and engineering of FPs with different mechanical switching properties. Here, we found that mVenus mechanical switching was dominant over mTFP1, indicating that FPs can have different mechanical switching sensitivities *in cellulo*. To our knowledge, GFP is the only FP to have its *in vitro* mechanical switching properties characterized.[17] However, our experimental data, combined with modeling of a wide set of FP mechanical switching parameters (Figures S1 and S5; Note S1, section VII), suggest that mVenus undergoes mechanical switching *in cellulo* at lower load magnitudes and/or durations than would be expected for GFP *in vitro*. This suggests differences in the mechanical switching properties of GFP versus mVenus and/or differences in mechanical switching for single FPs *in vitro* versus FPs inside sensors *in cellulo*. For MTSs in mechanotransmission mode and other probes and sensors with FPs in the line of loading, proper sensor function requires the use of mechanically stable FPs. It was previously shown *in vitro* that YPet and mCherry can be subjected to considerable load magnitudes and durations (e.g., 24 pN for >5 min) without unfolding.[55] This suggests that these FPs could be well suited for sensors requiring mechanically stable FPs, like MTSs in mechanotransmission mode. However, we suggest that their mechanical switching properties be verified *in cellulo* when used in biosensors. However, the development of future MTSs in mechanosensing mode will require finding FPs with desired mechanical switching properties to enable sensors that function as indirect detectors of mechanosensing in response to a plethora of dynamic loading conditions and for pairing with specific endogenous mechanosensitive domains.

This work describes a framework for assessing FP mechanical stability and provides a means of probing force-sensitive protein function *in cellulo*. First, it provides quality control that will immediately improve the development and application of genetically encoded FRET-based MTSs designed to quantitatively measure the first step in mechanosensitive signaling, mechanotransmission. Second, it provides an approach leveraging FP mechanical switching inside MTSs to indirectly probe another key step in mechanosensitive signaling, mechanosensing. Together, these and existing tools form an overlapping continuum for probing the multi-step molecular mechanisms of mechanosensitive signaling.

Limitations of the study

When applying our framework and experimental methodology for detecting FP mechanical switching *in cellulo*, the following limitations of the study should be considered.

First, in our mathematical model, we made assumptions about the effect of FP mechanical switching on the photophysical properties of FPs to determine the signal contribution for each sensor state in three-channel FRET measurements. To our knowledge, forced-induced changes in the excitation or emission wavelengths of FPs have not been described. Therefore, we assumed that donor FPs that have undergone mechanical switching cannot be excited by any excitation light in the optical system, and that acceptor FPs that have undergone mechanical switching cannot be excited by any excitation light in the optical system and also cannot accept energy from donor FPs. If this assumption is not met, then a substantially more complex formalism is needed. Other, less critical assumptions associated with the mathematical model are detailed in Note S1, section VI.

Second, we focused on sensitized emissions for the FRET imaging modality because both the acceptor and donor are readily observable, its ease of use and low-cost, standard calibration methodologies to measure FRET efficiency, and, most important, existing frameworks for analyzing FP stoichiometry.[27–29] The framework we developed is not immediately adaptable to other FRET modalities, such as *fluorescence* lifetime *imaging* and spectral imaging-based FRET, which are also used to image MTSs.[55,56] However, we suggest that sensitized emission FRET can be used for the quality control of existing and future MTSs designed for mechanotransmission mode before using them in other imaging modalities.

Third, we applied our framework to TSMod,[30] which contains a calibrated unstructured tension sensing element. The framework here can be applied immediately to TSMod in other endogenous and synthetic proteins. By modifying the eff-force relationship,

the framework can be readily applied to other calibrated tension sensing elements whose eff-force relationships are loading rate independent and have no hysteresis, such as unstructured repeats of GGSGGS[10] and domains with rapid unfolding transition like HP35 and HP35st.[15] In contrast, the framework is not readily modifiable for structured tension sensing elements exhibiting loading rate dependence or hysteresis.

Lastly, FP mechanical switching is not a direct readout for force-induced changes of mechanosensitive domains within the protein of interest. A greater understanding of the mechanical behavior of FPs will be needed to use FP mechanical switching as a proxy/indirect readout for specific mechanosensitive domains.

STAR★METHODS

Detailed methods are provided in the online version of this paper and include the following:

- KEY RESOURCES TABLE
- RESOURCE AVAILABILITY
  - Lead contact
  - Materials availability
  - Data and code availability
- EXPERIMENTAL MODEL AND STUDY PARTICIPANT DETAILS
  - Cell culture and expression of DNA constructs
- METHOD DETAILS
  - Generation of DNA constructs
  - Cell seeding
  - Analysis of previous VinTS datasets
  - Fixation & phalloidin labeling of actin
  - Pharmacological Inhibitors
  - Imaging of FRET-based sensors and Immunofluorescence
  - Preparation of methacrylated coverslips and hydrophobic glass substrate
  - Preparation, imaging, and mechanical testing of PA gels
  - Mathematical models of FP mechanical switching in MTS
  - Steered molecular dynamics simulations of FPs
- QUANTIFICATION AND STATISTICAL ANALYSIS
  - Calculation of FRET efficiency and stoichiometry from sensitized emission
  - Computation of cell and FA morphology metrics
  - Statistical analysis

SUPPLEMENTAL INFORMATION

Supplemental information can be found online at https://doi.org/10.1016/j.crmeth.2024.100815.

ACKNOWLEDGMENTS

We thank Dr. Stefano Di Talia and Dr. Victoria Deneke (Duke University) for their assistance with molecular cloning to generate ABDTS and ABDTL constructs. We also acknowledge support from the Duke Compute Cluster. Images of molecular dynamics simulations in this work were made with VMD and NAMD software support. VMD and NAMD were developed with NIH support by the Theoretical and Computational Biophysics group at the Beckman Institute, University of Illinois at Urbana-Champaign. This research was supported by the NIH (1R01GM121739 to B.D.H. and 5T32GM008555-26 to K.L.C.), the National Science Foundation (2310593 to B.D.H., GRFP DGE 2139754 to T.C.S., and GRFP DGE 2139754 to J.N.M.), and the National Cancer Institute K00 Fellowship (K00CA245789 to A.T.B.).

AUTHOR CONTRIBUTIONS

B.D.H. and J.L.W. conceived the project. K.L.C. and J.N.M. conducted the experiments. T.C.S., T.R.H., K.L.C., J.N.M., and B.A.J. performed the data analyses. T.C.S. designed and analyzed the mathematical models. A.T.B. performed and analyzed the SMD simulations. T.C.S., T.R.H., A.T.B., and B.D.H. wrote the paper. T.C.S., A.T.B., B.A.J., and B.D.H. edited the paper.

DECLARATION OF INTERESTS

The authors declare no competing interests.

Received: January 11, 2024
Revised: May 3, 2024
Accepted: June 17, 2024
Published: July 9, 2024

REFERENCES

1. Wolfenson, H., Yang, B., and Sheetz, M.P. (2019). Steps in Mechanotransduction Pathways that Control Cell Morphology. Annu. Rev. Physiol. *81*, 585–605. https://doi.org/10.1146/annurev-physiol-021317-121245.
2. Hoffman, B.D., Grashoff, C., and Schwartz, M.A. (2011). Dynamic molecular processes mediate cellular mechanotransduction. Nature *475*, 316–323. https://doi.org/10.1038/nature10316.
3. Hoffman, B.D., and Yap, A.S. (2015). Towards a Dynamic Understanding of Cadherin-Based Mechanobiology. Trends Cell Biol. *25*, 803–814. https://doi.org/10.1016/j.tcb.2015.09.008.
4. Elosegui-Artola, A., Trepat, X., and Roca-Cusachs, P. (2018). Control of Mechanotransduction by Molecular Clutch Dynamics. Trends Cell Biol. *28*, 356–367. https://doi.org/10.1016/j.tcb.2018.01.008.
5. Sharma, S., Subramani, S., and Popa, I. (2021). Does protein unfolding play a functional role in vivo? FEBS J. *288*, 1742–1758. https://doi.org/10.1111/febs.15508.
6. del Rio, A., Perez-Jimenez, R., Liu, R., Roca-Cusachs, P., Fernandez, J.M., and Sheetz, M.P. (2009). Stretching single talin rod molecules activates vinculin binding. Science *323*, 638–641. https://doi.org/10.1126/science.1162912.
7. Yao, M., Qiu, W., Liu, R., Efremov, A.K., Cong, P., Seddiki, R., Payre, M., Lim, C.T., Ladoux, B., Mège, R.M., and Yan, J. (2014). Force-dependent conformational switch of alpha-catenin controls vinculin binding. Nat. Commun. *5*, 4525. https://doi.org/10.1038/ncomms5525.
8. Alegre-Cebollada, J. (2021). Protein nanomechanics in biological context. Biophys. Rev. *13*, 435–454. https://doi.org/10.1007/s12551-021-00822-9.
9. LaCroix, A.S., Rothenberg, K.E., and Hoffman, B.D. (2015). Molecular-Scale Tools for Studying Mechanotransduction. Annu. Rev. Biomed. Eng. *17*, 287–316. https://doi.org/10.1146/annurev-bioeng-071114-040531.
10. Ham, T.R., Collins, K.L., and Hoffman, B.D. (2019). Molecular Tension Sensors: Moving Beyond Force. Curr. Opin. Biomed. Eng. *12*, 83–94. https://doi.org/10.1016/j.cobme.2019.10.003.
11. Sawada, Y., Tamada, M., Dubin-Thaler, B.J., Cherniavskaya, O., Sakai, R., Tanaka, S., and Sheetz, M.P. (2006). Force sensing by mechanical extension of the Src family kinase substrate p130Cas. Cell *127*, 1015–1026. https://doi.org/10.1016/j.cell.2006.09.044.
12. Yonemura, S., Wada, Y., Watanabe, T., Nagafuchi, A., and Shibata, M. (2010). alpha-Catenin as a tension transducer that induces adherens junction development. Nat. Cell Biol. *12*, 533–542. https://doi.org/10.1038/ncb2055.
13. Zhong, B.L., Vachharajani, V.T., and Dunn, A.R. (2022). Facile detection of mechanical forces across proteins in cells with STReTCh. Cell Rep. Methods *2*, 100278. https://doi.org/10.1016/j.crmeth.2022.100278.
14. Tao, A., LaCroix, A.S., Shoyer, T.C., Venkatraman, V., Xu, K.L., Feiger, B., and Hoffman, B.D. (2023). Identifying constitutive and context-specific

molecular-tension-sensitive protein recruitment within focal adhesions. Dev. Cell *58*, 522–534.e7. https://doi.org/10.1016/j.devcel.2023.02.015.

15. Fischer, L.S., Rangarajan, S., Sadhanasatish, T., and Grashoff, C. (2021). Molecular Force Measurement with Tension Sensors. Annu. Rev. Biophys. *50*, 595–616. https://doi.org/10.1146/annurev-biophys-101920-064756.
16. LaCroix, A.S., Lynch, A.D., Berginski, M.E., and Hoffman, B.D. (2018). Tunable molecular tension sensors reveal extension-based control of vinculin loading. Elife *7*, e33927. https://doi.org/10.7554/eLife.33927.
17. Ganim, Z., and Rief, M. (2017). Mechanically switching single-molecule fluorescence of GFP by unfolding and refolding. Proc. Natl. Acad. Sci. USA *114*, 11052–11056. https://doi.org/10.1073/pnas.1704937114.
18. Saeger, J., Hytönen, V.P., Klotzsch, E., and Vogel, V. (2012). GFP's mechanical intermediate states. PLoS One *7*, e46962. https://doi.org/10.1371/journal.pone.0046962.
19. Dudko, O.K., Hummer, G., and Szabo, A. (2006). Intrinsic rates and activation free energies from single-molecule pulling experiments. Phys. Rev. Lett. *96*, 108101. https://doi.org/10.1103/PhysRevLett.96.108101.
20. Evans, E. (2001). Probing the relation between force–lifetime–and chemistry in single molecular bonds. Annu. Rev. Biophys. Biomol. Struct. *30*, 105–128. https://doi.org/10.1146/annurev.biophys.30.1.105.
21. Wang, Y., Yan, J., and Goult, B.T. (2019). Force-Dependent Binding Constants. Biochemistry *58*, 4696–4709. https://doi.org/10.1021/acs.biochem.9b00453.
22. Dietz, H., and Rief, M. (2004). Exploring the energy landscape of GFP by single-molecule mechanical experiments. Proc. Natl. Acad. Sci. USA *101*, 16192–16197. https://doi.org/10.1073/pnas.0404549101.
23. Perez-Jimenez, R., Garcia-Manyes, S., Ainavarapu, S.R.K., and Fernandez, J.M. (2006). Mechanical unfolding pathways of the enhanced yellow fluorescent protein revealed by single molecule force spectroscopy. J. Biol. Chem. *281*, 40010–40014. https://doi.org/10.1074/jbc.M609890200.
24. Snapp, E.L. (2009). Fluorescent proteins: a cell biologist's user guide. Trends Cell Biol. *19*, 649–655. https://doi.org/10.1016/j.tcb.2009.08.002.
25. Roca-Cusachs, P., Iskratsch, T., and Sheetz, M.P. (2012). Finding the weakest link: exploring integrin-mediated mechanical molecular pathways. J. Cell Sci. *125*, 3025–3038. https://doi.org/10.1242/jcs.095794.
26. Algar, W.R., Hildebrandt, N., Vogel, S.S., and Medintz, I.L. (2019). FRET as a biomolecular research tool - understanding its potential while avoiding pitfalls. Nat. Methods *16*, 815–829. https://doi.org/10.1038/s41592-019-0530-8.
27. Chen, H., Puhl, H.L., Koushik, S.V., Vogel, S.S., and Ikeda, S.R. (2006). Measurement of FRET efficiency and ratio of donor to acceptor concentration in living cells. Biophys. J. *91*, L39–L41. https://doi.org/10.1529/biophysj.106.088773.
28. Gates, E.M., LaCroix, A.S., Rothenberg, K.E., and Hoffman, B.D. (2019). Improving Quality, Reproducibility, and Usability of FRET-Based Tension Sensors. Cytometry A. *95*, 201–213. https://doi.org/10.1002/cyto.a.23688.
29. Coullomb, A., Bidan, C.M., Qian, C., Wehnekamp, F., Oddou, C., Albigès-Rizo, C., Lamb, D.C., and Dupont, A. (2020). QuanTI-FRET: a framework for quantitative FRET measurements in living cells. Sci. Rep. *10*, 6504. https://doi.org/10.1038/s41598-020-62924-w.
30. Grashoff, C., Hoffman, B.D., Brenner, M.D., Zhou, R., Parsons, M., Yang, M.T., McLean, M.A., Sligar, S.G., Chen, C.S., Ha, T., and Schwartz, M.A. (2010). Measuring mechanical tension across vinculin reveals regulation of focal adhesion dynamics. Nature *466*, 263–266. https://doi.org/10.1038/nature09198.
31. Johnson, H.W., and Schell, M.J. (2009). Neuronal IP3 3-kinase is an F-actin-bundling protein: role in dendritic targeting and regulation of spine morphology. Mol. Biol. Cell *20*, 5166–5180. https://doi.org/10.1091/mbc.e09-01-0083.
32. Belin, B.J., Goins, L.M., and Mullins, R.D. (2014). Comparative analysis of tools for live cell imaging of actin network architecture. BioArchitecture *4*, 189–202. https://doi.org/10.1080/19490992.2014.1047714.
33. Spracklen, A.J., Fagan, T.N., Lovander, K.E., and Tootle, T.L. (2014). The pros and cons of common actin labeling tools for visualizing actin dynamics during Drosophila oogenesis. Dev. Biol. *393*, 209–226. https://doi.org/10.1016/j.ydbio.2014.06.022.
34. LaCroix, A.S., Rothenberg, K.E., Berginski, M.E., Urs, A.N., and Hoffman, B.D. (2015). Construction, imaging, and analysis of FRET-based tension sensors in living cells. Methods Cell Biol. *125*, 161–186. https://doi.org/10.1016/bs.mcb.2014.10.033.
35. Aratyn-Schaus, Y., Oakes, P.W., and Gardel, M.L. (2011). Dynamic and structural signatures of lamellar actomyosin force generation. Mol. Biol. Cell *22*, 1330–1339. https://doi.org/10.1091/mbc.E10-11-0891.
36. Murrell, M., Oakes, P.W., Lenz, M., and Gardel, M.L. (2015). Forcing cells into shape: the mechanics of actomyosin contractility. Nat. Rev. Mol. Cell Biol. *16*, 486–498. https://doi.org/10.1038/nrm4012.
37. Bays, J.L., and DeMali, K.A. (2017). Vinculin in cell-cell and cell-matrix adhesions. Cell. Mol. Life Sci. *74*, 2999–3009. https://doi.org/10.1007/s00018-017-2511-3.
38. Rothenberg, K.E., Scott, D.W., Christoforou, N., and Hoffman, B.D. (2018). Vinculin Force-Sensitive Dynamics at Focal Adhesions Enable Effective Directed Cell Migration. Biophys. J. *114*, 1680–1694. https://doi.org/10.1016/j.bpj.2018.02.019.
39. Chirasani, V.R., Khan, M.A.I., Malavade, J.N., Dokholyan, N.V., Hoffman, B.D., and Campbell, S.L. (2023). Molecular basis and cellular functions of vinculin-actin directional catch bonding. Nat. Commun. *14*, 8300. https://doi.org/10.1038/s41467-023-43779-x.
40. Shoyer, T.C., Gates, E.M., Cabe, J.I., Urs, A.N., Conway, D.E., and Hoffman, B.D. (2023). Coupling during collective cell migration is controlled by a vinculin mechanochemical switch. Proc. Natl. Acad. Sci. USA *120*, e2316456120. https://doi.org/10.1073/pnas.2316456120.
41. Thompson, P.M., Tolbert, C.E., Shen, K., Kota, P., Palmer, S.M., Plevock, K.M., Orlova, A., Galkin, V.E., Burridge, K., Egelman, E.H., et al. (2014). Identification of an actin binding surface on vinculin that mediates mechanical cell and focal adhesion properties. Structure *22*, 697–706. https://doi.org/10.1016/j.str.2014.03.002.
42. Auernheimer, V., and Goldmann, W.H. (2014). Serine phosphorylation on position 1033 of vinculin impacts cellular mechanics. Biochem. Biophys. Res. Commun. *450*, 1095–1098. https://doi.org/10.1016/j.bbrc.2014.06.122.
43. Auernheimer, V., Lautscham, L.A., Leidenberger, M., Friedrich, O., Kappes, B., Fabry, B., and Goldmann, W.H. (2015). Vinculin phosphorylation at residues Y100 and Y1065 is required for cellular force transmission. J. Cell Sci. *128*, 3435–3443. https://doi.org/10.1242/jcs.172031.
44. Huang, D.L., Bax, N.A., Buckley, C.D., Weis, W.I., and Dunn, A.R. (2017). Vinculin forms a directionally asymmetric catch bond with F-actin. Science *357*, 703–706. https://doi.org/10.1126/science.aan2556.
45. Yao, M., Goult, B.T., Chen, H., Cong, P., Sheetz, M.P., and Yan, J. (2014). Mechanical activation of vinculin binding to talin locks talin in an unfolded conformation. Sci. Rep. *4*, 4610. https://doi.org/10.1038/srep04610.
46. Meng, F., Suchyna, T.M., and Sachs, F. (2008). A fluorescence energy transfer-based mechanical stress sensor for specific proteins in situ. FEBS J. *275*, 3072–3087. https://doi.org/10.1111/j.1742-4658.2008.06461.x.
47. Kanoldt, V., Kluger, C., Barz, C., Schweizer, A.L., Ramanujam, D., Windgasse, L., Engelhardt, S., Chrostek-Grashoff, A., and Grashoff, C. (2020). Metavinculin modulates force transduction in cell adhesion sites. Nat. Commun. *11*, 6403. https://doi.org/10.1038/s41467-020-20125-z.
48. Cai, D., Chen, S.C., Prasad, M., He, L., Wang, X., Choesmel-Cadamuro, V., Sawyer, J.K., Danuser, G., and Montell, D.J. (2014). Mechanical feedback through E-cadherin promotes direction sensing during collective cell migration. Cell *157*, 1146–1159. https://doi.org/10.1016/j.cell.2014.03.045.
49. Eder, D., Basler, K., and Aegerter, C.M. (2017). Challenging FRET-based E-Cadherin force measurements in Drosophila. Sci. Rep. *7*, 13692. https://doi.org/10.1038/s41598-017-14136-y.

50. Bisaria, A., Hayer, A., Garbett, D., Cohen, D., and Meyer, T. (2020). Membrane-proximal F-actin restricts local membrane protrusions and directs cell migration. Science *368*, 1205–1210. https://doi.org/10.1126/science.aay7794.

51. Bergert, M., Lembo, S., Sharma, S., Russo, L., Milovanović, D., Gretarsson, K.H., Börmel, M., Neveu, P.A., Hackett, J.A., Petsalaki, E., and Diz-Muñoz, A. (2021). Cell Surface Mechanics Gate Embryonic Stem Cell Differentiation. Cell Stem Cell *28*, 209–216.e4. https://doi.org/10.1016/j.stem.2020.10.017.

52. Khan, R.B., and Goult, B.T. (2019). Adhesions Assemble!-Autoinhibition as a Major Regulatory Mechanism of Integrin-Mediated Adhesion. Front. Mol. Biosci. *6*, 144. https://doi.org/10.3389/fmolb.2019.00144.

53. Chen, H., Cohen, D.M., Choudhury, D.M., Kioka, N., and Craig, S.W. (2005). Spatial distribution and functional significance of activated vinculin in living cells. J. Cell Biol. *169*, 459–470. https://doi.org/10.1083/jcb.200410100.

54. Case, L.B., Baird, M.A., Shtengel, G., Campbell, S.L., Hess, H.F., Davidson, M.W., and Waterman, C.M. (2015). Molecular mechanism of vinculin activation and nanoscale spatial organization in focal adhesions. Nat. Cell Biol. *17*, 880–892. https://doi.org/10.1038/ncb3180.

55. Austen, K., Ringer, P., Mehlich, A., Chrostek-Grashoff, A., Kluger, C., Klingner, C., Sabass, B., Zent, R., Rief, M., and Grashoff, C. (2015). Extracellular rigidity sensing by talin isoform-specific mechanical linkages. Nat. Cell Biol. *17*, 1597–1606. https://doi.org/10.1038/ncb3268.

56. Arsenovic, P.T., Mayer, C.R., and Conway, D.E. (2017). SensorFRET: A Standardless Approach to Measuring Pixel-based Spectral Bleed-through and FRET Efficiency using Spectral Imaging. Sci. Rep. *7*, 15609. https://doi.org/10.1038/s41598-017-15411-8.

57. Mierke, C.T., Kollmannsberger, P., Zitterbart, D.P., Diez, G., Koch, T.M., Marg, S., Ziegler, W.H., Goldmann, W.H., and Fabry, B. (2010). Vinculin facilitates cell invasion into three-dimensional collagen matrices. J. Biol. Chem. *285*, 13121–13130. https://doi.org/10.1074/jbc.M109.087171.

58. Rothenberg, K.E., Neibart, S.S., LaCroix, A.S., and Hoffman, B.D. (2015). Controlling Cell Geometry Affects the Spatial Distribution of Load Across Vinculin. Cell. Mol. Bioeng. *8*, 364–382. https://doi.org/10.1007/s12195-015-0404-9.

59. Lee, S., Stanton, A.E., Tong, X., and Yang, F. (2019). Hydrogels with enhanced protein conjugation efficiency reveal stiffness-induced YAP localization in stem cells depends on biochemical cues. Biomaterials *202*, 26–34. https://doi.org/10.1016/j.biomaterials.2019.02.021.

STAR★METHODS

KEY RESOURCES TABLE

REAGENT or RESOURCE	SOURCE	IDENTIFIER
Bacterial and virus strains		
NEB 5-alpha competent E. coli	New England Biolabs	C2987U
Chemicals, peptides, and recombinant proteins		
Fibronectin	Thermo Fisher	33016015
Phalloidin-AF647	Thermo Fisher	A22287
Latrunculin A	Sigma-Aldrich	L5163
DMEMgfp-2 live cell visualization media	Sapphire North America	MC102
Lipofectamine 2000	Thermo Fisher	11668019
OptiMEM	Thermo Fisher	31985070
EcoRI-HF	New England Biolabs	R3101S
NotI-HF	New England Biolabs	R3189S
BamHI-HF	New England Biolabs	R3136S
T4 DNA Ligase	New England Biolabs	M0202S
Critical commercial assays		
Gibson Assembly Master Mix	New England Biolabs	E2611S
Experimental models: Cell lines		
NIH/3T3 cells	ATCC	Cat# CRL-1658; RRID:CVCL_0594
Vinculin −/− mouse embryonic fibroblasts	Gift from Dr. Ben Fabry and Dr. Wolfgang H. Goldmann, Friedrich-Alexander-Universität Erlangen-Nürnberg; Mierke et al. 2010[57]	N/A
Oligonucleotides		
Primer (forward) used in construction of ABDTS, specifically for the generation of fragment containing F-tractin and Linker 1 by PCR using pEGFP-C1 F-tractin-EGFP: CCACTAGTCCAGTGTGGTGGA TGGCGCGACCACGGGGC	Integrated DNA Technologies	N/A
Primer (reverse) used in construction of ABDTS, specifically for the generation of fragment containing F-tractin and Linker 1 by PCR using pEGFP-C1 F-tractin-EGFP: TGCTCACCATCATGGTGGCGA CCGGTAGCG	Integrated DNA Technologies	N/A
Primer (forward) used in construction of ABDTS, specifically for the generation of the fragment containing TSmod by PCR using pcDNA3.1-TSMod: CGCCACCATGATGGTGAGCAAGGGCGAG	Integrated DNA Technologies	N/A
Primer (reverse) used in construction of ABDTS, specifically for the generation of the fragment containing TSmod by PCR using pcDNA3.1-TSMod: CGCTGCCGCCCTTGTACAGCTCGTCCATGC	Integrated DNA Technologies	N/A
Primer (forward) used in construction of ABDTS, specifically for the generation of the fragment containing Linker 2 and F-tractin by PCR using pEGFP-C1 F-tractin-EGFP: GCTGTACAAGGGCGGCAGCGGCAGCGATCCCCC CGTGGCCACCATGGCGCGACCACGGGGC	Integrated DNA Technologies	N/A
Primer (reverse) used in construction of ABDTS, specifically for the generation of the fragment containing Linker 2 and F-tractin by PCR using pEGFP-C1 F-tractin-EGFP: CGGGCCCTCTAGACTCGAGCTTACCCTGCGGCCGCTGC	Integrated DNA Technologies	N/A

(*Continued on next page*)

Continued

REAGENT or RESOURCE	SOURCE	IDENTIFIER
Recombinant DNA		
pcDNA3.1-VinTS	Grashoff et al. 2010[30]	Addgene 26019
pcDNA3.1-VinTS-I997A	Rothenberg et al. 2018[38]	Addgene 111828
pcDNA3.1-VinTS-E1015A	Chirasani et al. 2024[39]	Addgene 213415
pcDNA3.1-VinTS-E1021A	Chirasani et al. 2024[39]	Addgene 213416
pcDNA3.1-VinTS-E1015A-E1021A	Chirasani et al. 2024[39]	Addgene 213417
pRRL-VinTS	Rothenberg et al. 2018[38]	Addgene 111830
pRRL-VinTS-E1015A-E1021A	Chirasani et al. 2024[39]	Addgene 213411
pcDNA3.1-ABDTS	This paper	Addgene 215368
pcDNA3.1-ABDTL	This paper	Addgene 215371
Software and algorithms		
MATLAB	Mathworks	N/A
MATLAB Code, Image Pre-processing	LaCroix et al. 2018[16]	Zenodo: https://doi.org/10.5281/zenodo.11625595 Also see Gitlab: https://gitlab.oit.duke.edu/HoffmanLab-Public/image-preprocessing
MATLAB Code, Three-Channel FRET Image Analysis	LaCroix et al. 2018[16]	Zenodo: https://doi.org/10.5281/zenodo.11625634 Also see Gitlab: https://gitlab.oit.duke.edu/HoffmanLab-Public/fret-analysis
MATLAB Code, Simulation and Analysis of Mathematical Models of FP Mechanical Switching in MTSs	This paper	Zenodo: Also see Gitlab: https://gitlab.oit.duke.edu/HoffmanLab-Public/fpmechanicalswitchinmts_model
JMP Pro	SAS	N/A

RESOURCE AVAILABILITY

Lead contact

Further information and requests for resources and reagents should be directed to and will be fulfilled by the lead contact, Brenton D. Hoffman (brenton.hoffman@duke.edu).

Materials availability

All plasmids generated in this study will be made publicly available on Addgene.

Data and code availability

- All data reported in this paper will be shared by the lead contact upon request.
- MATLAB codes used to perform image pre-processing (https://gitlab.oit.duke.edu/HoffmanLab-Public/image-preprocessing), perform three channel sensitized emission FRET image analysis (https://gitlab.oit.duke.edu/HoffmanLab-Public/fret-analysis), and analyze and simulate the mathematical models of FP mechanical switching in MTSs (https://gitlab.oit.duke.edu/HoffmanLab-Public/fpmechanicalswitchinmts_model) are publicly available on GitLab. Archival DOIs are listed in the key resources table.
- Any additional information required to reanalyze the data reported in this paper is available from the lead contact upon request.

EXPERIMENTAL MODEL AND STUDY PARTICIPANT DETAILS

Cell culture and expression of DNA constructs

Vinculin −/− MEFs (kindly provided by Dr. Ben Fabry and Dr. Wolfgang H. Goldmann, Friedrich-Alexander-Universität Erlangen-Nürnberg)[57] were maintained at 37°C in a humidified 5% CO_2 atmosphere in Dulbecco's Modified Eagle's Medium (DMEM) high glucose with sodium pyruvate (D6429; Sigma Aldrich, St. Louis, MO) supplemented with 10% FBS (HyClone SH30071.03; Cytivia, Marlborough, MA), 1% v/v non-essential amino acids (11140050; Thermo Fisher Scientific, Waltham, MA), and 1% v/v penicillin-streptomycin solution (15140122; Thermo Fisher). The generation of cell lines stably expressing VinTS and VinTS-E1015A-E1021A via lentiviral transduction were described previously.[38,39,58] NIH3T3cells were obtained from ATCC (CRL-1658) and maintained in

the same conditions, using the same media formulation except for the omission of non-essential amino acids. For transient expression of ABDTS or ABDTL, NIH 3T3s were transfected at 50–75% confluence in 6-well tissue culture plates (25–105; Genesee Scientific, El Cajon, CA) using Lipofectamine 2000 (11668019; Thermo Fisher) and OptiMEM (31985070; Thermo Fisher) following the manufacturer's instructions.

METHOD DETAILS

Generation of DNA constructs

Construction of pcDNA3.1-VinTS, pcDNA3.1-VinTS-I997A, pcDNA3.1-VinTS-E1015A, pcDNA3.1-VinTS-E1021A, pcDNA3.1-VinTS-E1015A-E1021A, pRRL-VinTS, and pRRL-VinTS-E1015A-E1021A have been described previously.[30,38,39] ABDTS is comprised of F-tractin (actin-binding peptide from rat neuronal inositol 1,4,5-triphosphate 3-kinase A), followed by a 9 amino acid linker (GLALPVATM, hereafter called "Linker 1"), the original TSMod, an 11 amino acid linker (GGSGSDPPVAT, hereafter called "Linker 2"), and a second F-tractin. F-tractin and Linker 1 were derived from pEGFP-C1 F-tractin-EGFP (Addgene Plasmid #58473).[32] The original TSMod was derived from pcDNA3.1-TSMod (Addgene Plasmid #26021).[30] Linker 2 (GGSGSDPPVAT) was used previously in another construct containing F-tractin.[33] Gibson Assembly (with Gibson Assembly Master Mix, E2611S; NEB, Ipswich, MA) was used to generate pcDNA3.1-ABDTS from pcDNA3.1 vector digested with EcoRI-HF (Cat #: R3101S; NEB)/NotI-HF (Cat #: R3189S; NEB) and the following three fragments containing complementary regions: (1) F-tractin and Linker 1, (2) TSMod, and (3) Linker 2 and F-tractin. The fragment containing F-tractin and Linker 1 was generated by Polymerase Chain Reaction (PCR) using pEGFP-C1 F-tractin-EGFP and the oligonucleotide primer sequences (5′ to 3′) CCACTAGTCCAGTGTGGTGGATGGCGCGA CCACGGGGC (forward) and TGCTCACCATCATGGTGGCGACCGGTAGCG (reverse). The fragment containing TSmod was generated by PCR using pcDNA3.1-TSMod and the oligonucleotide primer sequences (5′ to 3′) CGCCACCATGATGGTGAGCAAGG GCGAG (forward) and CGCTGCCGCCCTTGTACAGCTCGTCCATGC (reverse). The fragment containing Linker 2 and F-tractin was generated by PCR using pEGFP-C1 F-tractin-EGFP and the oligonucleotide primer sequences (5′ to 3′) GCTGTACAAGG GCGGCAGCGGCAGCGATCCCCCCGTGGCCACCATGGCGCGACCACGGGGC (forward) and CGGGCCCTCTAGACTCGAGCTTA CCCTGCGGCCGCTGC (reverse). ABDTL is comprised of F-tractin, Linker 1, and the original TSMod, i.e., only the part of ABDTS before Linker 2 and the second F-tractin. pcDNA3.1-ABDTL was generated via PCR from pcDNA3.1-ABDTS and inserted into pcDNA3.1 via BamHI-HF (Cat #: R3136S; NEB)/EcoRI-HF (Cat #: R3101S; NEB) digestion and subsequent ligation (Cat #: M0202S; NEB). All newly generated constructs were verified by DNA sequencing (GENEWIZ from Azenta).

Cell seeding

For imaging, glass bottom dishes with no. 1.5 coverslips (FD35-100; World Precision Instruments, Sarasota, FL) or no. 1.5 glass coverslips mounted in reusable metal dishes (30-1313-03192; Bioptechs, Butler, PA) were incubated with 10 μg/mL fibronectin (33016015; Thermo Fisher) in PBS at room temperature for 1 h and rinsed once with PBS. Approximately 3000 cells/cm^2 were plated on the dishes. Cells were incubated for 4 h to enable sufficient spreading.

Analysis of previous VinTS datasets

Analyses were conducted on previously obtained three-channel FRET images of Vinculin −/− MEFs expressing VinTS or VinTS-I997A on FN-coated glass that were part of the data in the study by Rothenberg et al.,[38] and the three-channel FRET images of Vinculin −/− MEFs expressing VinTS, VinTS-I997A, VinTS-E1015A, VinTS-E1021A, or VinTS-E1015A-E1021A on FN-coated glass that were part of the data in the study by Chirasani, Khan, Malavade et al.[39]

Fixation & phalloidin labeling of actin

For fixation, cells were washed twice with PBS, fixed with 4% v/v EM-grade paraformaldehyde (Cat #: 15700; Electron Microscopy Sciences, Hatfield, PA) in PBS for 10 min and then rinsed with PBS. To label actin, cells were permeabilized with 0.1% Triton X- in PBS for 5 min, blocked with 2% bovine serum albumin (BSA, A7906-100G; Sigma-Aldrich) in PBS for 30 min, treated with Alexa Fluor 647-conjugated phalloidin (A22287; Thermo Fisher) at a 1:100 dilution for 60 min, and then rinsed three times with PBS. Cells were imaged in PBS.

Pharmacological Inhibitors

Cells were seeded on fibronectin-coated glass coverslips as described above. A solution of 1 μM Latrunculin A (L5163; Sigma-Aldrich) were prepared from a 2 mM stock solution in DMSO (D2650; Sigma-Aldrich) by dilution in complete growth medium. Vehicle only controls were conducted with DMSO in complete growth medium. Cells were treated for 15 min at 37°C prior to fixation.

Imaging of FRET-based sensors and Immunofluorescence

An Olympus inverted fluorescent microscope (IX83; Olympus, Tokyo, Japan) was used to image samples as described previously.[38] Images were acquired at 60x magnification (UPlanSApo 60X/NA1.35 Objective, Olympus) and illuminated by a Lambda LS equipped with a 300W ozone-free xenon bulb (Sutter Instrument, Novato, CA). The images were captured using a sCMOS ORCA-Flash4.0 V2 camera (Hamamatsu Photonics, Hamamatsu, Japan). The FRET images were acquired using a custom filter set comprised of an

mTFP1 excitation filter (ET450/30x; Chroma Technology Corp, Bellows Falls, VT), mTFP1 emission filter (FF02-485/20–25, Semrock, Rochester, NY), Venus excitation filter (ET514/10x; Chroma Technology Corp), Venus emission filter (FF01-571/72; Semrock), and dichroic mirror (T450/514rpc; Chroma Technology Corp). For sensitized emission FRET microscopy, three images are acquired to calculate FRET efficiency.[58] These include imaging the acceptor (I_{AA}, Venus excitation, Venus emission), FRET (I_{DA}, mTFP1 excitation, Venus emission), and donor (I_{DD}, mTFP1 excitation, mTFP1 emission). For immunofluorescent imaging, we utilized the DA/FI/TR/Cy5-4X4 M-C Brightline Sedat filter set (Semrock) and the associated dichroic mirror (FF410/504/582/669-Di01). The motorized filter wheels (Lambda 10-3; Sutter Instrument), automated stage (H117EIX3; Prior Scientific, Rockland, MA), and image acquisition were controlled through MetaMorph Advanced software (Molecular Devices, San Jose, CA). Differential interference contrast (DIC) images were acquired at 60x magnification using a polarizer (IX-LWPO, Olympus) mounted above the condenser, an adjustable DIC slider (U-DICT, Olympus) containing one of the Nomarski prisms, and a mirror unit equipped with the analyzer (IX3-FDICT, Olympus). The Nomarski prism within the DIC slider was adjusted to achieve optimum contrast prior to each experiment.

For live cell imaging of NIH3T3cells, growth media was replaced with DMEMgfp-2 live cell visualization media (MC102; Sapphire North America, Ann Arbor, MI), supplemented with 10% FBS, 30 min before imaging. For live cell imaging of MEFs, growth media was replaced with the same live cell visualization media and supplemented with 10% FBS and 1% NEAA, 30 min before imaging. A constant temperature was maintained across the sample using an objective heater (Objective Heater Medium 150819-13; Bioptechs, Butler, PA) in conjunction with a stage and lid heater (Stable Z System 403–1926; Bioptechs). A humidified CO_2 perfusion system (130708; Bioptechs) was used to maintain a stable pH. All components were brought to thermal equilibrium prior to imaging.

Preparation of methacrylated coverslips and hydrophobic glass substrate

18x18 No. 2 glass coverslips (48368-040; VWR, Radnor, PA) were exposed to air plasma for 5 min. Immediately before addition to glass coverslips, 500 μL of glacial acetic acid (ACROS Organics AC124040010; Thermo Fisher) was added to a solution of 3-(Trimethoxysilyl) propyl methacrylate (M6514-25ML; Sigma-Aldrich) in ethanol (E7023-500ML; Sigma-Aldrich; 30 μL in 9.5 mL). This solution was applied to the coverslips and incubated for 5 min. The coverslips were then washed twice with ethanol and dried via compressed air. Coverslips were prepared < 1h before fabrication of polyacrylamide gels.

A hydrophobic glass substrate was prepared using by first rinsing with DI H_2O, then 70% ethanol in DI H_2O (Sigma-Aldrich), and finally 100% isopropyl-alcohol (BDH-11334LP; VWR International). This was dried via compressed air. Rain-X Original Glass Water Repellent (ITW Global Brands, Houston, TX) was applied to the pre-cleaned glass substrate according to the manufacturer's instructions.

Preparation, imaging, and mechanical testing of PA gels

Polyacrylamide (PA) gels were fabricated using a methodology to improve ECM protein attachment described previously.[59] PA gels of the 5% acrylamide/0.08% bis-acrylamide formulation were prepared using 375 μL of 40% acrylamide solution (1610140; Bio-Rad, Hercules, CA), 120 μL of 2% bis-acrylamide solution (1610142; Bio-Rad), and 2475 μL of DI H_2O. This solution was de-gassed for 10 min via sonication under vacuum. The de-gassed solution was mixed with a 1.5M solution of 2-aminoethyl methacrylate (516155-5G; Sigma-Aldrich) in DI H_2O at a ratio of 1:100. This solution was passed through a 0.2 μm syringe filter (VWR) to remove any particulate. This solution was mixed with a 100 mg/mL solution of Irgacure-2959 (410896-10G; Sigma-Aldrich) in methanol (VWR) at a ratio of 1:100. 240 μL of this solution was pipetted onto a hydrophobic glass substrate (see above). A methacrylated coverslip (see above) was inverted onto the droplet of PA solution and exposed to UV light for 15 min. Following polymerization, the glass substrate was flooded with PBS and the gel-attached coverslips were gently removed. Gels were placed in a 6-well plate and washed twice with PBS. Following washing, a working solution of 0.83 mg/mL solution of sulfosuccinimidyl 6-(4′-azido-2′-nitrophenylamino) hexanoate (sulfo-SANPAH, 22589; Thermo Fisher) in PBS was prepared from a stock solution of 83 mg/mL sulfo-SANPAH in DMSO (Sigma-Aldrich). The working solution was pipetted onto the surface of each gel, ensuring complete coverage. The gels were then exposed to UV light for 5 min. The gels were rinsed twice with PBS and covered with a 10 μg/mL solution of fibronectin in PBS (for gels to be used for cell attachment) or 10 μg/mL BSA in PBS (to reduce non-specific adhesion for gels to be used in mechanical testing) prior to incubation overnight at 4°C.

For imaging, gels were kept in a 6-well dish. The fibronectin in PBS solution was changed to full MEF growth media prior to seeding cells. MEFs (stably expressing VinTS or VinTS-E1015A-E1021A) were seeded at approximately 5700 cells/cm^2 and allowed to adhere for 24h prior to fixation. Following fixation, the gels were stored in PBS until imaging. No. 1.5 glass coverslips were mounted in reusable metal dishes (Bioptechs, Butler, PA). A 50 μL droplet of PBS was added to the coverslip and the gel was carefully inverted onto the droplet. Imaging was performed in this configuration.

Mechanical testing of PA gels was performed via atomic force microscopy (Asylum Research MFP 3D, Santa Barbara, CA). Hydrogels were immersed in PBS and indented with a spherical cantilever (10 μm radius, borosilicate glass, Novascan Technologies, Ames, IA) with a spring constant of 188.39 pN/nm at an indentation speed of 0.8 μm/s. Young's modulus was determined via Hertzian model fit. The Young's modulus for the PA gel formulation used in this study was determined to be 3.5 kPa (Figure S22).

Mathematical models of FP mechanical switching in MTS

The formulation and implementation of the mathematical models of FP mechanical switching in load-bearing proteins and MTSs are provided in Note S1.

Steered molecular dynamics simulations of FPs

The methods for SMD simulations of FPs are provided in Note S2.

QUANTIFICATION AND STATISTICAL ANALYSIS

Calculation of FRET efficiency and stoichiometry from sensitized emission

FRET was detected through measurement of sensitized emission[27] and calculated using custom written code in MATLAB (Mathworks).[58] All analyses were conducted on a pixel-by-pixel basis. Prior to FRET calculations, all images were first corrected for dark current, uneven illumination, background intensity, and three-dimensional offsets caused by chromatic aberrations and minute hardware misalignments (registration) as previously described.[28] Spectral bleedthrough coefficients were determined through FRET-imaging of cells expressing only donor or only acceptor FPs. The donor bleedthrough coefficient (*dbt*) was calculated for mTFP1 as:

$$dbt = \langle \frac{I_{DA}}{I_{DD}} \rangle$$

where I_{DA} is the intensity in the FRET-channel, I_{DD} is the intensity in the donor-channel, and data were binned by donor-channel intensity. Similarly, the acceptor bleedthrough coefficient (*abt*) was calculated for Venus (A206K) as:

$$abt = \langle \frac{I_{DA}}{I_{AA}} \rangle$$

where I_{AA} is the intensity in the acceptor-channel, and data were binned by acceptor-channel intensity. For the mTFP1-Venus (A206K) FP pair on our microscope setup, the cross-talk between donor and acceptor channels (signal from donor in acceptor channel and vice-versa) was determined to be negligeable. To correct for spectral bleedthrough in experimental data, pixel-by-pixel FRET corrections were performed according to the equation:

$$I_{DA,corr} = I_{DA} - dbt \cdot I_{DD} - abt \cdot I_{AA}$$

where $I_{DA,corr}$ is the corrected FRET intensity (also defined in the literature as F_c). After bleedthrough correction, FRET efficiency was calculated. Through imaging donor-acceptor fusion constructs of differing, but constant, FRET efficiencies, it is possible to calculate two proportionality constants that enable the calculation of FRET efficiencies for a given FRET pair.[27] These proportionality constants are *G*:

$$G = -\frac{\Delta\left(\frac{I_{DA,corr}}{I_{AA}}\right)}{\Delta\left(\frac{I_{DD}}{I_{AA}}\right)}$$

where Δ indicates the change between two donor-acceptor fusion proteins, and *k*:

$$k = \frac{I_{DD} + \frac{I_{DA,corr}}{G}}{I_{AA}}$$

Using published methods,[28] the calibration factors were experimentally determined for mTFP1 and Venus (A206K). With these two proportionality constants, it is possible to calculate both the apparent FRET efficiency (E_{app}):

$$E_{app} = \frac{I_{DA,corr}}{I_{DA,corr} + G \cdot I_{DD}}$$

and FP stoichiometry[29] (S_{app}):

$$S_{app} = \frac{I_{DA,corr} + G \cdot I_{DD}}{I_{DA,corr} + G \cdot I_{DD} + G \cdot k \cdot I_{AA}}$$

The calibration constants *G* and *k* were monitored over the course of this work to control for changes in lamp and filter performance. Note, these formulas are equivalent to the formulas from Coulomb et al.[29] with $\alpha^{BT} = dbt$, $\delta^{DE} = abt$, $\gamma^{M} = G$, and $\beta^{X} = \frac{1}{G \cdot k}$:

$$I_{DA,corr} = I_{DA} - \alpha_{BT} \cdot I_{DD} - \delta_{DE} \cdot I_{AA}$$

$$E_{app} = \frac{I_{DA,corr}}{I_{DA,corr} + \gamma^{M} \cdot I_{DD}}$$

$$S_{app} = \frac{I_{DA,corr} + \gamma^M \cdot I_{DD}}{I_{DA,corr} + \gamma^M \cdot I_{DD} + \frac{I_{AA}}{\beta^X}}$$

Note that all experimental FRET measurements are inherently apparent FRET efficiency (E_{app}) and FP stoichiometry (S_{app}), but are indicated for experimental data in this work using E and S without the subscript to match previous conventions.[16,27,28,34]

To analyze E and S, the following approaches were used to generate analysis masks. For ABDTS and ABDTL, analysis masks were constructed for whole cells. Cell masks were manually drawn using DIC images (for live imaging) or phalloidin-labeled actin images (for fixed imaging). Cell masks were refined by excluding pixels in which the intensity of both I_{AA} and I_{DD} was below a small threshold value (exclude px if $I_{AA} < 50$ and $I_{DD} < 50$). This condition preserves regions containing signal from both or a single FP. For VinTS variants, analysis masks contained all pixels in the FAs of single cells. Segmentation of FAs was done as previously reported using a water-based algorithm.[58] Segmentation and manual cell mask generation for VinTS variants were performed using the acceptor channel, which is independent of FRET, as previously described.[38]

For ES-histogram analyses, all pixels in the above-described analysis mask were used. E outside [0.000, 0.500] and S outside [0.000, 1.000] were set to the nearest limit. ES-histograms were constructed with fixed bin widths. For single cells, pixel counts were plotted, and bin widths of 0.005 for E and 0.010 for S were used. For cell populations, histograms show the average of the relative fraction of each bin across cells in the indicated group, which gives each cell in the population an equal waiting regardless of its size (number of pixels in analysis mask). Here, bin widths of 0.025 for E and 0.050 for S were used. To quantitatively compare the extent of acceptor FP mechanical switching between groups or conditions, the fraction of pixels in a larger bin containing low E values and high S values was quantified for each cell. Specifically, we quantified the fraction of pixels in each cell with $E < 0.15$ and $S > 0.60$.

Computation of cell and FA morphology metrics

Cell and FA morphology was analyzed for the VinTS dataset. Cell masks were used to compute cell morphology metrics. FA masks were used to compute FA morphology metrics. All morphology metrics were computed using the MATLAB "regionprops" function. The following cell morphology metrics were used: cell area (A), cell perimeter (P), cell form factor ($4\pi A/P^2$), cell eccentricity (ratio of the distance between the center and one foci to the length of the semi-major axis for the fitted ellipse), and cell solidity (A/[*Convex Hull Area*]). The following FA morphology metrics were used: number of FAs in the cell, mean area of FAs in the cell, standard deviation of area of FAs in the cell, mean eccentricity of FAs in the cell, and standard deviation of eccentricity of FAs in the cell. For all analyses, FAs smaller than 16 px or 0.1866 μm^2 were discarded as done previously.[14]

Statistical analysis

Statistical analyses were performed using JMP Pro (SAS, Cary, NC) software. Normality of each dataset was assessed using Q-Q plots and Shapiro-Wilks test. For normal datasets, comparisons of data with equal variances, as determined with Levene's test, were analyzed with an ANOVA and, if necessary, Tukey's Honest Significant Difference (HSD) tests. Datasets with unequal variances were analyzed with a non-parametric Welch's ANOVA and, if necessary, the Steel-Dwass multiple comparisons test. For non-normal datasets, comparisons of data were analyzed with a Kruskal-Wallis test and, if necessary, Steel-Dwass multiple comparisons test. A p value of $p < 0.05$ was considered statistically significant. In figures, a single asterisk (*), double asterisk (**), triple asterisk (***), and quadruple asterisk (****) indicate p-values less than 0.05, 0.01, 0.001, and 0.0001, respectively, and ns indicates a p-value greater than or equal to 0.05. Cells were treated as independent observations. Sample sizes for each experiment can be found in the figure legends. Where used, standard boxplots were created using JMP Pro, where the bottom and top of the box indicate the first and third quartiles, respectively, the middle line indicates the median, the whiskers extend to the outermost data points below the first quartile and above the third quartile that are within 1.5 times the interquartile range, and data outside the whiskers are indicated as points.

Cell Reports Methods, Volume *4*

Supplemental information

Detection of fluorescent protein mechanical switching *in cellulo*

T. Curtis Shoyer, Kasie L. Collins, Trevor R. Ham, Aaron T. Blanchard, Juilee N. Malavade, Benjamin A. Johns, Jennifer L. West, and Brenton D. Hoffman

Supplemental Information

This document contains the following supplemental information:

- Supplemental Figures S1-S22
- Supplemental Note S1, containing Supplemental Tables S1-S4
- Supplemental Note S2
- Supplemental Note S3, containing Supplemental Tables S5-S9
- Supplemental References

Supplemental Figures

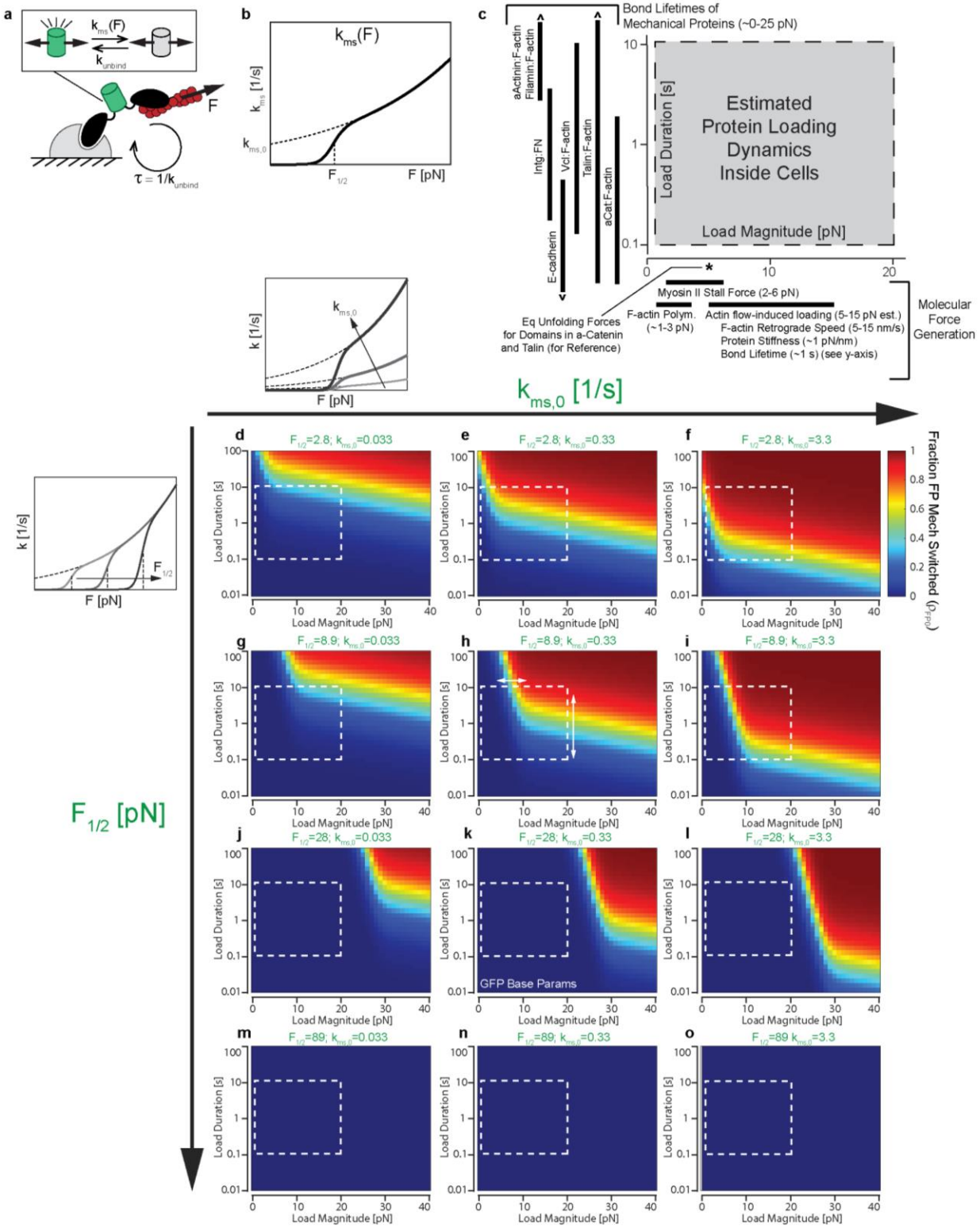

Figure S1, related to Figure 1. Model of FP Mechanical Switching in a Load-bearing Protein. (a) Schematic of model of a single FP integrated into a dynamic load-bearing protein. The protein is loaded by an actin structure to which it binds/unbinds. The FP is in the line of loading and can reversibly switch

between functional (state 1) and non-functional (state 0) states in a force-sensitive manner. (b) Force-dependent rate constant for mechanical switching. (c) Estimated range of protein loading magnitude (x-axis) and duration (y-axis) inside cells, based on literature values for molecular force generation and bond lifetimes of mechanical proteins, respectively. See the text of Note S1 for citations. (d-o) Contour plots of the steady state fraction of FPs that have undergone mechanical switching (ρ_{FP0}) as a function of load magnitude (F) and load duration (τ). Each plot corresponds to the indicated FP mechanical switching parameter combination ($F_{1/2}$ and $k_{MS,0}$). All other parameters were set to the base values indicated in Table S1. The white dashed box in (d)-(o) indicate the estimated ranges of load magnitude and load duration experienced by proteins in cells that is originally shown in (c).

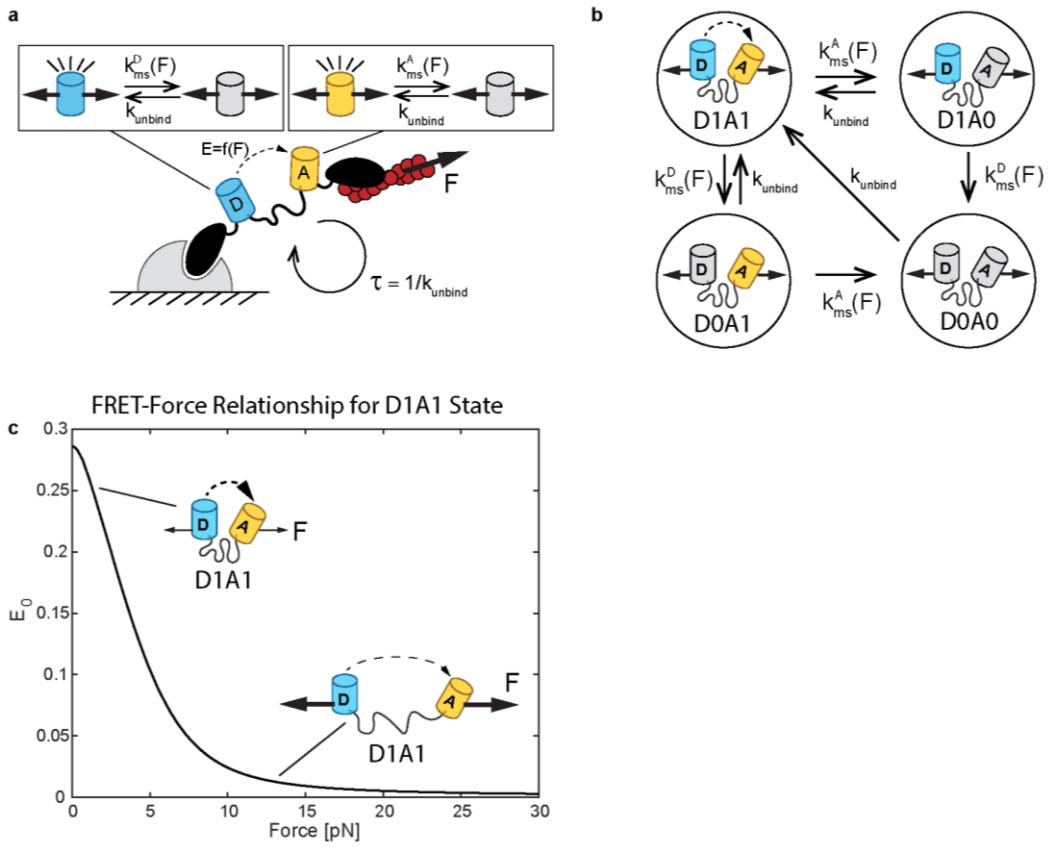

Figure S2, related to Figure 1. Model Formulation of FP Mechanical Switching in MTS. (a) Schematic of model of FP mechanical switching inside an MTS. The MTS is loaded by an actin structure to which it binds/unbinds. Donor and acceptor FPs are in the line of loading and can reversibly switch between functional (state 1) and non-functional (state 0) states in a force-sensitive manner. (b) Four possible MTS states based on the status of the donor and acceptor FP, with arrows indicating state transitions and the associated rate constant. (c) FRET-force relationship, $E_i = f(F_i)$, for an MTS in the D1A1 state. The FRET-force relationship shown is the previously determined calibration curve for the original TSMod, mTFP1-$(GPGGA)_8$-mVenus, which is used to convert experimental measurements of FRET Efficiency into molecular tension [S1, S2].

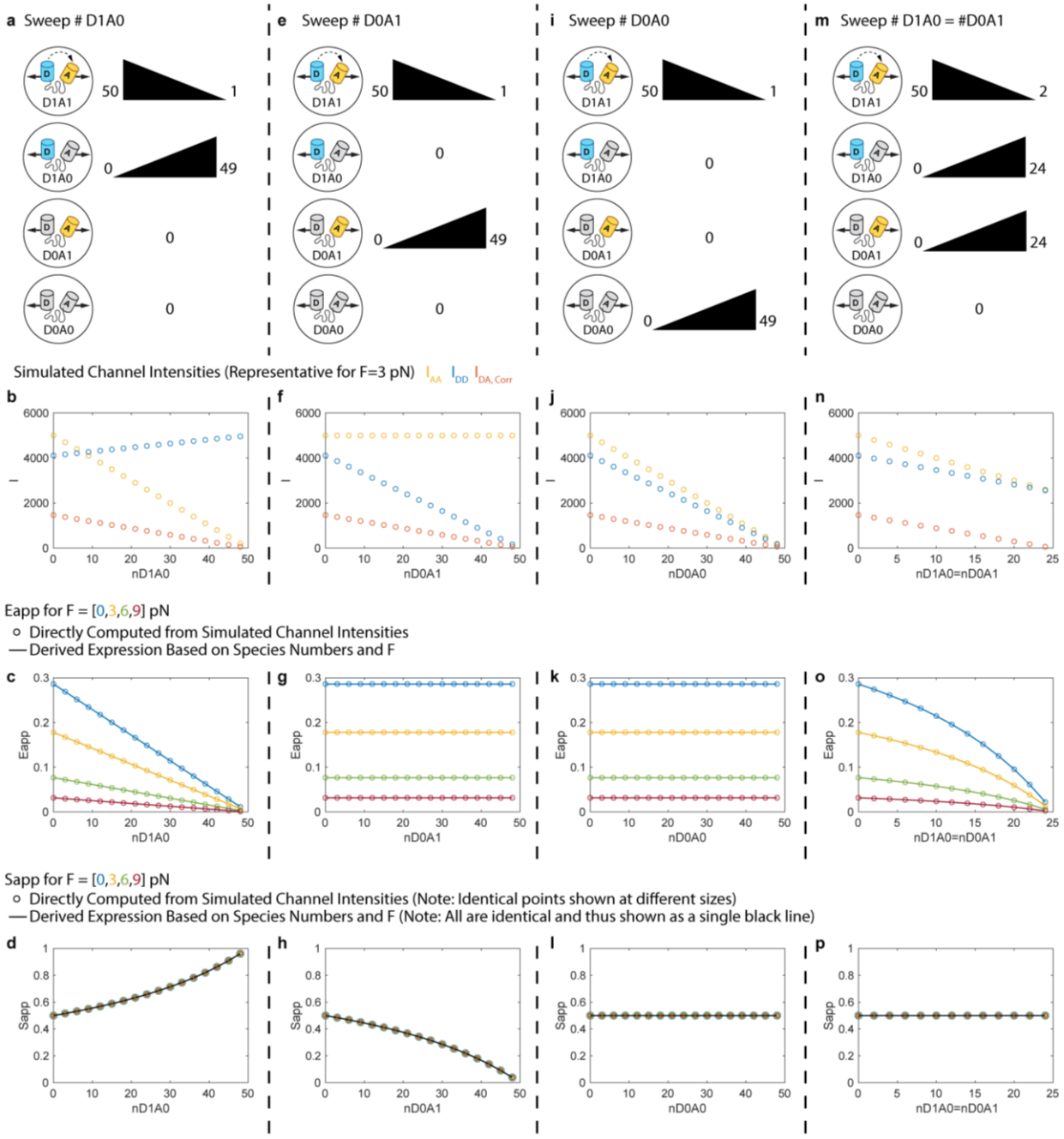

Figure S3, related to Figure 1. Validation of Derived Expressions for E_{app} and S_{app} by Comparison to Direct Simulation of Channel Intensities. The derived expressions for E_{app} and S_{app} (Note S1, Equations S18 and S19) for a population of MTSs comprised of a distribution of sensor states and all under the same force magnitude (F) were validated by comparison to direct computations from simulated channel intensities (Note S1, Equations S12-S17. (a-d) Effect of increasing the number of sensors in the D1A0 state (n_{D1A0}) from 0 to 49, with the remaining sensors in the D1A1 state (to a total of 50). (b) Intensities for the acceptor channel (I_{AA}^{TOT}; Equation S12), donor channel (I_{DD}^{TOT}; Equation S13), and corrected FRET channel ($I_{DA\,corr}^{TOT}$; Equation S15) versus n_{D1A0} for F of 3 pN. (c) Plot of E_{app} computed directly from channel intensities (dots; Equation S16) or derived expression (line; Equation S18) versus n_{D1A0} for four values of F. (d) Plot of S_{app} computed directly from channel intensities (dots; Equation S17) or derived

expression (line; Equation S19) versus n_{D1A0} for four values of F. (e-h) Same set of plots for increasing the number of sensors in the D0A1 state (n_{D0A1}) from 0 to 49 with remaining sensors in the D1A1 state. (i-l) Same set of plots for increasing the number of sensors in the D0A0 state (n_{D0A0}) from 0 to 49 with remaining sensors in the D1A1 state. (m-q) Same set of plots for jointly increasing the number of sensors in the D1A0 and D0A1 states ($n_{D1A0} = n_{D0A1}$) from 0 to 24 with remaining sensors in the D1A1 state. Simulated channel intensities and direct computations from simulated channel intensities were performed with the following three-channel FRET parameters: $\widehat{\alpha_{BT}} = 0.75, \widehat{\delta^{DE}} = 0.25, \widehat{\gamma^{M}} = 1.65, \widehat{\beta^{X}} = 0.6061$, and $C_{AA} = 100$.

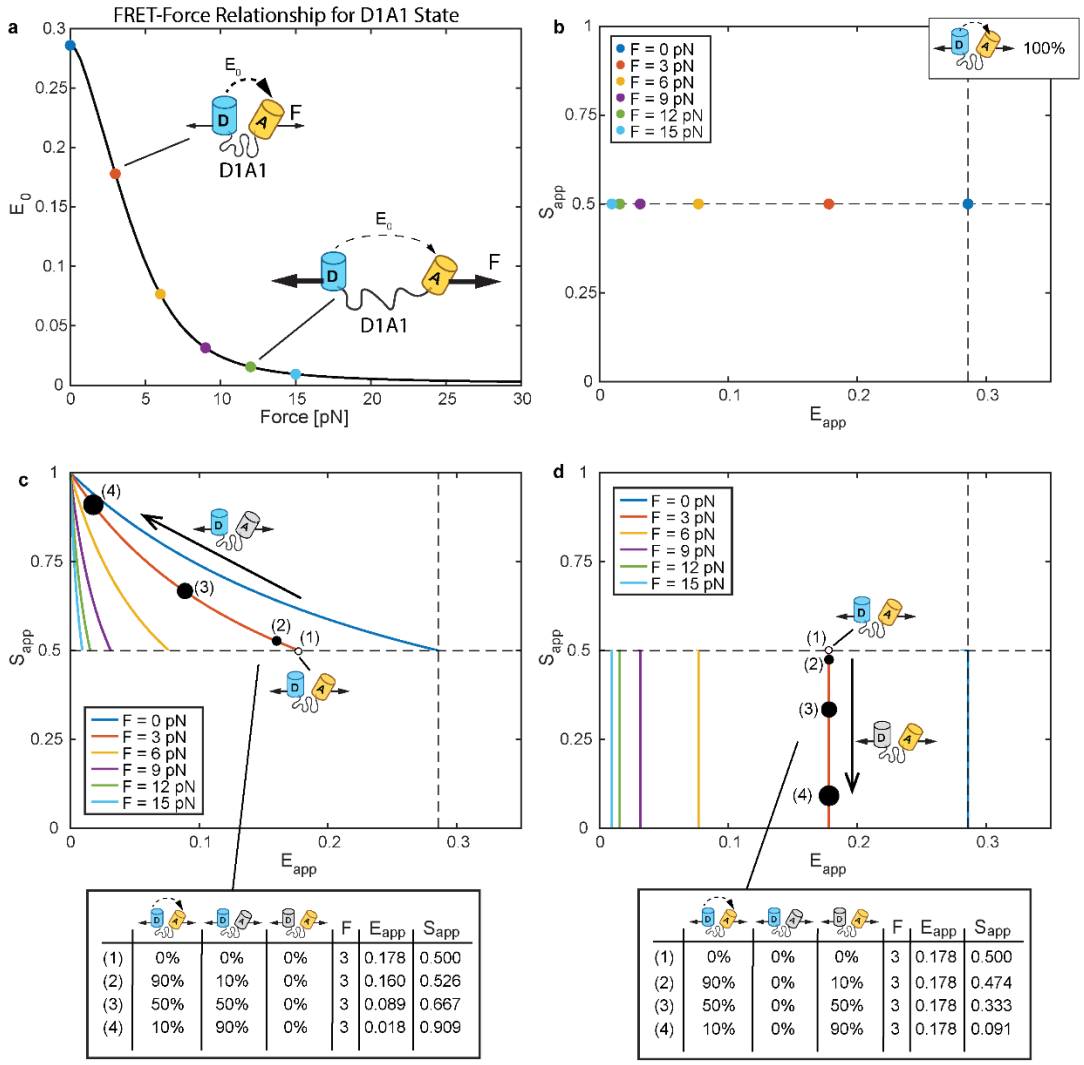

Figure S4, related to Figure 1. Extension of ES-Histogram Framework to MTSs with FP Mechanical Switching. (a) FRET-force relationship, $E_i = f(F_i)$, for an MTS in the D1A1 state, with dots indicating force magnitudes (F) of 0, 3, 6, 9, 12, and 15 pN. These force magnitudes are also indicated in the subsequent panels. (b) ES-Histogram for MTS ensemble comprised of 100% sensors in the D1A1 state and all sensors subject to the indicated F. (c) (E_{app}, S_{app})-curves ("tension isoclines") for MTS ensembles comprised of various amounts of sensors in the D1A1 and D1A0 state (i.e. varying levels of acceptor mechanical switching only) with all sensors subject to the indicated F. Bottom right of each solid line (tension isocline) corresponds to 100% D1A1 state and top left approaches the limit of 100% D1A0 state. Three dots provide references indicating 90%:10%, 50%:50%, and 10%:90% sensors in D1A1:D1A0 state, respectively. (d) (E_{app}, S_{app})-curves for MTS ensembles comprised of various amounts of sensors in the D1A1 and D0A1 state (i.e. varying levels of donor mechanical switching only) with all sensors subject to the indicated F. Top of each solid line (tension isocline) corresponds to 100% D1A1 state and bottom approaches the limit of 100% D0A1 state. Three dots provide references indicating 90%:10%, 50%:50%, and 10%:90% sensors in D1A1:D0A1 state, respectively.

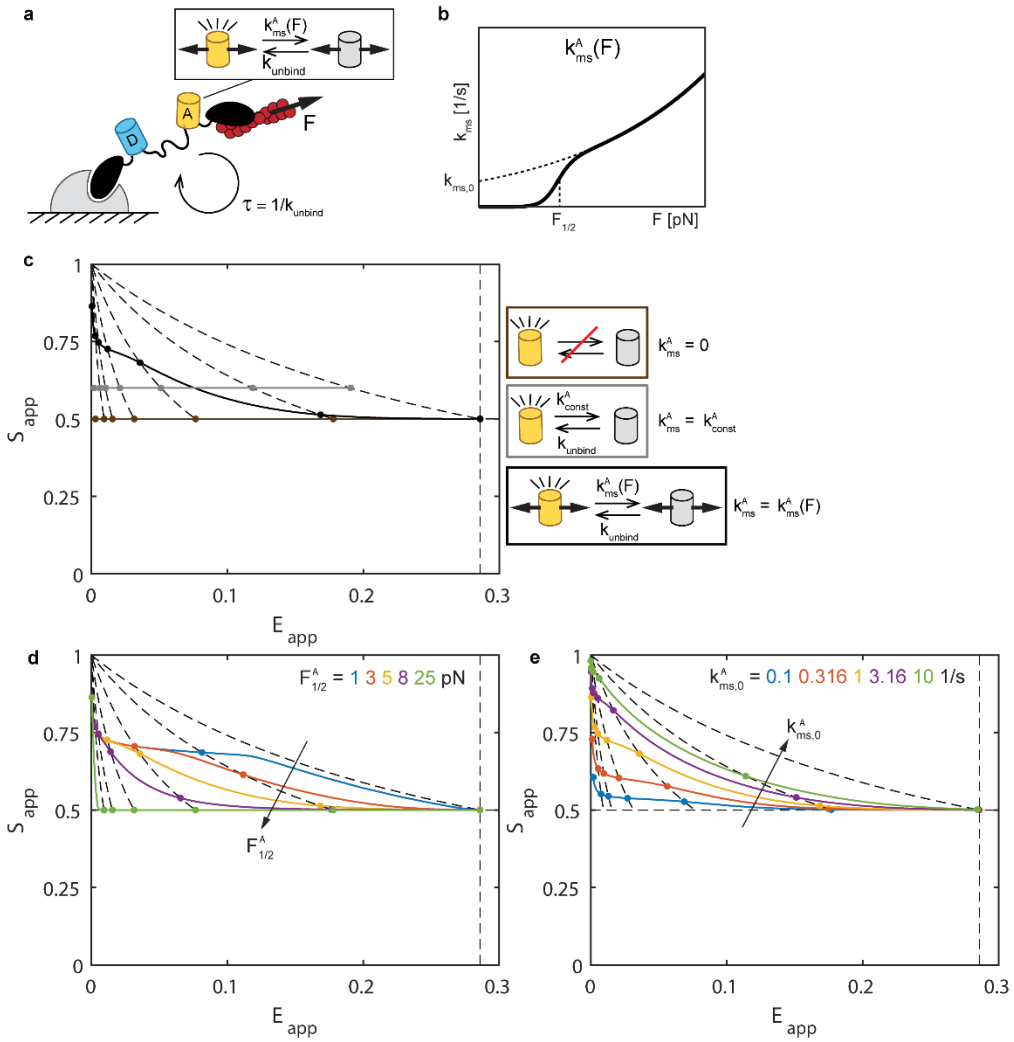

Figure S5, related to Figures 2 and 3. Effect of Acceptor Mechanical Switching in MTS. (a) Schematic of MTS with acceptor mechanical switching only. (b) Force-dependent rate constant for acceptor mechanical switching. (c) (E_{app}, S_{app})-curves for MTS ensembles without acceptor mechanical switching [$k_{MS}^{A}(F) = 0$], force-independent acceptor loss-of-function [$k_{MS}^{A}(F) = k_{MS,0}^{A} = 1/s$; e.g. due to photobleaching or large differences in FP maturation time], and acceptor mechanical switching [$k_{MS}^{A}(F)$ with base parameter values in Table S2] for a range of F from 0 to 30 pN. (d) (E_{app}, S_{app})-curves for different $F_{1/2}^{A}$ (and corresponding m^{A} in Table S2). (e) (E_{app}, S_{app})-curves for different $k_{MS,0}^{A}$. In all plots, reference dots indicate F of 0, 3, 6, 9, 12, 15, and 30 pN (from right-to-left) and reference black dashed lines are tension isoclines for acceptor only mechanical switching at F of 0, 3, 6, 9, 12, and 15 pN (from right-to-left). Except where indicated, all parameters are set to base values indicated in Table S2 and there is no donor mechanical switching [$k_{MS}^{D}(F) = 0$].

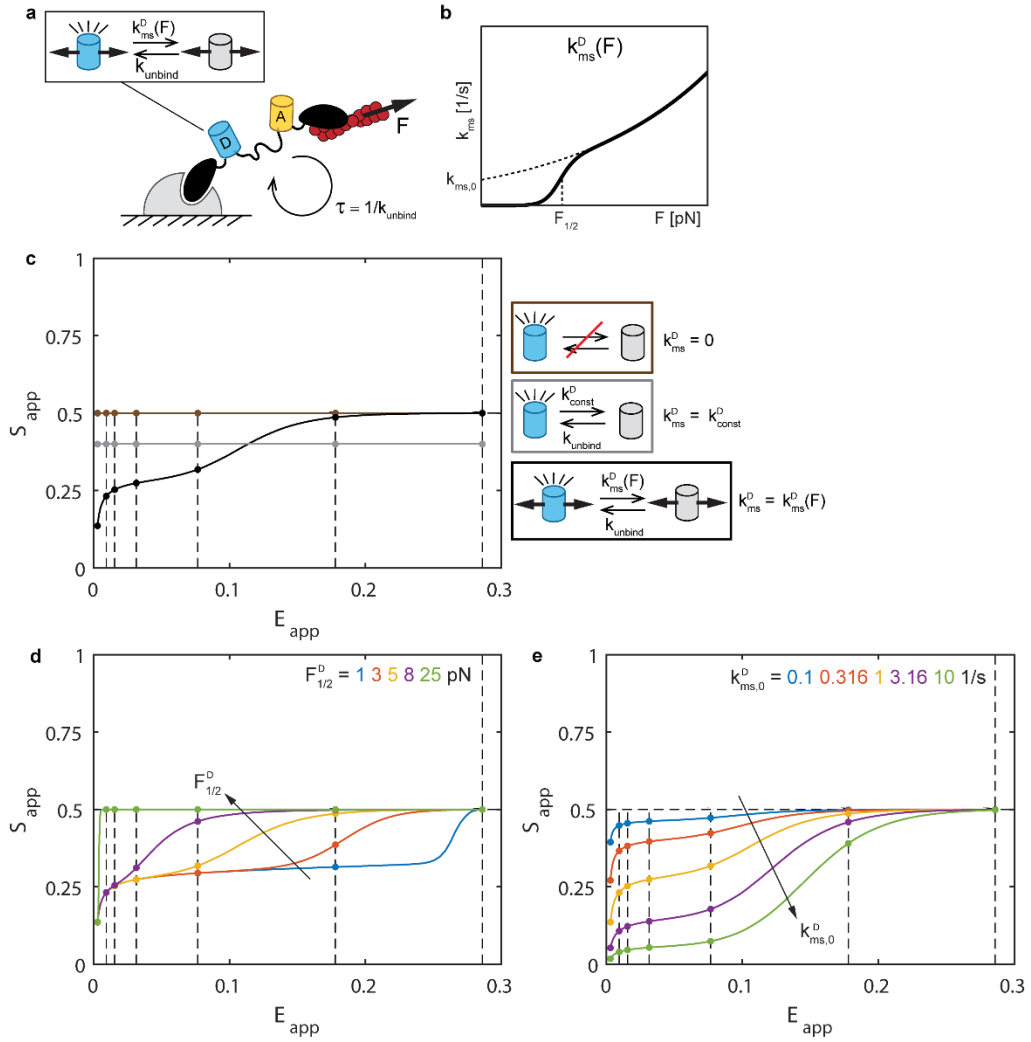

Figure S6, related to Figures 2 and 3. Effect of Donor Mechanical Switching in MTS. (a) Schematic of MTS with donor mechanical switching only. (b) Force-dependent rate constant for donor mechanical switching. (c) (E_{app}, S_{app})-curves for MTS ensembles without donor mechanical switching [$k_{MS}^{D}(F) = 0$], force-independent donor loss-of-function [$k_{MS}^{D}(F) = k_{MS,0}^{D} = 1/s$; e.g. due to photobleaching or large differences in FP maturation time], and donor mechanical switching [$k_{MS}^{D}(F)$ with base parameter values in Table S2] for a range of F from 0 to 30 pN. (d) (E_{app}, S_{app})-curves for different $F_{1/2}^{D}$ (and corresponding m^{D} in Table S2). (e) (E_{app}, S_{app})-curves for different $k_{MS,0}^{D}$. In all plots, reference dots indicate F of 0, 3, 6, 9, 12, 15, and 30 pN (from right-to-left) and reference black dashed lines are tension isoclines for donor only mechanical switching at F of 0, 3, 6, 9, 12, and 15 pN (from right-to-left). Except where indicated, all parameters are set to base values indicated in Table S2 and there is no acceptor mechanical switching [$k_{MS}^{A}(F) = 0$].

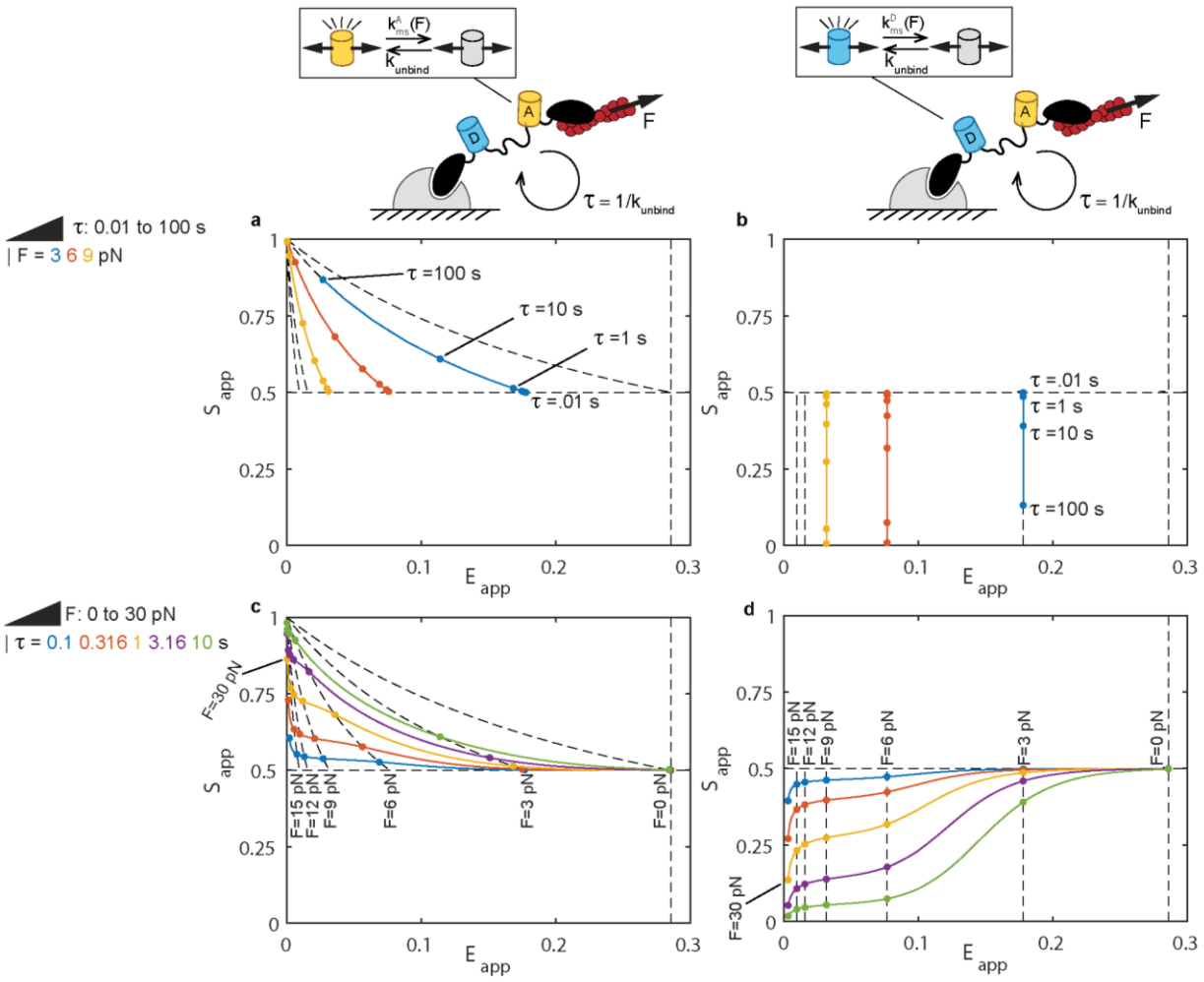

Figure S7, related to Figures 2 and 3. Comparison on Variations in Load Magnitude versus Load Duration. (a) For acceptor mechanical switching only [$k_{MS}^{A}(F)$ with base parameter values in Table S2 and $k_{MS}^{D}(F) = 0$], (E_{app}, S_{app})-curves for variation of load duration τ from 0.01 to 100 seconds at three different F values. Dots indicate select τ values for reference. (b) Same for donor mechanical switching only [$k_{MS}^{D}(F)$ with base parameter values in Table S2 and $k_{MS}^{A}(F) = 0$]. (c) For acceptor mechanical switching only [$k_{MS}^{A}(F)$ with base parameter values in Table S2 and $k_{MS}^{D}(F) = 0$], (E_{app}, S_{app})-curves for variation of F from 0 to 30 pN at five different τ values. Dots indicate select F values for reference. (d) Same for donor mechanical switching only [$k_{MS}^{D}(F)$ with base parameter values in Table S2 and $k_{MS}^{A}(F) = 0$]. In all plots, black dashed lines are tension isoclines for acceptor only or donor only mechanical switching at F of 0, 3, 6, 9, 12, and 15 pN. Except where indicated, all parameters are set to base values indicated in Table S2.

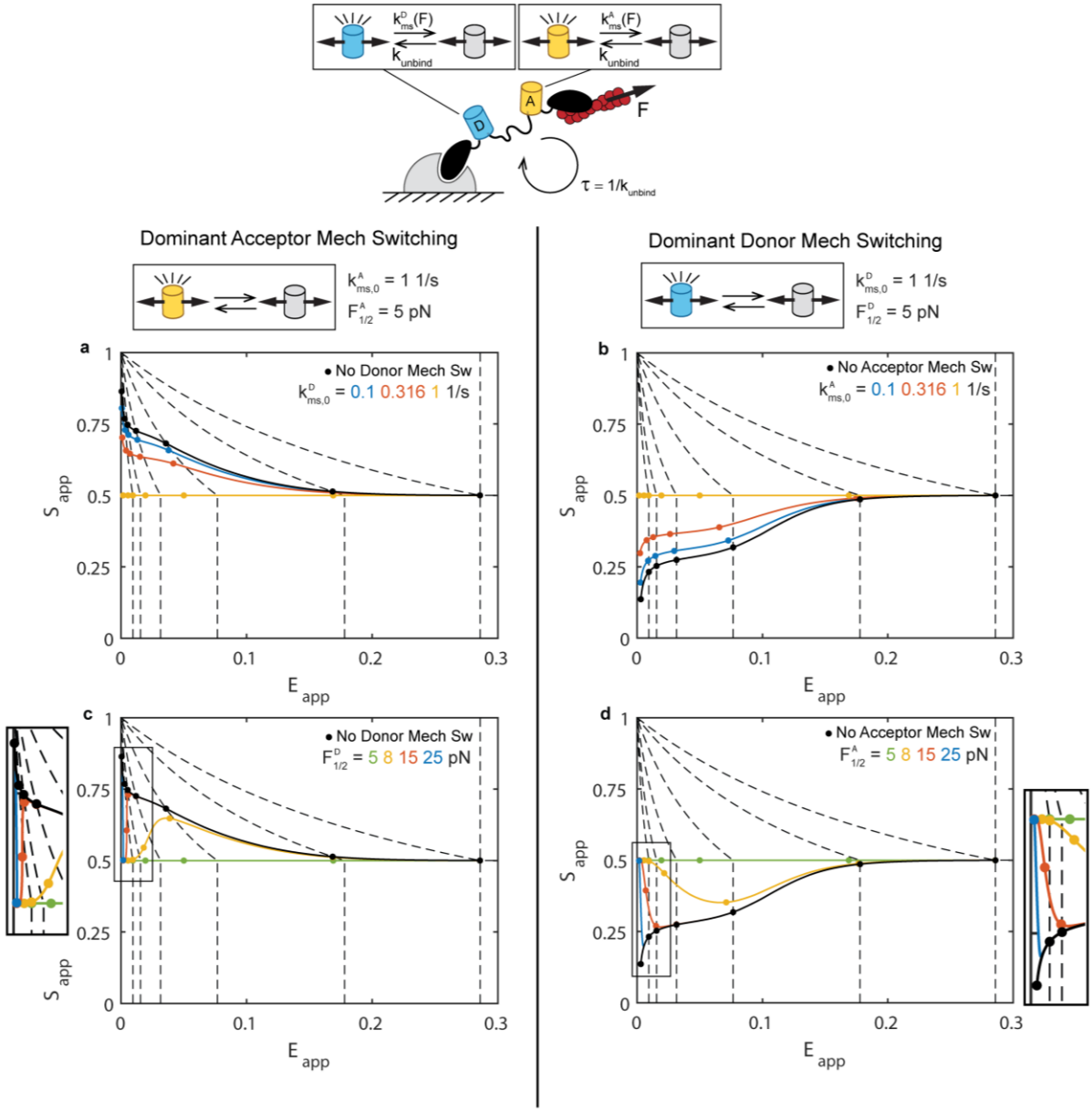

Figure S8, related to Figures 2 and 3. Dominant Mechanical Switching in One FP is Detectable In Presence of Weaker Mechanical Switching in the Other FP. (a) For base acceptor mechanical switching [$k_{MS}^{A}(F)$ with base parameter values in Table S2], (E_{app}, S_{app})-curves for donor mechanical switching at different values of $k_{MS,0}^{D}$. (b) For base donor mechanical switching [$k_{MS}^{D}(F)$ with base parameter values in Table S2], (E_{app}, S_{app})-curves for acceptor mechanical switching at different values of $k_{MS,0}^{A}$. (c) For base acceptor mechanical switching [$k_{MS}^{A}(F)$ with base parameter values in Table S2], (E_{app}, S_{app})-curves for donor mechanical switching at different values of $F_{1/2}^{D}$ (and corresponding m^{D} in Table S2). (d) For base donor mechanical switching [$k_{MS}^{D}(F)$ with base parameter values in Table S2], (E_{app}, S_{app})-curves for acceptor mechanical switching at different values of $F_{1/2}^{A}$ (and corresponding m^{A} in Table S2). In all plots, reference dots indicate F of 0, 3, 6, 9, 12, 15, and 30 pN (from right-to-left) and reference black dashed lines are tension isoclines for F of 0, 3, 6, 9, 12, and 15 pN (from right-to-left). Except where indicated, all parameters are set to base values indicated in Table S2.

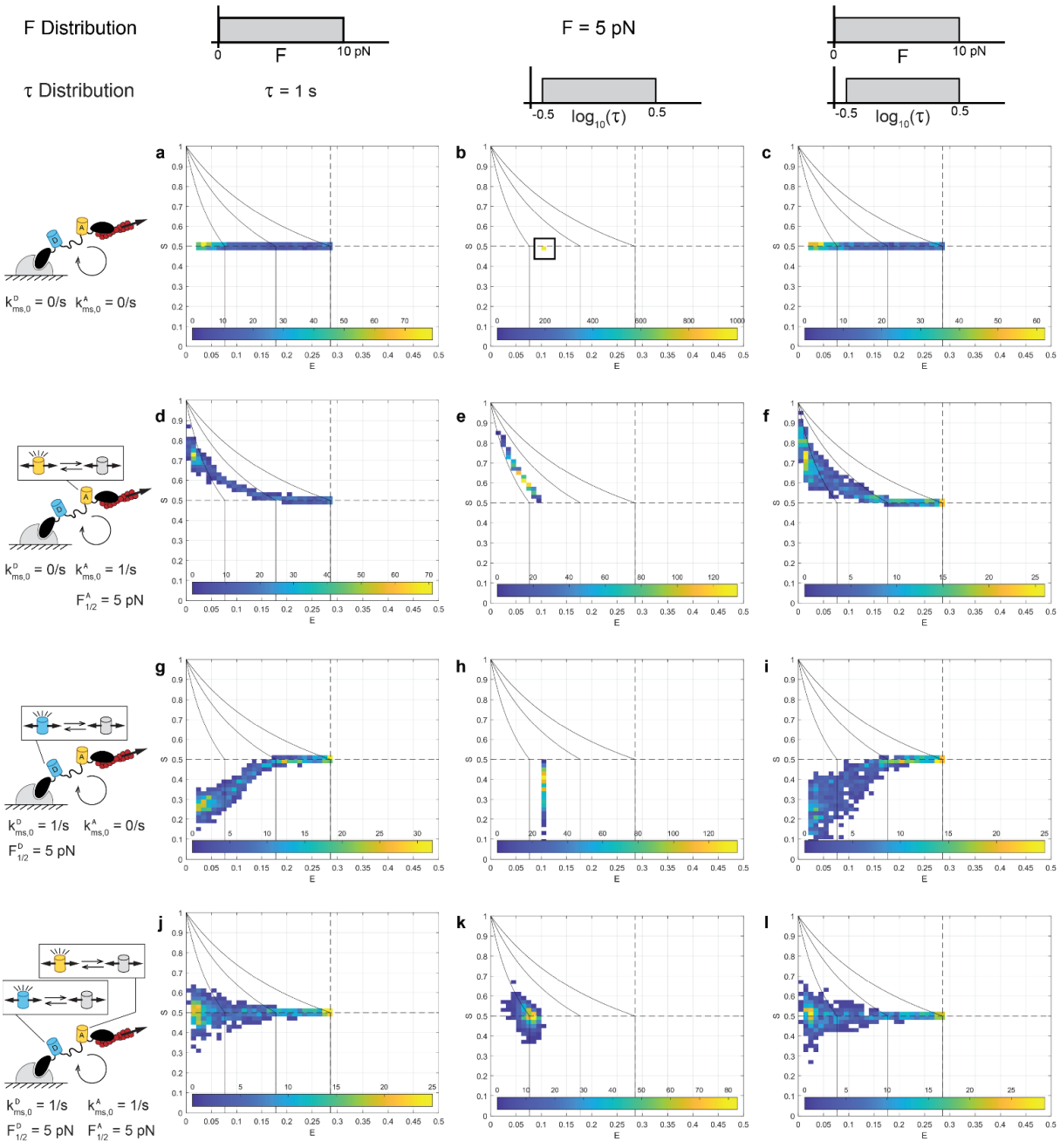

Figure S9, related to Figures 2 and 3. Representative ES-Histograms for Stochastic Simulations. For no FP mechanical switching [$k_{MS}^{A}(F) = k_{MS}^{D}(F) = 0$], ES-Histogram of 1000 simulated MTS ensembles ($N_{sims} = 1000$), each comprised of 50 total sensors ($n_{sensors} = 50$) subject to (a) a single F value drawn from a uniform distribution between 0 and 10 pN and a single τ value of 1 s, (b) a single F value of 5 pN and a single τ value drawn from a log-uniform distribution from $10^{-0.5}$ to $10^{0.5}$ s, or (c) a single F value drawn from a uniform distribution between 0 and 10 pN and a single τ value drawn from a log-uniform distribution from $10^{-0.5}$ to $10^{0.5}$ s. (d-f) Same for acceptor only mechanical switching [$k_{MS}^{A}(F)$ with base parameter values in Table S2 and $k_{MS}^{D}(F) = 0$]. (g-i) Same for donor only mechanical switching [$k_{MS}^{D}(F)$ with base parameter values in Table S2 and $k_{MS}^{A}(F) = 0$]. (j-l) Same for acceptor and donor mechanical switching with identical parameters [$k_{MS}^{A}(F)$ and $k_{MS}^{D}(F)$ with base parameter values in Table S2]. The

color bars indicate bin counts. In all plots, reference black lines are tension isoclines for acceptor only or donor only mechanical switching at F of 0, 3, and 6 pN (from right-to-left). Note that within single MTS ensembles, all sensors are subject to the same F and τ values. A subset of the data in this figure are repeated from Figure 2 and Figure 3.

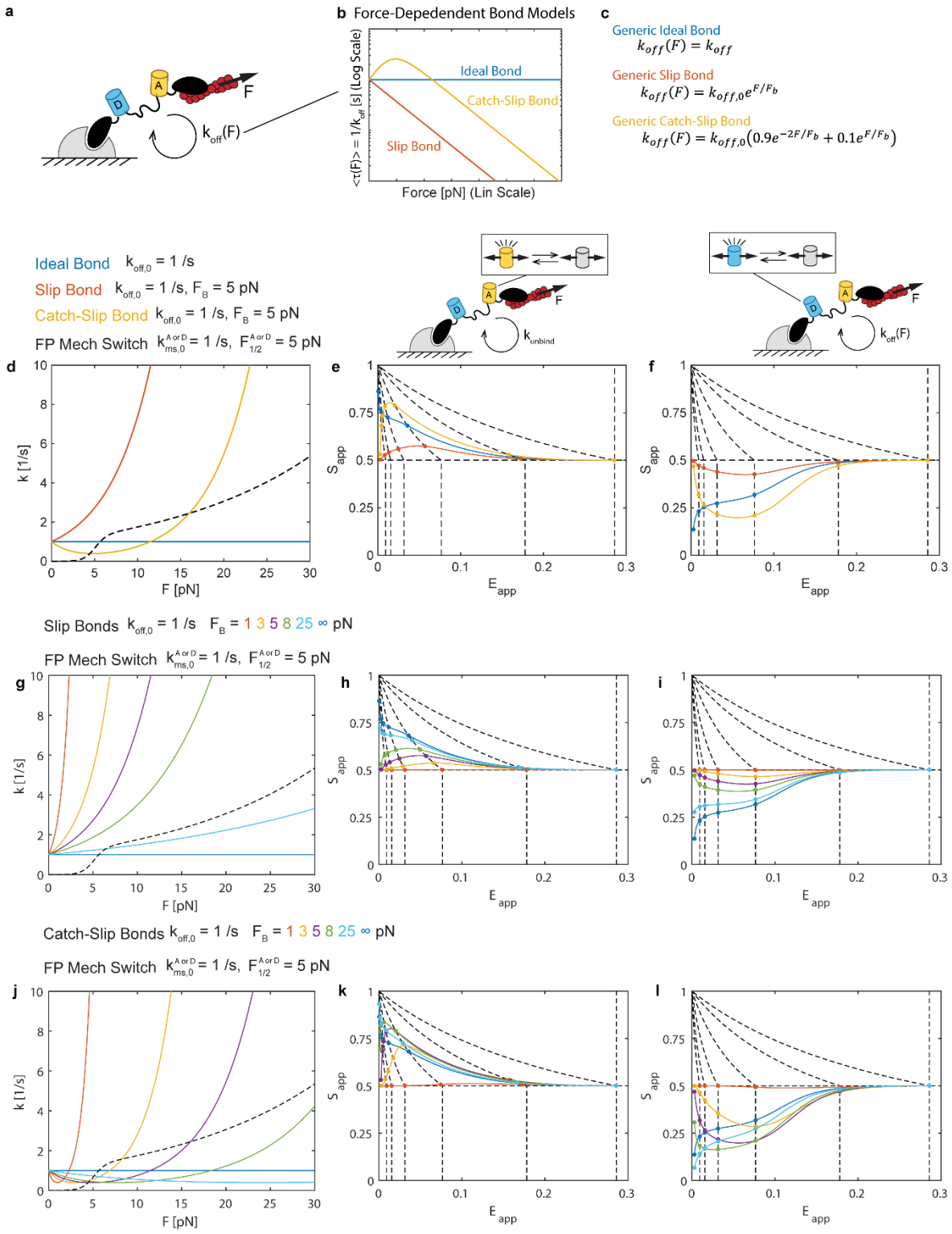

Figure S10, related to Figures 2 and 3. Effect of Force-Dependent Bonds on FP Mechanical Switching in MTS. (a) Schematic of MTS with turnover driven by force-dependent unbinding. (b) Mean lifetime versus force and (c) force-dependent unbinding rate constant expressions for generalized ideal, slip, and catch-slip bonds. (d) Force-dependent unbinding rate constants for three bond types at indicated parameters (matched intrinsic rate constant and exponential parameters), shown with the FP mechanical switching

rate constant for comparison. (e) For acceptor mechanical switching only [$k_{MS}^{A}(F)$ with base parameter values in Table S2 and $k_{MS}^{D}(F) = 0$], (E_{app}, S_{app})-curves for the different unbinding rate constants in (d) for a range of F from 0 to 30 pN. (f) Same for donor mechanical switching only [$k_{MS}^{D}(F)$ with base parameter values in Table S2 and $k_{MS}^{A}(F) = 0$]. (g) Force-dependent unbinding rate constants for slip bonds with different F_B values and the FP mechanical switching rate constant shown for comparison. For (h) acceptor or (i) donor only mechanical switching, (E_{app}, S_{app})-curves for the different unbinding rate constants in (g) for a range of F from 0 to 30 pN. (j) Force-dependent unbinding rate constants for catch-slip bonds with different F_B values and the FP mechanical switching rate constant shown for comparison. For (k) acceptor or (l) donor only mechanical switching, (E_{app}, S_{app})-curves for the different unbinding rate constants in (j) for a range of F from 0 to 30 pN. In (e-f,h-i,k-l), reference dots indicate F of 0, 3, 6, 9, 12, 15, and 30 pN (from right-to-left) and reference black dashed lines are tension isoclines for acceptor or donor only mechanical switching at F of 0, 3, 6, 9, 12, and 15 pN (from right-to-left). Except where indicated, all parameters are set to base values indicated in Table S2.

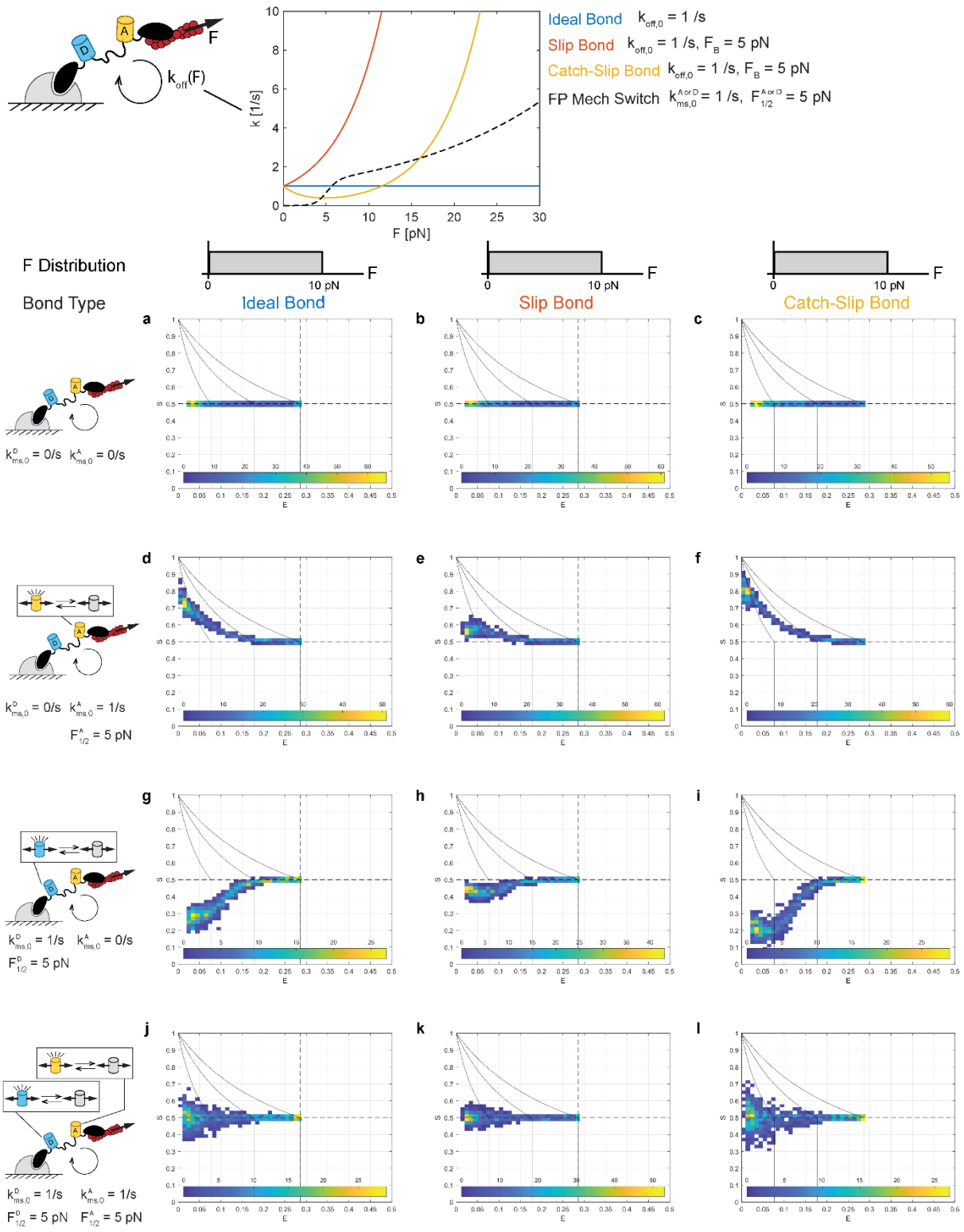

Figure S11, related to Figures 2 and 3. ES-Histograms for Stochastic Simulations with Force-dependent Bonds. (a-c) For no FP mechanical switching [$k_{MS}^{A}(F) = k_{MS}^{D}(F) = 0$], ES-Histogram of 1000 simulated MTS ensembles ($N_{sims} = 1000$), each comprised of 50 total sensors ($n_{sensors} = 50$) subject to single F value drawn from a uniform distribution between 0 and 10 pN and having (a) ideal, (b) slip, or (c) catch-

slip unbinding rate constant. (d-f) Same for acceptor only mechanical switching [$k_{MS}^{A}(F)$ with base parameter values in Table S2 and $k_{MS}^{D}(F) = 0$]. (g-i) Same for acceptor only mechanical switching [$k_{MS}^{D}(F)$ with base parameter values in Table S2 and $k_{MS}^{A}(F) = 0$]. (j-l) Same for acceptor and donor mechanical switching with identical parameters [$k_{MS}^{A}(F)$ and $k_{MS}^{D}(F)$ with base parameter values in Table S2]. The color bars indicate bin counts. In all plots, reference black lines are tension isoclines for acceptor only or donor only mechanical switching at F of 0, 3, and 6 pN (from right-to-left). Note that within single MTS ensembles, all sensors are subject to the same F value.

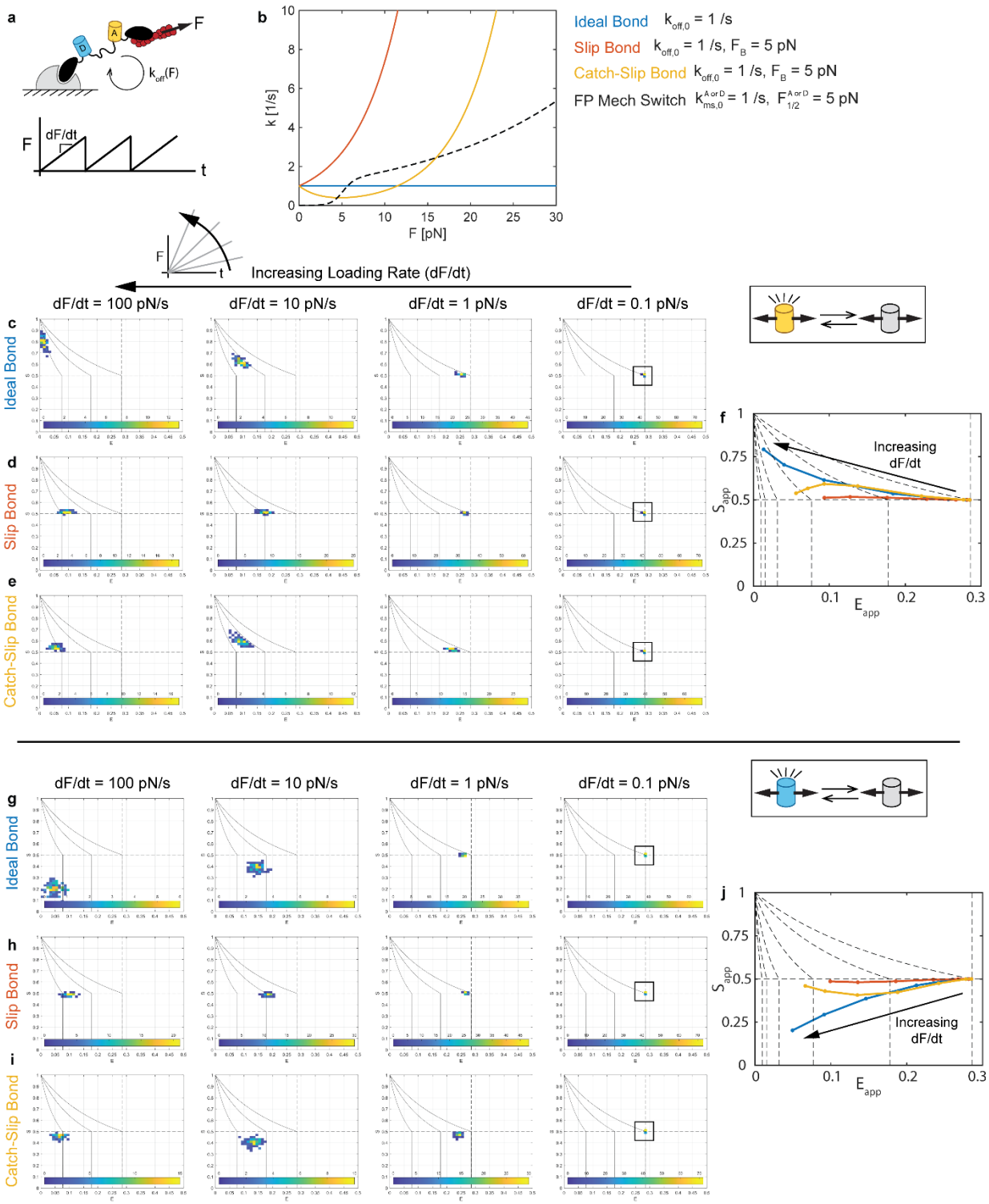

Figure S12, related to Figures 2 and 3. Effect of Loading Rate on FP Mechanical Switching in MTS. (a) Schematic of MTS subject to linear ramp (constant rate) loading. (b) Force-dependent unbinding rate constants for ideal, slip, and catch-slip bond types at indicated parameters (matched intrinsic rate constant and exponential parameters) with the FP mechanical switching rate constant shown for comparison. (c-e) For acceptor only mechanical switching [$k^A_{MS}(F)$ with base parameter values in Table S2 and $k^D_{MS}(F) = 0$] and MTS with an (c) ideal, (d) slip, or (e) catch-slip bond, ES-Histogram of 100

simulated MTS ensembles ($N_{sims} = 100$), each comprised of 50 total sensors ($n_{sensors} = 50$) subject to loading rates 100, 10, 1, or 0.1 pN/s. The color bars indicate bin counts. (f) For acceptor mechanical switching and the three bond types, (E_{app}, S_{app})-curves for a range of loading rate dF/dt from 0.1 to 100 pN/s constructed from the mean values from the stochastic simulations at each loading rate. Reference dots indicate loading rates of 0, 0.32, 1, 3.2, 10, 32, and 100 pN/s (from right-to-left) and reference black dashed lines are tension isoclines for acceptor or donor only mechanical switching at F of 0, 3, 6, 9, 12, and 15 pN (from right-to-left). (g-i) Same as (c-e) but for donor only mechanical switching [$k_{MS}^{D}(F)$ with base parameter values in Table S2 and $k_{MS}^{A}(F) = 0$] and MTS with (g) ideal, (h) slip, or (i) catch-slip bond. (j) Same as (f) but for donor only mechanical switching.

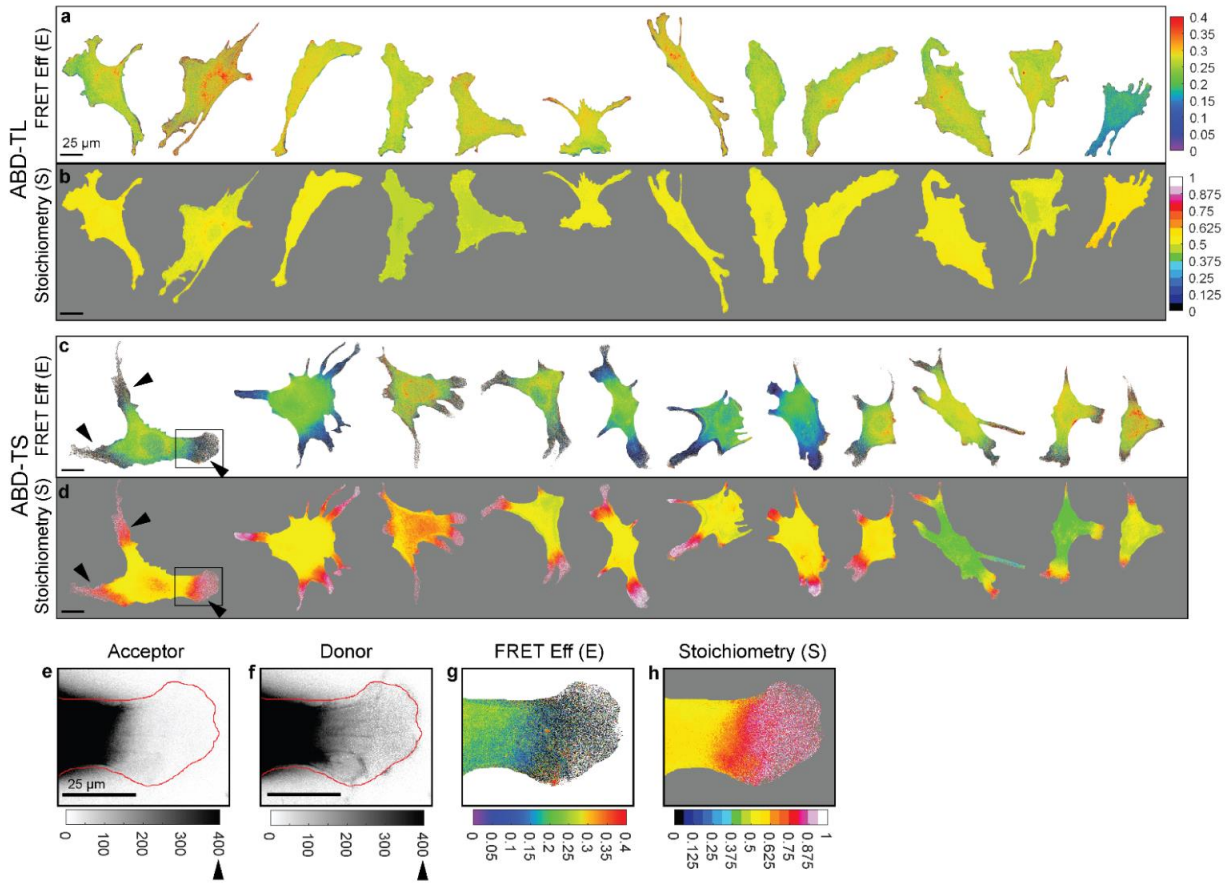

Figure S13, related to Figure 4. Signatures of FP mechanical switching in ABDTS are consistent and exhibit a distinct spatial pattern. Montage of >10 NIH 3T3 cells expressing (a-b) ABDTL or (c-d) ABDTS from a single experimental day, showing FRET efficiency and stoichiometry. (e-h) Zoom of indicated region at periphery of a cell expressing ABDTS, showing acceptor and donor intensities with cell outline overlaid in red and FRET efficiency and Stoichiometry in cell mask.

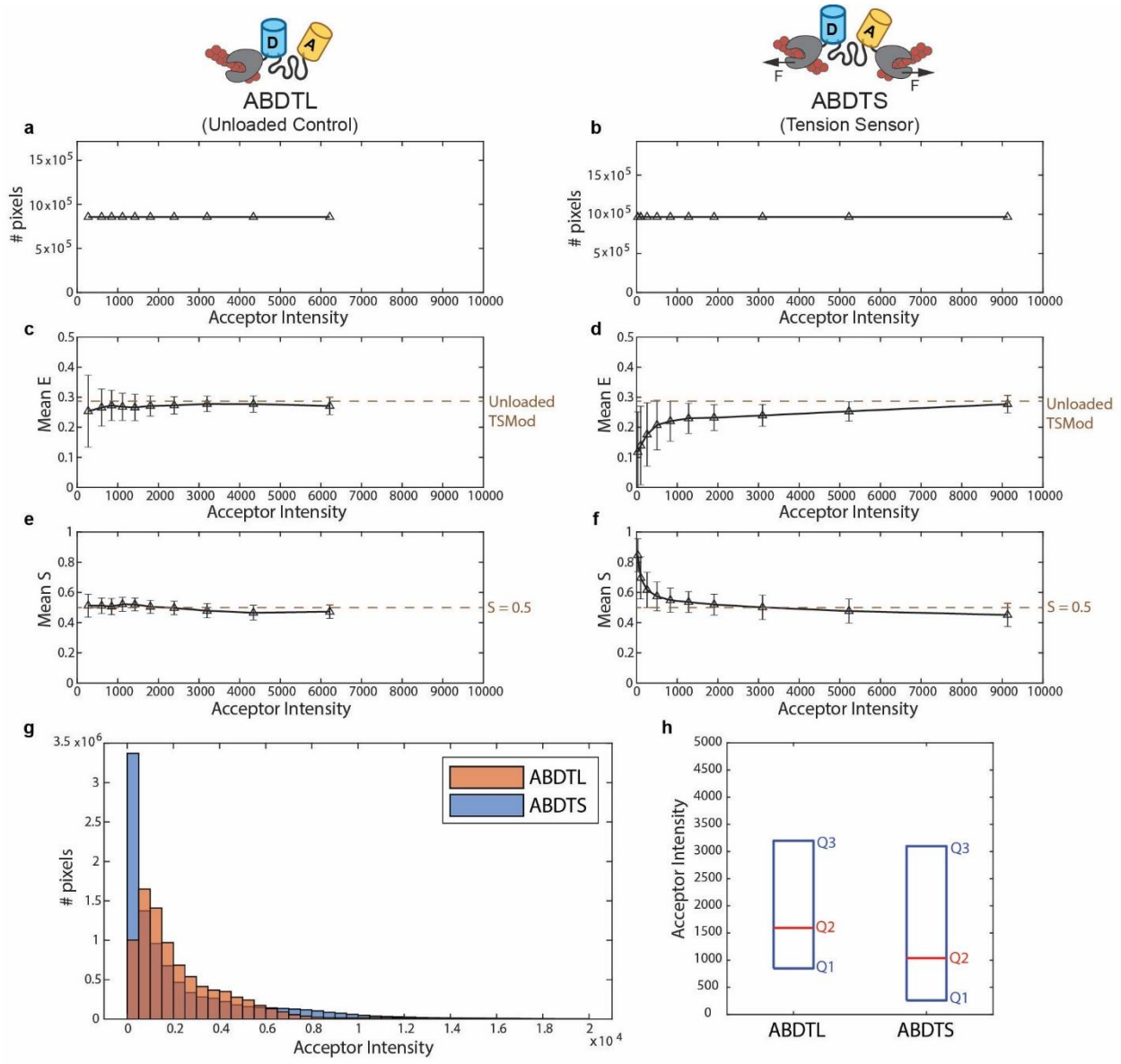

Figure S14, related to Figure 4. Dependence of apparent FRET Efficiency and Stoichiometry on Acceptor Intensity for ABDTL and ABDTS. *Note: Acceptor intensity can only be considered an estimate of sensor concentration when FP mechanical switching is not possible, i.e. only for ABDTL. Acceptor intensity is not a measure of concentration for ABDTS.* Plots of (a-b) number of pixels in bin versus binned acceptor intensity, (c-d) mean +/- standard deviation of E versus binned acceptor intensity, and (e-f) mean +/- standard deviation of S versus binned acceptor intensity for ADBTL (a,c,e) and ABDTS (b,d,f). Binning by acceptor intensity was performed such that there are 10 bins each with the same number of pixels. (g) Histograms of acceptor intensity for ABDTL and ABDTS (using fixed bins of width 500). (h) Box plots of acceptor intensity for ABDTL and ABDTS showing the lower (Q1), middle (Q2), and upper (Q3) quartiles. The data shown in this figure corresponds to the entire data set from Figure 4 (38/44 cells for ABDTL/ABDTS over 5 experimental days).

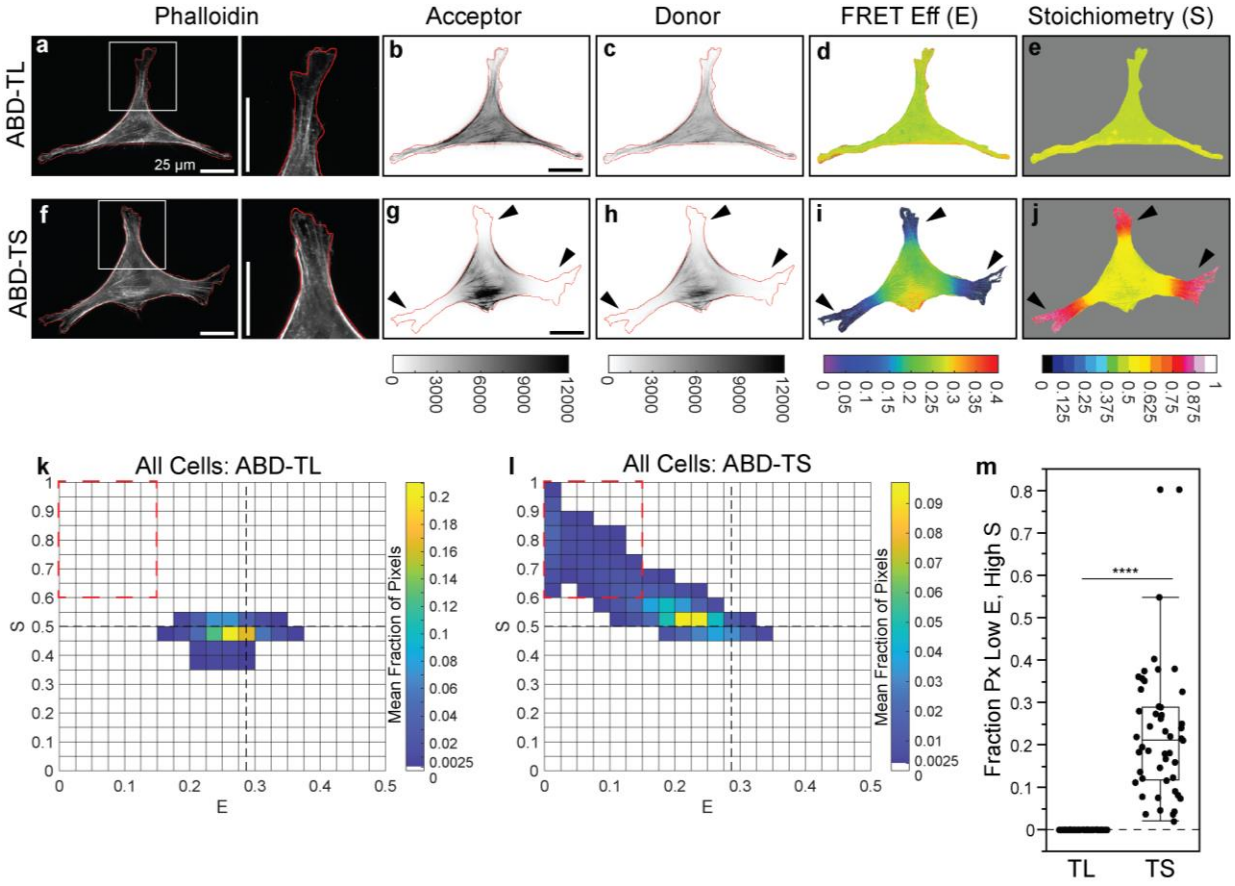

Figure S15, related to Figure 4. Fixation and phalloidin labeling of F-actin in ABDTL- and ABDTS-expressing cells. Representative NIH 3T3 cells expressing ABDTL (a-e) or ABDTS (f-j) fixed and labeled with phalloidin. Images are phalloidin intensity used to create cell outline, acceptor and donor intensities with cell outline overlaid in red, and FRET efficiency and Stoichiometry in cell mask. ES-histograms for whole cell populations of ABDTL (k) or ABDTS (l) (N = 64/48 cells for ABDTL/ABDTS over 2 experimental days), where color bars indicate the cell-averaged fraction of pixels in each bin. (m) Box plot of fraction of pixels in each cell in the low E, high S bin ($E < 0.15,\ S > 0.60$). Differences between groups were detected using the Steel-Dwass test, ****: p<0.0001.

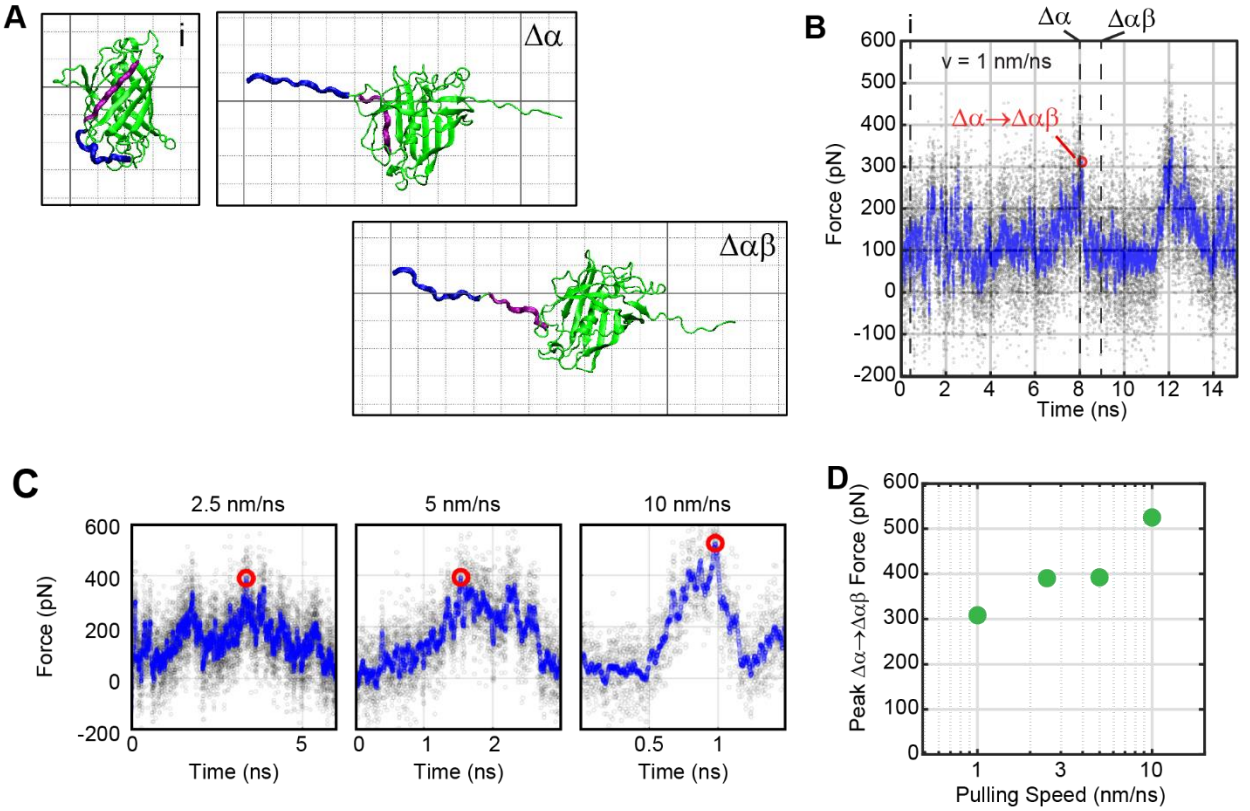

Figure S16, related to Figure 4. Steered molecular dynamics simulations of alpha-GFP. (A) Three snapshots of a representative simulation of GFP unfolding (at a pulling speed of 1 nm/ns) are shown: The initial state just before the application of force (i), the first intermediate state wherein GFP's N-terminal handle (blue) has been removed from the structure (Δα), and what we believe to be the mechanically switched intermediate wherein a β-strand (purple) has been removed from GFP's β-barrel structure (Δαβ). (B) A force vs. time plot from the simulation in (A) showing the force-extension curve (black translucent circles) and the force-extension curve smoothed by 250 points (blue circles). Vertical dashed lines show the timepoints of the snapshots in (A). A red circle shows the maximum force, which coincides with the transition from the Δα state to the Δαβ state. (C) Force-extension curves for additional loading rates, with the peak force before the Δα to Δαβ transition shown with red circles. (D) The peak force before the Δα to Δαβ transition, shown as a function of the pulling speed. Each point represents the maximum from a single simulation.

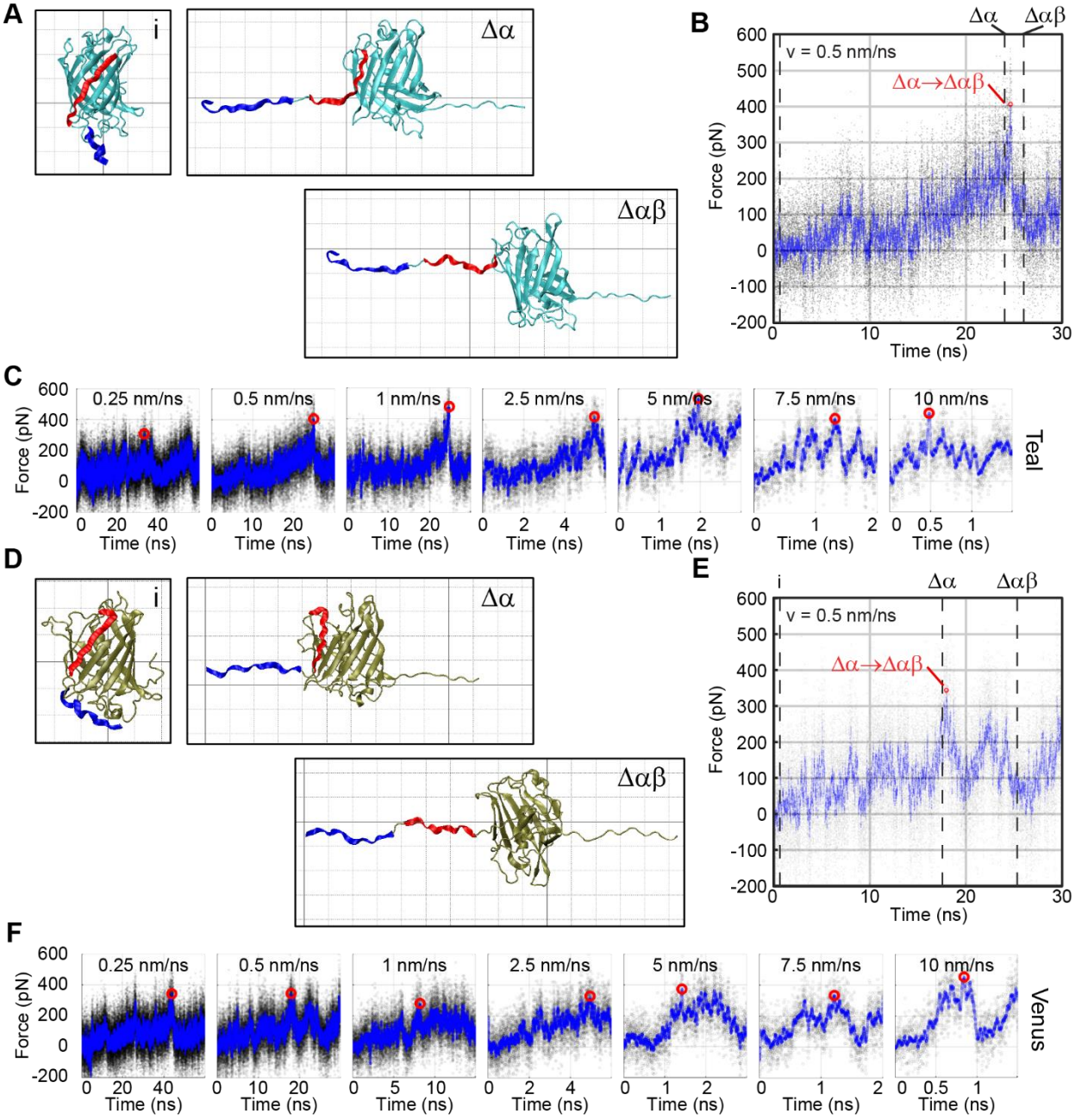

Figure S17, related to Figure 4. Steered molecular dynamics simulations of mTFP1 and mVenus. (A-C) Like Figure S16A-C, but for simulations of mTFP1. (D-F) Like Figure S16A-C, but for simulations of mVenus.

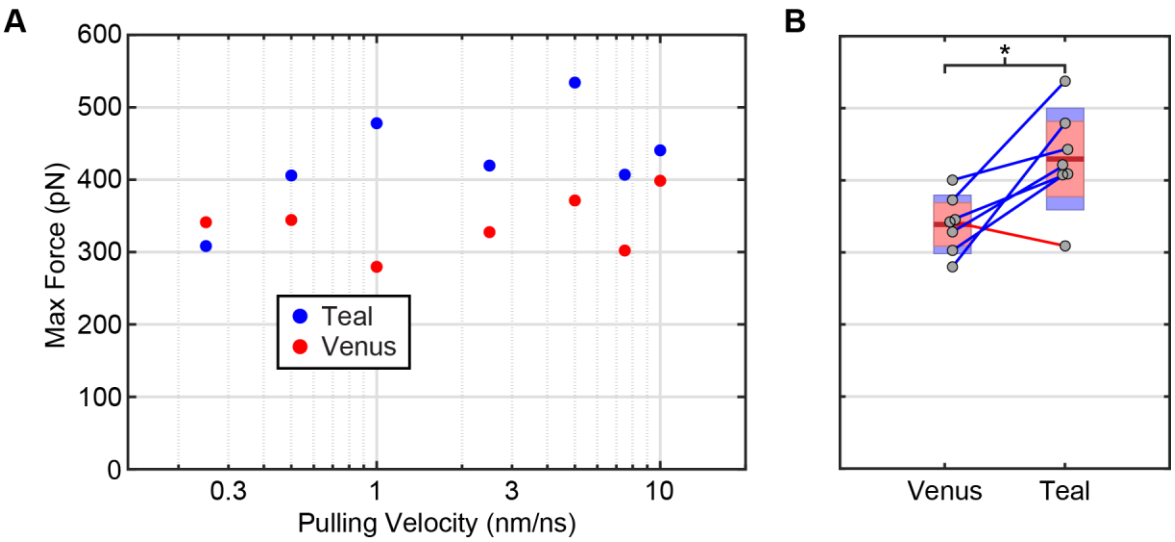

Figure S18, related to Figure 4. Comparison of peak forces from SMD simulations for mVenus and mTFP1. (A) The peak force before the Δα to Δαβ transition, shown as a function of the pulling speed for simulations of mTFP1 (blue) and mVenus (red) from Figure S17. B) Boxplots showing the maximum forces from (A) pooled for a paired comparison between mVenus and mTFP1. Boxplots are shown with average (maroon line), standard error of the mean (pink), and 95% confidence intervals (purple), as well as all individual datapoints (gray circles). Pairings between datapoints are shown via lines, where blue line color denotes that the maximum force for mTFP1 is higher than that of mVenus and red line color denotes the reverse. A statistical comparison between the two groups (paired T-test) shows that mTFP1 has a significantly higher rupture force than mVenus (p = 0.047). These findings are consistent with our experimental observations.

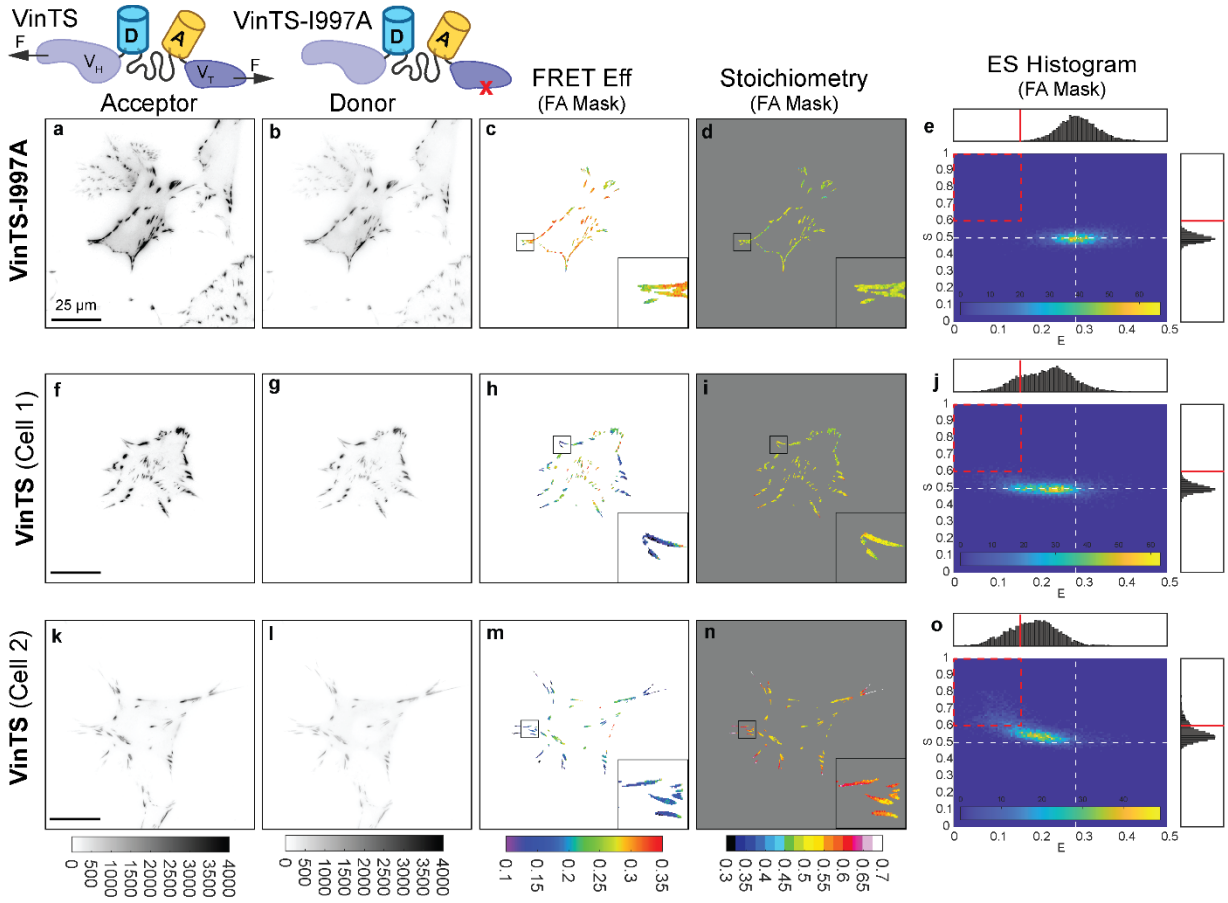

Figure S19, related to Figure 6. Signatures of weaker, but detectable, FP mechanical switching in VinTS. Representative vinculin -/- MEFs expressing VinTS-I997A (a-e) or VinTS (f-o) on FN-coated glass, showing images of acceptor intensity, donor intensity, FRET efficiency in the FA mask, Stoichiometry in the FA mask, and an ES-histogram of FA-masked pixels for the cell, where color bars indicate pixel counts. For VinTS, the two representative cells correspond to the two ends of the spectrum of behaviors observed. Cell 1 (f-j) matches model predications for MTS loading without FP mechanical switching. Cell 2 (k-o) matches model predications for MTS loading with acceptor mechanical switching. The data is a re-analysis of three-channel FRET images from an experiment in a previous publication [S3].

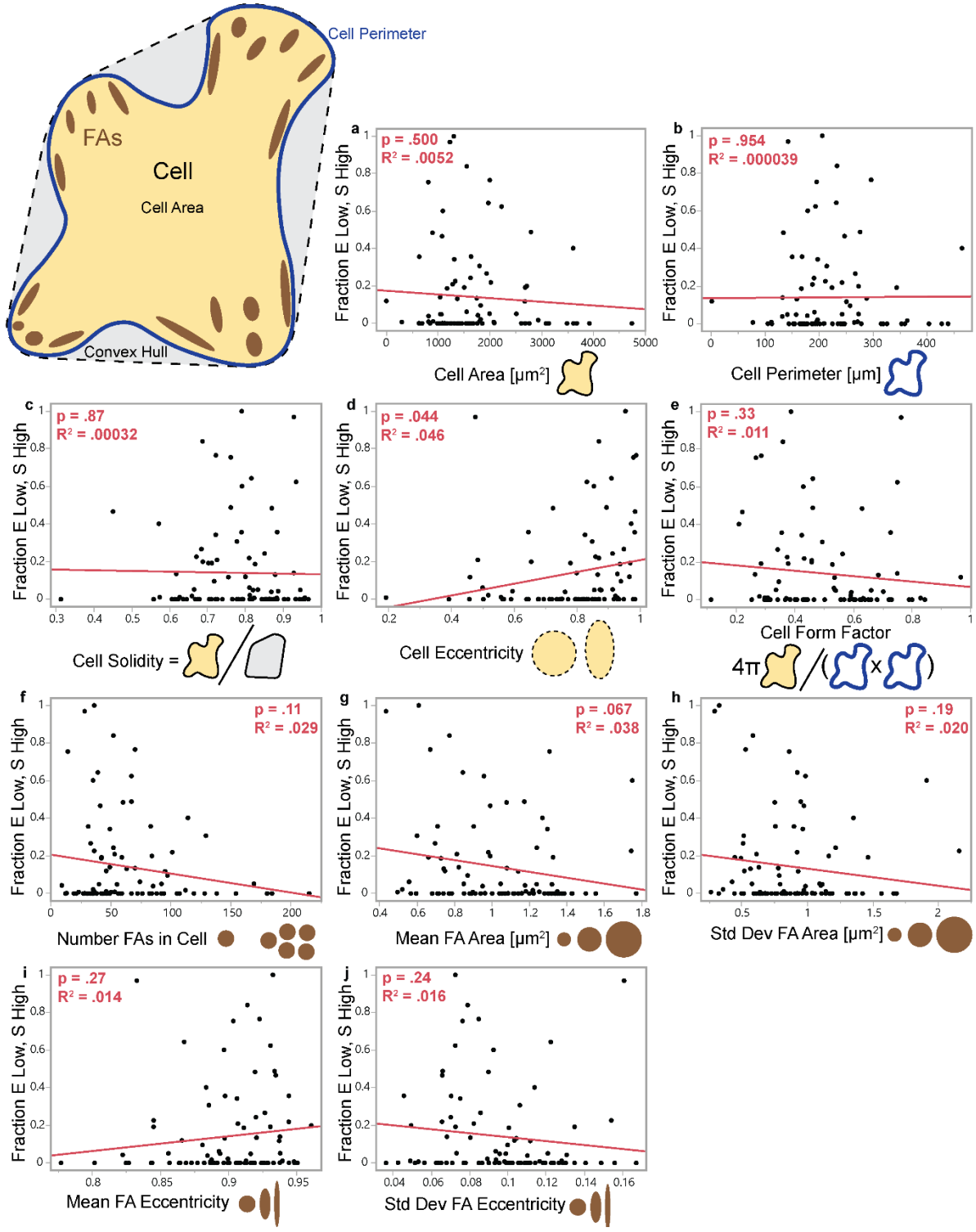

Figure S20, related to Figure 6. Relationships between Acceptor Mechanical Switching in VinTS and Cellular and Focal Adhesion Morphology Metrics. Scatter plots of the fraction of pixels in each cell in the low E, high S bin ($E < 0.15,\ S > 0.60$) versus (a) cell area, (b) cell perimeter, (c) cell solidity, (d) cell eccentricity, (e) cell form factor, (f) number of FAs in cell, (g) mean FA area, (h) standard deviation of FA area, (i) mean FA eccentricity, or (j) standard deviation of FA eccentricity. For all plots, the fitted line, the

p value for the F statistic, and the R squared value are shown for the linear regression. A significance level of 0.005 (=0.05/10) was used to account for the 10 tests performed. No p values were considered significant at this level. Each plot contains the entire VinTS-WT data set from Figure 6.

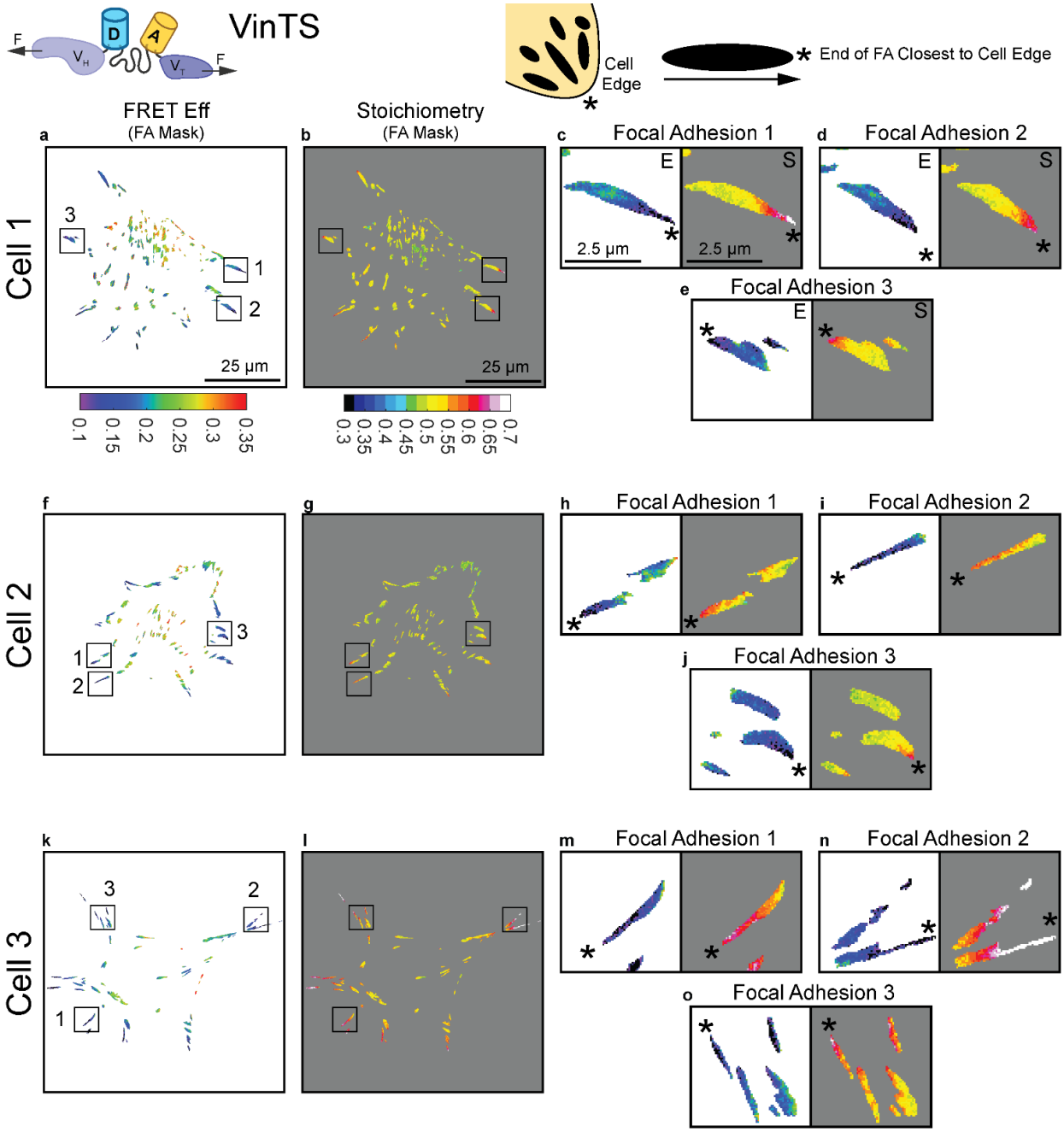

Figure S21, related to Figure 6. Single FA Gradients in VinTS FRET Efficiency (lowest at cell edge) are Accompanied by Gradients in Stoichiometry (highest at cell edge). (a) FRET Efficiency and (b) Stoichiometry images for a representative Vinculin -/- MEF expressing VinTS. (c-e) Zoom-in FRET Efficiency and Stoichiometry images for three indicated FA regions, with asterik indicated the end of the FA that is closest to the cell edge. (f-j) and (k-o) are analogous image sets for two additional representative cells.

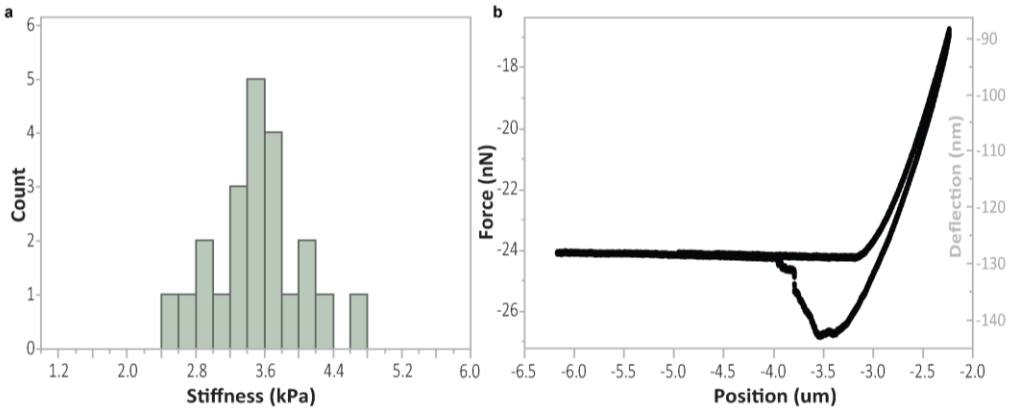

Figure S22, related to Figure 7. Mechanical testing of the PA gel. (a) Histogram of Young's modulus estimates for the PA gel formulation used in the experiment in Figure 7. Young's modulus was determined via Hertzian model fit from mechanical tests by atomic force microscopy (AFM). (b) Representative trace from mechanical testing. See methods for more information on mechanical testing.

Note S1: Mathematical Models of FP Mechanical Switching in Load-bearing Proteins and FRET-based Molecular Tension Sensors, related to Figures 1-3 and S1-S12

I. Introduction

This supplemental note covers the formulation, results, and analysis of mathematical models of fluorescent protein (FP) mechanical switching in load-bearing proteins and Förster resonance energy transfer (FRET)-based molecular tension sensors (MTS). To investigate the process of FP mechanical switching in the context of protein loading in cells, we first modeled the reversible mechanical switching of a single FP integrated into a load-bearing protein and assessed the extent of FP mechanical switching across load magnitudes and durations estimated for protein loading in cells (Section II). Then, to assess how FP mechanical switching affects FRET-based MTSs, we extended the model of FP mechanical switching to an MTS containing a donor and an acceptor FP (Section III). Using simulated three channel FRET measurements analogous to experimentally accessible readouts, we developed and applied a framework for detecting FP mechanical switching in MTSs. To facilitate data visualization, we conducted simulations that account for phenomena expected in real experimental data, including variability in protein loading dynamics and intrinsic noise in FP mechanical switching (Section IV). Lastly, the effect of two additional aspects of protein loading dynamics, force-sensitive bonds and loading rate control, on FP mechanical switching in MTSs was assessed (Section V). Assumptions and limitations of the models are discussed in Section VI, interpretation of experimental data is covered in Section VII, and the main conclusions are summarized in Section VIII.

II. Model of FP Mechanical Switching in a Load-bearing Protein

In this section, we investigate the process of FP mechanical switching in the context of load-bearing proteins inside cells. To do so, we develop and use a model describing the reversible mechanical switching of an FP integrated into a load-bearing protein subject to protein loading dynamics.

A. Model Formulation

1. Kinetic Model

Mechanical forces applied externally to cells or generated internally by cells are transmitted through proteins that form mechanical linkages within the cytoskeleton or between the cytoskeleton and other subcellular structures, including adhesions and the plasma membrane [S4, S5, S6, S7]. Proteins in these linkages bear dynamic loads, exhibit binding/unbinding dynamics, and turnover [S4, S5, S6, S7]. Therefore, we modeled an FP integrated into a load-bearing protein subject to dynamic loading parameterized by a load magnitude F and a characteristic load duration τ, which is governed by unbinding from a loading source with rate constant k_{unbind} (where $\tau \equiv 1/k_{unbind}$) (Figure S1a).

Our model of FP mechanical switching is motivated by single molecule experiments demonstrating that GFP fluorescence can be reversibly switched on/off by repeated cycles of mechanical tension [S8]. Inside the load-bearing protein, we estimate the behavior of the FP as a two-state system, with fluorescence on (FP1) or off (FP0). The FP experiences the force F across the load-bearing protein and can undergo a mechanical switching transition (FP1 → FP0) according to a force-dependent mechanical switching rate constant, $k_{MS}(F)$. When the load-bearing protein unbinds from the loading source with rate constant k_{unbind}, an FP in the off state immediately recovers (FP0 → FP1) before the load-bearing protein rebinds

and is reloaded. This is consistent with the rapid recovery of unloaded FPs and/or the exchange of load-bearing proteins with a cytosolic pool upon unbinding [S8, S9].

As we intended to interpret experiments with different types of FPs, we modeled a generalized force-dependent mechanical switching rate constant, $k_{MS}(F)$, that was informed from single molecule experimental observations of the response of GFP structure and fluorescence to mechanical loading [S8, S10]. Briefly, when GFP is mechanically loaded, it undergoes a fast, near-equilibrium transition from the native state to the first intermediate state that occurs at a characteristic force magnitude [S10]. This first intermediate is characterized by the unfurling of GFP's flexible handle region, while all the beta strands in the beta-barrel remain fully intact. From this first intermediate state, GFP can transition to a second intermediate state, corresponding to beta-barrel disruption without complete denaturation [S8]. A force-dependent rate constant was previously determined for this second transition by fitting to a Bell model [S8]. Lastly, recovery of fluorescence requires complete unloading of GFP and return to the native state, with no recovery of fluorescence observed in the intermediate states along the refolding trajectory [S8]. Taken together, this suggests that FP mechanical switching occurs through two subsequent transitions: a fast, near-equilibrium transition at a characteristic force, followed by a slower transition with a rate constant characterized by a Bell model. As recovery of fluorescence required complete unloading, we chose to model the second transition as not reversible and only permit recovery of fluorescence through protein unbinding and unloading (see above). Under these assumptions, we can approximate a single effective forward rate constant for FP mechanical switching. This consists of the probability of existing in the intermediate state produced from the first near-equilibrium sub-transition (modeled as a logistic function) multiplied by the rate constant of the second sub-transition (modeled as a Bell model). As such, we define the force-dependent rate constant of mechanical switching for an FP subject to a tension, F, as follows:

$$k_{MS}(F) = \left[1 + e^{-m\cdot(F-F_{1/2})}\right]^{-1} \cdot \left[k_{MS,0} \cdot e^{F\cdot\Delta x_{MS}/(k_BT)}\right] \quad \text{(S1)}$$

where the logistic function component is parameterized by a characteristic force $F_{1/2}$ and a steepness m, and the Bell model component is parametrized by an intrinsic rate constant $k_{MS,0}$ and an exponential parameter Δx_{MS} (Figure S1b). For the logistic component motivated by the fast, near-equilibrium sub-transition, if we consider a system with two states (A and B) with a difference in free energy minima ΔG^0_{BA} and a mechanical reaction coordinate separation Δx^0_{BA} that is assumed unaffected by applied force, then the equilibrium probability of existing in state B as function of F is $P_{B,eq}(F) = \left[1 + e^{(\Delta G^0_{BA} - F\Delta x^0_{BA})/(k_BT)}\right]^{-1}$, derived from Bustamante et al. [S11]. In this case, we have $F_{1/2} = \frac{\Delta G^0_{BA}}{\Delta x^0_{BA}}$ and $m = \frac{\Delta x^0_{BA}}{k_BT}$. Using state A to represent native GFP and state B to represent the first unfolding intermediate of GFP (GFPΔα), ΔG^0_{BA} would be approximately $22k_BT$ as previously reported [S10]. If we also estimate Δx^0_{BA} from the previously reported contour length increase for this transition ($3.2\ nm$) [S10], we get $F_{1/2} = 28.3\ pN$ and $m = 0.778\ pN^{-1}$ for GFP. The parameters for the single FP model are given in Table S1.

Table S1. Parameters for Single FP Model, related to Figure S1.

Param	Units	GFP Estimate	Single FP Model	Rationale
$F_{1/2}$	pN	28.3	[2.83, 283] sweep	Sweep centered on estimated parameter for GFP from data in Dietz et al [S10].
m	1/pN	0.778	0.778	Estimated parameter for GFP from data in Dietz et al [S10].
$k_{MS,0}$	1/s	0.33	[0.033, 3.3] sweep	Sweep centered on estimated parameter for GFP from Ganim et al [S8].
Δx_{MS}	nm	0.23	0.23	Estimated parameter for GFP from Ganim et al [S8].
F	pN	N/A	[0,40] sweep	Encompasses estimated range of load magnitudes (~1-20 pN) based on molecular-scale force generation in the actin cytoskeleton driven by Myosin II motors [S12, S13] or F-actin polymerization [S14], as well as estimates for the extension of molecular clutches (with characteristic protein stiffnesses) by actin retrograde flow [S5, S15] (Figure S1c, x-axis). Full range of parameter sweep extends to load magnitudes twice as high for completeness.
τ	s	N/A	[.01,100] sweep	Encompasses estimated range of load durations (~0.1-10 seconds) based on the unbinding lifetimes of bonds in mechanical linker proteins and transmembrane proteins under this range of load magnitudes, including alpha-catenin:F-actin [S16], vinculin:F-actin [S17], talin:F-actin [S18], Integrin:FN [S19], E-cad trans-dimer [S20], alpha-actinin:F-actin [S21] and filamin:F-actin [S21] (Figure S1c, y-axis). Full range of parameter sweep extends below and above estimated range by 1 order of magnitude for completeness.

2. Steady State Analysis of Model

To characterize the kinetic model for FP mechanical switching in a load-bearing protein, a steady state analysis in the deterministic limit was performed using 2 ordinary differential equations describing the rate of change of concentration of each species and 1 conservation equation for total concentration of protein.

$$\frac{d[FP1]}{dt} = -k_{MS}(F) \cdot [FP1] + k_{unbind}(F) \cdot [FP0]$$

$$\frac{d[FP0]}{dt} = -k_{unbind}(F) \cdot [FP0] + k_{MS}(F) \cdot [FP1]$$

$$[Total\ FP] = [FP1] + [FP0]$$

Setting each ODE to zero and solving for the steady state concentrations of each species yields expressions for the steady state fraction (ρ) of each species:

$$\rho_{FP1}(F) = \frac{[FP1]_{ss}}{[FP1]_{ss} + [FP0]_{ss}} = \frac{k_{unbind}}{k_{unbind} + k_{MS}(F)} \quad \text{(S2)}$$

$$\rho_{FP0}(F) = \frac{[FP0]_{ss}}{[FP1]_{ss} + [FP0]_{ss}} = \frac{k_{MS}(F)}{k_{unbind} + k_{MS}(F)} \quad \text{(S3)}$$

B. Results

To characterize the process of FP mechanical switching inside a dynamic load-bearing protein, we first investigated the range of load magnitudes (F) and durations (τ) over which FP mechanical switching is likely to occur. We focused on an estimated range of load magnitudes (~1-20 pN) based on molecular-scale force generation in the actin cytoskeleton driven by Myosin II motors [S12, S13] or F-actin polymerization [S14], as well as estimates for the extension of molecular clutches (with characteristic protein stiffnesses) by actin retrograde flow [S5, S15] (Figure S1c, x-axis). We also note that this range encompasses the equilibrium unfolding forces of multiple endogenous mechanosensitive protein domains, including those in alpha-catenin and talin [S22, S23]. We focused on an estimated range of load durations (~0.1-10 seconds) based on the unbinding lifetimes of bonds in mechanical linker proteins and transmembrane proteins under this range of load magnitudes, including alpha-catenin:F-actin [S16], vinculin:F-actin [S17], talin:F-actin [S18], integrin:FN [S19], E-cadheren trans-dimer [S20], alpha-actinin:F-actin [S21] and filamin:F-actin [S21] (Figure S1c, y-axis). As a large set of natural and engineered FPs with different structures, photophysical properties, and mechanical stabilities exist, and the integration of FPs into a fusion protein as well as the use of FPs in the cellular environment can alter these properties [S2, S10, S24, S25], we assessed FPs with a range of force thresholds ($F_{1/2}$) and kinetic timescales ($1/k_{ms,0}$) (Figure S1d-o).

For a given set of FP parameters, FP mechanical switching occurs at load magnitudes near or above the force threshold for FP mechanical switching ($F \geq F_{1/2}$) and load durations of the same order of magnitude or longer than the kinetic timescale for FP mechanical switching ($\tau \geq 1/k_{ms,0}$) (for example see Figure S1h). If the load magnitude is too low, then FP mechanical switching is not permitted regardless of load duration. Likewise, when the load duration is too short, the protein unbinds before FP mechanical switching occurs, regardless of load magnitude.

Comparing FPs with different parameters, we find that decreasing the force threshold ($F_{1/2}$) expands the range of forces over which FP mechanical switching occurs with little effect on the range of load durations (for example compare Figure S1e,h,k,n). Alternatively, increasing the kinetic rate constant ($k_{ms,0}$) expands the range of load durations that support FP mechanical switching without affecting the load magnitude range (for example compare Figure S1g-i). Therefore, for two FPs with different sets of FP mechanical switching parameters, there exists load magnitudes and/or durations for which neither, just one, or both FPs are mechanically switched.

Lastly, this model also demonstrates differential sensitivity of FP mechanical switching to load magnitude and duration. For a given set of FP parameters, the fraction of mechanically switched FPs changes rapidly

with respect to force near the force threshold, increasing steeply from 0 to 1 over a small range of a few pN in load magnitude (less than an order of magnitude; exact value depends on the parameters m and Δx_{MS}; for an example see the horizontal arrow in Figure S1h). In contrast, the fraction of mechanically switched FPs changes gradually with respect to load duration, increasing gradually from 0 to 1 over almost 2 orders of magnitude in load duration (for an example see the vertical arrow in Figure S1h).

Taken together, the model of FP mechanical switching in a load-bearing protein indicates that FP mechanical switching can occur at the load magnitudes and durations estimated for protein loading in cells for a range of FP parameters. For a given FP, the loads must be high enough ($F \geq F_{1/2}$) and long enough ($\tau \geq 1/k_{ms,0}$) to support mechanical switching. Lastly, the process of FP mechanical switching exhibits sensitivity to both load magnitude and duration.

III. Model of FP Mechanical Switching in FRET-based Tension Sensor

In this section we investigate how FP mechanical switching affects FRET-based MTSs. To do so, we extend the model of FP mechanical switching in a load-bearing protein to a FRET-based MTS containing a donor and an acceptor FP. Then, we compute three channel FRET measurements of ensembles of MTSs exhibiting donor and/or acceptor mechanical switching.

A. Model Formulation

1. Kinetic Model

An MTS consists of a tension sensor module composed of two FPs (donor and acceptor) separated by an extensible domain that is integrated into a load-bearing protein. The MTS is subject to the same loading dynamics previously described for load-bearing proteins in Section II.A (Figure S2a). As the FPs are in series in the line of loading, the load applied across the MTS is experienced by both the donor and acceptor FPs, each of which can undergo FP mechanical switching as previously described in Section II.A. As a large set of natural and engineered FPs with different structures, photophysical properties, and mechanical stabilities exist [S10, S24], we model separate FP mechanical switching kinetic parameters for the acceptor and donor. The force-dependent rate constant of mechanical switching for donor and acceptor FPs subject to a load, F, are thus defined as follows:

$$k_{MS}^{D}(F) = \left[1 + e^{-m^{D}\cdot(F - F_{1/2}^{D})}\right]^{-1} \cdot \left[k_{MS,0}^{D} \cdot e^{F\cdot\Delta x_{MS}^{D}/(k_B T)}\right] \quad \text{(S4)}$$

$$k_{MS}^{A}(F) = \left[1 + e^{-m^{A}\cdot(F - F_{1/2}^{A})}\right]^{-1} \cdot \left[k_{MS,0}^{A} \cdot e^{F\cdot\Delta x_{MS}^{A}/(k_B T)}\right] \quad \text{(S5)}$$

Because the donor and acceptor FP can each exist in two states, i.e. functional/on (FP1) and non-functional/off (FP0), an MTS can exist in one of four states: functional donor and functional acceptor (D1A1), functional donor and non-functional acceptor (D1A0), non-functional donor and functional acceptor (D0A1), and non-functional donor and non-functional acceptor (D0A0). The transitions between these four states are summarized in the transition rate diagram (Figure S2b). Note that the absence of reverse transitions from D0A0 to D1A0 or from D0A0 to D0A1 is a consequence of the simple assumption that FP fluorescence does not recover under load. The parameters for the MTS model are given in Table S2. Values of m^D and m^A were adjusted based on the values of $F_{1/2}^{D}$ and $F_{1/2}^{A}$, respectively, to match the experimental observation of negligeable FP mechanical switching in unloaded

FPs [S8] as well as MTSs (see the following load-insensitive experimental controls from this work: ABDTL in Figure 4 and Figure S13, and VinTS-I997A in Figure 6 and Figure S19). Specifically, m^D and m^A were set to limit the fraction of mechanically switched FPs in unloaded MTSs to negligeable values of $\rho_{D0}(F=0) < 0.0005$ and $\rho_{A0}(F=0) < 0.0005$ without reducing m^D and m^A below a lower limit of $1\ pN^{-1}$ based on the estimated parameter for GFP [S10] (see Section II.A). Mathematically, this means that $m = max\left\{1,\ \frac{1}{F_{1/2}}\ln\left(\frac{1}{.0005}-1\right)\right\}\ pN^{-1}$.

Table S2. Parameters for MTS Model, related to Figures 2-3 and S5-S12.

Param	Units	Base Value	Param Sweep	Rationale
$F_{1/2}^D$ $F_{1/2}^A$	pN	5	1, 3, 5, 8, 25	Base value is permissive of FP mechanical switching in the estimated range of load magnitudes for molecular-scale forces. Sweep covers range below and above base value, with highest value similar to estimated parameter for GFP from Dietz et al. [S10] (see Table S1)
m^D m^A	1/pN	1.5	7.6, 2.5, 1.5, 1, 1 for $F_{1/2}$ values of 1, 3, 5, 8, 25, respectively	Adjusted to match the experimental observation of negligeable FP mechanical switching in unloaded MTSs. See text for further information.
$k_{MS,0}^D$ $k_{MS,0}^A$	1/s	1	[.1,10]	Base value similar to parameter for GFP from Ganim et al. [S10] (see Table S1). Sweep covers one order of magnitude around the base value.
Δx_{MS}^D Δx_{MS}^A	nm	.23	.23	Parameter for GFP from Ganim et al. [S8] (see Table S1)
F	pN	N/A	[0,30]	Encompasses estimated range of load magnitudes (~1-20 pN) based on molecular-scale force generation in the actin cytoskeleton driven by Myosin II motors [S12, S13] or F-actin polymerization [S14], as well as estimates for the extension of molecular clutches (with characteristic protein stiffnesses) by actin retrograde flow [S5, S15] (Figure S1c, x-axis). Full range of parameter sweep extends to load magnitudes 1.5x as high for completeness.
τ	s	1	[.01,100]	Encompasses estimated range of load durations (~0.1-10 seconds) based on the unbinding lifetimes of bonds in mechanical linker proteins and transmembrane proteins under this range of load magnitudes, including alpha-Catenin:F-actin [S16], Vinculin:F-actin [S17], Talin:F-actin [S18], Integrin:FN [S19], E-cad trans-dimer [S20], alpha-Actinin:F-actin [S21] and Filamin:F-actin [S21] (Figure S1c, y-axis). Full range of parameter sweep extends below and above estimated range by 1 order of magnitude for completeness.

2. Steady State Analysis of Kinetic Model

To characterize the kinetic model for FP mechanical switching in an MTS, a steady state analysis in the continuous deterministic limit was performed using 4 ordinary differential equations describing the rate of change of concentration of each species and 1 conservation equation for total concentration of MTS.

$$\frac{d[D1A1]}{dt} = -\left(k_{MS}^{D}(F) + k_{MS}^{A}(F)\right) \cdot [D1A1] + k_{unbind} \cdot ([D0A1] + [D0A1] + [D0A0])$$

$$\frac{d[D0A1]}{dt} = -(k_{MS}^{A}(F) + k_{unbind}) \cdot [D0A1] + k_{MS}^{D}(F) \cdot [D1A1]$$

$$\frac{d[D1A0]}{dt} = -(k_{MS}^{D}(F) + k_{unbind}) \cdot [D1A0] + k_{MS}^{A}(F) \cdot [D1A1]$$

$$\frac{d[D0A0]}{dt} = -(k_{unbind}) \cdot [D0A0] + k_{MS}^{A}(F) \cdot [D0A1] + k_{MS}^{D}(F) \cdot [D1A0]$$

$$[Total\ MTS] = [D1A1] + [D0A1] + [D1A0] + [D0A0]$$

Setting each ODE to zero and solving for the steady state concentrations of each species yields expressions for the steady state fraction (ρ) of each species:

$$\rho_{D1A1}(F) = \frac{[D1A1]_{ss}}{[Total\ MTS]} = \frac{k_{unbind}}{k_{MS}^{D}(F) + k_{MS}^{A}(F) + k_{unbind}} \tag{S6}$$

$$\rho_{D0A1}(F) = \frac{[D0A1]_{ss}}{[Total\ MTS]} = \frac{k_{MS}^{D}(F) \cdot k_{unbind}}{[k_{MS}^{A}(F) + k_{unbind}][k_{MS}^{D}(F) + k_{MS}^{A}(F) + k_{unbind}]} \tag{S7}$$

$$\rho_{D1A0}(F) = \frac{[D1A0]_{ss}}{[Total\ MTS]} = \frac{k_{MS}^{A}(F) \cdot k_{unbind}}{[k_{MS}^{D}(F) + k_{unbind}][k_{MS}^{D}(F) + k_{MS}^{A}(F) + k_{unbind}]} \tag{S8}$$

$$\rho_{D0A0}(F) = \frac{[D0A0]_{ss}}{[Total\ MTS]} = \frac{k_{MS}^{D}(F) \cdot k_{MS}^{A}(F) \cdot (k_{MS}^{D}(F) + k_{MS}^{A}(F) + 2k_{unbind})}{[k_{MS}^{A}(F) + k_{unbind}][k_{MS}^{D}(F) + k_{unbind}][k_{MS}^{D}(F) + k_{MS}^{A}(F) + k_{unbind}]} \tag{S9}$$

Additionally, the total steady state fraction of MTSs with mechanically switched donor or acceptor can also be obtained:

$$\rho_{D0}(F) = \frac{[D0A1]_{ss} + [D0A0]_{ss}}{[Total\ MTS]} = \frac{k_{MS}^{D}(F)}{k_{MS}^{D}(F) + k_{unbind}} \tag{S10}$$

$$\rho_{A0}(F) = \frac{[D1A0]_{ss} + [D0A0]_{ss}}{[Total\ MTS]} = \frac{k_{MS}^{A}(F)}{k_{MS}^{A}(F) + k_{unbind}} \tag{S11}$$

3. Computation of Three Channel FRET Measurements of MTS Ensemble

We focused on sensitized emission as the FRET imaging modality because it is widely used and there are existing approaches for calibrating, measuring, and analyzing the relative abundance of acceptor and donor fluorophores [S26, S27, S28]. In sensitized emission-based FRET measurements, images are

acquired in three channels (AA: acceptor excitation and acceptor emission; DD: donor excitation and donor emission; DA: donor excitation and acceptor emission) [S29]. With calibration, the FRET efficiency, E, and FP stoichiometry, $S = n_D/(n_D + n_A)$, can be determined from the signal in these three channels [S28]. To simulate measurements of MTSs with FP mechanical switching, we derive general expressions for the three channel FRET signals and resulting apparent FRET Efficiency, E_{app}, and Stoichiometry, S_{app}, for a population of MTSs. In a given population, each MTS exists in a state, ψ_i, based on the functional status of its donor and acceptor fluorescent protein ($\psi_i = \mathrm{D1A1}, \mathrm{D1A0}, \mathrm{D0A1}, \mathrm{D0A0}$) and is subject to a force, F_i.

Signal Contributions for Each Sensor State. Sensors in the D1A1 state ($\psi_i = D1A1$) undergo intramolecular FRET with a FRET efficiency (E_i), which depends on molecular tension according to the FRET Eff vs force calibration of the tension sensor module [S1, S2], i.e. $E_i = f(F_i)$. Here, the FRET-force relationship for the original TSMod (mTFP1-(GPGGA)$_8$-mVenus; Figure S2c) was used to facilitate comparisons to experimental data in this work [S1, S2]. However, the framework here can be adapted to other calibrated tension sensor modules by modifying the FRET-force relationship (see Section VI for a complete discussion of this applicability). To our knowledge, forced-induced changes in the excitation or emission wavelengths of FPs have not been described. Therefore, to determine the signal contribution for each sensor state, we assumed that donor FPs that have undergone mechanical switching cannot be excited by any excitation light in the optical system, and that acceptor FPs that have undergone mechanical switching cannot be excited by any excitation light in the optical system and also cannot accept energy from donor FPs. As such, sensors with mechanically switched acceptors (D1A0) do not undergo FRET and behave like free donors. Sensors with mechanically switched donors (D0A1) do not undergo FRET and behave like free acceptors. Sensors with both donor and acceptor mechanically switched (D0A0) do not undergo FRET and do not affect any signals. Additionally, we assume the absence of intermolecular FRET between sensors, regardless of sensor state. Using previously defined photophysical and instrumental parameters [S28], the signal contribution from each sensor state in each image channel is therefore defined in Table S3, where $E_i = f(F_i)$ is the FRET Efficiency (in the D1A1 state) for the ith sensor, ϕ_j is the fluorescence quantum yield of fluorophore j, L_j is the excitation intensity for the excitation of fluorophore j, σ_k^j is the absorption cross section of fluorophore j when excited with excitation channel k, η_k^j is the efficiency of detecting photons emitted by fluorophore j in the detection channel k.

Table S3. Signal Contributions from Each Sensor State, related to Figures 1 and S2-S4.

State	AA Signal Per Sensor	DD Signal Per Sensor	DA Signal Per Sensor		
			Sensitized Emission	Bleedthrough of Donor	Direct Acceptor Excitation
D1A1	$L_A\sigma_{Aex}^A\phi_A\eta_{Adet}^{Aem}$	$(1-E_i)\cdot(L_D\sigma_{Dex}^D\phi_D\eta_{Ddet}^{Dem})$	$E_i\cdot(L_D\sigma_{Dex}^D\phi_A\eta_{Adet}^{Aem})$	$(1-E_i)\cdot(L_D\sigma_{Dex}^D\phi_D\eta_{Adet}^{Dem})$	$L_D\sigma_{Dex}^A\phi_A\eta_{Adet}^{Aem}$
D1A0	0	$L_D\sigma_{Dex}^D\phi_D\eta_{Ddet}^{Dem}$	0	$L_D\sigma_{Dex}^D\phi_D\eta_{Adet}^{Dem}$	0
D0A1	$L_A\sigma_{Aex}^A\phi_A\eta_{Adet}^{Aem}$	0	0	0	$L_D\sigma_{Dex}^A\phi_A\eta_{Adet}^{Aem}$
D0A0	0	0	0	0	0

These expressions can be simplified by combining the photophysical and instrumental parameters into 4 constants [S28]. These (or similar) constants are routinely determined by three channel FRET calibration procedures and enable the determination of FRET efficiency from sensitized emission [S26, S27, S28]. The donor bleedthrough constant, α^{BT}, relates to the bleedthrough of photons emitted by the donor into the DA channel, and the acceptor direction excitation constant, δ^{DE}, relates to the photons from the direct excitation of the acceptor in the DA channel. They are given below:

$$\alpha^{BT} \equiv \frac{\eta_{Ddet}^{Dem}}{\eta_{Adet}^{Dem}}, \qquad \delta^{DE} \equiv \frac{L_D \sigma_{Dex}^{A}}{L_A \sigma_{Aex}^{A}}$$

Additionally, a factor for the different detection efficiencies in both channels, γ^M, and a factor for the different excitation efficiencies, β^X are defined as follows:

$$\gamma^M \equiv \frac{\phi_A \eta_{Adet}^{Aem}}{\phi_D \eta_{Ddet}^{Dem}}, \qquad \beta^X \equiv \frac{L_A \sigma_{Aex}^{A}}{L_D \sigma_{Dex}^{D}}$$

Using these four constants and an intensity scaling constant representing the signal intensity of a single acceptor fluorophore in the AA channel, $C_{AA} \equiv L_A \sigma_{Aex}^{A} \phi_A \eta_{Adet}^{Aem}$, we simplify the signal contribution from each sensor state in each image channel, yielding the expressions in Table S4.

Table S4. Signal Contributions for Each Sensor State with Simplified Parameters, related to Figures 1 and S2-S4.

State	AA Signal Per Sensor	DD Signal Per Sensor	DA Signal Per Sensor		
			Sensitized Emission	Bleedthrough of Donor	Direct Acceptor Excitation
D1A1	C_{AA}	$(1-E_i)\cdot\frac{C_{AA}}{\gamma^M\beta^X}$	$E_i\cdot\frac{C_{AA}}{\beta^X}$	$(1-E_i)\cdot\frac{\alpha_{BT}C_{AA}}{\gamma^M\beta^X}$	$\delta_{DE}\cdot C_{AA}$
D1A0	0	$\frac{C_{AA}}{\gamma^M\beta^X}$	0	$\frac{\alpha_{BT}C_{AA}}{\gamma^M\beta^X}$	0
D0A1	C_{AA}	0	0	0	$\delta_{DE}\cdot C_{AA}$
D0A0	0	0	0	0	0

From the signal contributions for each sensor state in each image channel, we derive the total signal in each image channel ($I_{AA}^{TOT}, I_{DD}^{TOT}, I_{DA}^{TOT}$) for a population of sensors existing in these four states.

$$I_{AA}^{TOT} = \sum_{D1A1} C_{AA} + \sum_{D0A1} C_{AA} \tag{S12}$$

$$I_{DD}^{TOT} = \sum_{D1A1} (1-E_i)\cdot\frac{C_{AA}}{\gamma^M\beta^X} + \sum_{D1A0} \frac{C_{AA}}{\gamma^M\beta^X} \tag{S13}$$

$$I_{DA}^{TOT} = \sum_{D1A1} \left(E_i\cdot\frac{C_{AA}}{\beta^X} + (1-E_i)\cdot\frac{\alpha_{BT}C_{AA}}{\gamma^M\beta^X} + \delta_{DE}\cdot C_{AA}\right) + \sum_{D1A0} \frac{\alpha_{BT}C_{AA}}{\gamma^M\beta^X} + \sum_{D0A1} \delta_{DE}\cdot C_{AA} \tag{S14}$$

where E_i is the FRET Efficiency (in the D1A1 state) for the ith sensor, and $\sum_{\psi_m}[\dots]$ denotes the sum over all sensors in state ψ_m.

Computation of Corrected FRET. In three channel FRET measurements, the DA channel is subject to bleedthrough of photons emitted by the donor and photons resulting from the direct excitation of the acceptor. We do not consider crosstalk between donor and acceptor here because microscope hardware is typically specified to make these effects negligeable [S26, S27, S28]. Therefore, the corrected FRET

intensity, $I_{DA\,corr}^{TOT}$ (also indicated using the variable F_C in other sensitized emission FRET formalisms) is defined as follows:

$$I_{DA\,corr}^{TOT} \equiv I_{DA}^{TOT} - \widehat{\alpha_{BT}} \cdot I_{DD}^{TOT} - \widehat{\delta_{DE}} \cdot I_{AA}^{TOT} \tag{S15}$$

where $\widehat{\alpha_{BT}}$ is the estimated donor bleedthrough constant and $\widehat{\delta^{DE}}$ is the estimated acceptor direction excitation constant, which are determined experimentally using samples containing only donor fluorophores or only acceptor fluorophores [S26, S27, S28]. As cytosolic FPs are not mechanically loaded, and these constants are routinely determined using standard three channel FRET calibration procedures [S26, S27, S28], we assume $\widehat{\alpha_{BT}} = \alpha^{BT}$ and $\widehat{\delta^{DE}} = \delta^{DE}$, i.e. no estimation error in these calibration constants. Using this result, the expression for $I_{DA\,corr}^{TOT}$ can be further simplified:

$$\begin{aligned} I_{DA\,corr}^{TOT} &\equiv I_{DA}^{TOT} - \widehat{\alpha_{BT}} \cdot I_{DD}^{TOT} - \widehat{\delta_{DE}} \cdot I_{AA}^{TOT} \\ &= \left[\sum_{D1A1}\left(E_i \cdot \frac{C_{AA}}{\beta^X} + (1-E_i)\cdot\frac{\alpha_{BT}C_{AA}}{\gamma^M\beta^X} + \delta_{DE}\cdot C_{AA}\right) + \sum_{D1A0}\frac{\alpha_{BT}C_{AA}}{\gamma^M\beta^X} + \sum_{D0A1}\delta_{DE}\cdot C_{AA}\right] - \alpha^{BT}\left[\sum_{D1A1}(1-E_i)\cdot\frac{C_{AA}}{\gamma^M\beta^X} + \sum_{D1A0}\frac{C_{AA}}{\gamma^M\beta^X}\right] \\ &\qquad - \delta^{DE}\left[\sum_{D1A1} C_{AA} + \sum_{D0A1} C_{AA}\right] \\ &= \sum_{D1A1} E_i \cdot \frac{C_{AA}}{\beta^X} \end{aligned}$$

Note that this demonstrates that sensors with non-functional donor and/or acceptor (sensors in the D1A0, D0A1, or D0A0 states) do not affect the corrected FRET signal.

Computation of Apparent FRET Efficiency and Stoichiometry. To estimate the apparent FRET Efficiency and Stoichiometry of a FRET sensor, two additional correction factors, $\widehat{\gamma^M}$ and $\widehat{\beta^X}$, must be determined for the microscope setup and fluorescent protein pair [S28]. When these constants are determined, the apparent FRET Efficiency and Stoichiometry are evaluated as follows:

$$E_{app} \equiv \frac{I_{DA\,corr}^{TOT}}{I_{DA\,corr}^{TOT} + \widehat{\gamma^M} I_{DD}^{TOT}} \tag{S16}$$

$$S_{app} \equiv \frac{I_{DA\,corr}^{TOT} + \widehat{\gamma^M} I_{DD}^{TOT}}{I_{DA\,corr}^{TOT} + \widehat{\gamma^M} I_{DD}^{TOT} + I_{AA}^{TOT}/\widehat{\beta^X}} \tag{S17}$$

The constants $\widehat{\gamma^M}$ and $\widehat{\beta^X}$ are routinely determined using standard three channel FRET calibration procedures [S26, S27, S28]. These calibrations use cytosolic FRET constructs, which are unloaded, so we assume $\widehat{\gamma^M} = \gamma^M$ and $\widehat{\beta^X} = \beta^X$, i.e. no estimation error in these calibration constants.

Expressions for Apparent FRET Efficiency and Stoichiometry for MTS Population with All Sensors Under the Same Tension and No Imaging Noise. We now derive expressions for the apparent FRET Efficiency and Stoichiometry of a sensor population in which all sensors are subject to the same force, i.e. $F_i = F_0$

for all sensors. Therefore, all sensors have the same FRET Efficiency in the D1A1 state, i.e. $E_i = E_0$ for all sensors in the D1A1 state, where $E_0 = f(F_0)$ as defined previously. For a mixed population of MTSs containing a specified number of sensors in each state ($n_{D1A1}, n_{D1A0}, n_{D0A1}, n_{D0A0}$) and having a non-zero number of sensors in the D1A1 state ($n_{D1A1} > 0$), the apparent FRET efficiency and stoichiometry can be simplified to the expressions given by Equations S18 and S19 in this section. First, we derive apparent FRET efficiency, E_{app}:

$$
\begin{aligned}
E_{app} &\equiv \frac{I_{DA\,corr}^{TOT}}{I_{DA\,corr}^{TOT} + \widehat{\gamma^M} I_{DD}^{TOT}} \\
&= \frac{\left[\sum_{D1A1} E_i \cdot \frac{C_{AA}}{\beta^X}\right]}{\left[\sum_{D1A1} E_i \cdot \frac{C_{AA}}{\beta^X}\right] + \gamma^M \left[\sum_{D1A1}(1 - E_i) \cdot \frac{C_{AA}}{\gamma^M \beta^X} + \sum_{D1A0} \frac{C_{AA}}{\gamma^M \beta^X}\right]} \\
&= \frac{E_0 \cdot n_{D1A1} \cdot \frac{C_{AA}}{\beta^X}}{E_0 \cdot n_{D1A1} \cdot \frac{C_{AA}}{\beta^X} + \gamma^M \left([n_{D1A1} \cdot (1 - E_0) + n_{D1A0}] \frac{C_{AA}}{\gamma^M \beta^X}\right)} \\
&= \frac{E_0 \cdot n_{D1A1}}{E_0 \cdot n_{D1A1} + [n_{D1A1} \cdot (1 - E_0) + n_{D1A0}]} \\
&= \frac{E_0}{1 + \left(\frac{n_{D1A0}}{n_{D1A1}}\right)}
\end{aligned}
$$

$$
E_{app} = \frac{E_0}{1 + \left(\frac{n_{D1A0}}{n_{D1A1}}\right)} \tag{S18}
$$

where $E_0 = f(F_0)$. This demonstrates that E_{app} depends only on the number of sensors in the D1A1 state (n_{D1A1}) and sensors with non-functional acceptor (n_{D1A0}), and not on the number of sensors with non-functional donor (n_{D0A1}) or both FPs non-functional (n_{D0A0}). Therefore, E_{app} is only affected by acceptor mechanical switching. This is similar to previous work showing that free donors, but not free acceptors, affect E_{app} when mixed with a population of sensors in the D1A1 state [S28]. Indeed, for the case of a sensor whose FRET is insensitive to force, Equation S18 is equivalent to the expression derived by Coullomb et al. [S28] for E_{app} for a mixed population of ideal sensors ($n_0^D = n_{D1A1}$) and free donors ($n_{free}^D = n_{D1A0}$).

Next, we derive apparent Stoichiometry, S_{app}:

$$
\begin{aligned}
S_{app} &\equiv \frac{I_{DA\,corr}^{TOT} + \widehat{\gamma^M} I_{DD}^{TOT}}{I_{DA\,corr}^{TOT} + \widehat{\gamma^M} I_{DD}^{TOT} + \frac{I_{AA}^{TOT}}{\widehat{\beta^X}}} \\
&= \frac{\left[\sum_{D1A1} E_i \cdot \frac{C_{AA}}{\beta^X}\right] + \gamma^M \left[\sum_{D1A1}(1 - E_i) \cdot \frac{C_{AA}}{\gamma^M \beta^X} + \sum_{D1A0} \frac{C_{AA}}{\gamma^M \beta^X}\right]}{\left[\sum_{D1A1} E_i \cdot \frac{C_{AA}}{\beta^X}\right] + \gamma^M \left[\sum_{D1A1}(1 - E_i) \cdot \frac{C_{AA}}{\gamma^M \beta^X} + \sum_{D1A0} \frac{C_{AA}}{\gamma^M \beta^X}\right] + \frac{1}{\beta^X}\left[\sum_{D1A1} C_{AA} + \sum_{D0A1} C_{AA}\right]}
\end{aligned}
$$

$$= \frac{E \cdot n_{D1A1} \cdot \frac{C_{AA}}{\beta^X} + \gamma^M \left([n_{D1A1} \cdot (1-E) + n_{D1A0}] \frac{C_{AA}}{\gamma^M \beta^X} \right)}{E \cdot n_{D1A1} \cdot \frac{C_{AA}}{\beta^X} + \gamma^M \left([n_{D1A1} \cdot (1-E) + n_{D1A0}] \frac{C_{AA}}{\gamma^M \beta^X} \right) + \frac{(n_{D1A1} + n_{D0A1}) \cdot C_{AA}}{\beta^X}}$$

$$= \frac{E \cdot n_{D1A1} + n_{D1A1} \cdot (1-E) + n_{D1A0}}{E \cdot n_{D1A1} + n_{D1A1} \cdot (1-E) + n_{D1A0} + (n_{D1A1} + n_{D0A1})}$$

$$= \frac{(n_{D1A1} + n_{D1A0})}{(n_{D1A1} + n_{D1A0}) + (n_{D1A1} + n_{D0A1})}$$

$$S_{app} = \frac{n_{D1A1} + n_{D1A0}}{(n_{D1A1} + n_{D1A0}) + (n_{D1A1} + n_{D0A1})} \quad \text{(S19)}$$

This demonstrates that S_{app} depends on the number of sensors in the D1A1 state (n_{D1A1}) and the number of sensors with either non-functional acceptor (n_{D1A0}) or non-functional donor (n_{D0A1}). Therefore, as expected, S_{app} can be affected by both acceptor and donor mechanical switching. This is again consistent with previous work showing that free donor or free acceptor can both affect S_{app} when mixed with a population of sensors in the D1A1 state [S28]. By combining the total number of functional donor ($n_D = n_{D1A1} + n_{D1A0}$) and acceptor FPs ($n_A = n_{D1A1} + n_{D0A1}$), we also show that $S_{app} = \frac{n_D}{n_D + n_A}$, which means that S_{app} remains a true readout of functional FP stoichiometry in the presence of mechanical switching of the acceptor and/or donor.

To validate the derived expressions for E_{app} and S_{app} (Equations S18 and S19), we confirmed exact agreement with values of E_{app} and S_{app} computed directly from simulated raw channel intensities using Equations S12-S17. Validation results for different populations of sensor states ($n_{D1A1}, n_{D1A0}, n_{D0A1}, n_{D0A0}$) and forces F are shown in Figure S3. The validations shown in Figure S3 were performed with FRET calibration constants similar to those for the mTFP1-mVenus FRET pair and microscope setup used in our experimental work ($\widehat{\alpha_{BT}} = 0.75, \widehat{\delta^{DE}} = 0.25, \widehat{\gamma^M} = 1.65, \widehat{\beta^X} = 0.6061$) and with intensity values ($C_{AA} = 100$) similar to those in our experimental system. However, the derived expressions hold for all FRET calibration constants and raw channel intensity values.

B. Results

1. Development of a Framework to Assess FP Mechanical Switching in MTS

To visualize MTS data in the presence of FP mechanical switching, we sought to adapt a recently developed framework for plotting three-channel FRET data using the apparent FRET efficiency, E_{app}, and apparent stoichiometry, S_{app} [S28]. MTSs have a continuously variable FRET efficiency in the D1A1 state, $E_0(F)$, that depends on the molecular tension according to a FRET efficiency versus tension calibration curve [S1, S2] (Figure S4a). Therefore, in the absence of FP mechanical switching, increasing tension leads to a decrease in E_{app} with a constant $S_{app} = 0.5$ (Figure S4b). In this case, E_{app} for an ensemble of MTSs under a single tension F remains equal to the calibrated value, $E_0(F)$. In the presence of FP mechanical switching, deviations from $S_{app} = 0.5$ occur. Acceptor mechanical switching increases S_{app} and decreases E_{app} moving the (E_{app}, S_{app}) point up and left (Figure S4c, dots indicate different distributions of D1A1 and D1A0 states for 3 pN). Donor mechanical switching decreases S_{app} and does not affect E_{app}, moving the (E_{app}, S_{app}) point down (Figure S4d, dots indicate different distributions of D1A1 and D0A1 states for 3 pN). To establish references, we define tension isoclines as the curves containing (E_{app}, S_{app}) points for an MTS ensemble under a single tension F (and thus having a single E_0) with all levels of acceptor mechanical switching only or donor mechanical switching only.

Taken together, this establishes a framework for visualizing three channel FRET measurements of MTSs using E_{app} and S_{app}. This framework applies generally to MTSs containing any type of non-functional acceptor or donor FPs. We assess its suitability specifically for detecting FP mechanical switching in MTSs in the following sections.

2. Effect of Acceptor Mechanical Switching in Dynamic MTSs

We next assessed the suitability of this framework for detecting FP mechanical switching in MTSs that undergo dynamic binding, loading, and unbinding. To do so, we used the kinetic model of FP mechanical switching in dynamic MTSs to obtain the steady state fractions of sensors in each of the four possible states for an MTS population subject to a specified load magnitude and duration and then computed the resulting (E_{app}, S_{app}) value. First, we analyzed computed FRET measurements for populations of MTSs undergoing acceptor mechanical switching only.

To assess the ability to detect acceptor mechanical switching inside MTS, we compared readouts for an MTS with no acceptor mechanical switching or other loss-of-function (Figure S5c, brown line), an MTS with force-independent acceptor loss-of-function such as due to photobleaching or large differences in FP maturation time (Figure S5c, grey line), and an MTS with acceptor mechanical switching (Figure S5c, black line; base parameters in Table S2). We looked at (E_{app}, S_{app})-curves for load magnitude F from 0 to 30 pN and a load duration τ of 1 second. In the absence of acceptor mechanical switching (Figure S5c, brown line), the (E_{app}, S_{app})-curve starts at the point ($E_{app} = E_0(F = 0) = 0.286$, $S_{app} = 0.5$), corresponding to an unloadable tension sensor module, and as the load magnitude increases E_{app} decreases while S_{app} remains constant. Thus, an MTS without acceptor mechanical switching exhibits a horizontal (E_{app}, S_{app}) signature at $S_{app} = 0.5$. In the case of force-independent acceptor loss-of-function (Figure S5c, grey line), the (E_{app}, S_{app})-curve starts at a lower E_{app} and a higher S_{app} than that of the unloaded tension sensor module. As load magnitude increases, E_{app} decreases but S_{app} does not change. Thus, an MTS with force-independent acceptor loss-of-function exhibits a horizontal (E_{app}, S_{app}) signature at $S_{app} > 0.5$. For the case of acceptor mechanical switching (Figure S5c, black line), the (E_{app}, S_{app})-curve again starts at the point corresponding to the unloaded tension sensor module. While E_{app} again decreases with load magnitude, S_{app}increases with load magnitude for loads near and above the FP's threshold force ($F \geq F_{1/2}^{A}$). Thus, acceptor mechanical switching exhibits an up/left slanting (E_{app}, S_{app}) signature. Therefore, these data indicate that acceptor mechanical switching has a unique (E_{app}, S_{app}) signature that can be distinguished from cases of no acceptor mechanical switching as well as force-independent acceptor loss-of-function.

A large set of natural and engineered FPs with different structures, photophysical properties, and mechanical stabilities exist, and the integration of FPs into a fusion protein as well as the use of FPs in the cellular environment can alter these properties [S2, S10, S24, S25]. As such, we next assessed the sensitivity of the acceptor mechanical switching signature to mechanical switching parameters. Increasing the acceptor force threshold $F_{1/2}^{A}$ increases the load magnitude and E_{app} point at which S_{app} begins to increase (Figure S5d). After the departure from $S_{app} = 0.5$, all (E_{app}, S_{app})-curves exhibit monotonic decreases in E_{app} and increases in $S_{app}$with increasing load magnitude. In comparison, increasing the acceptor kinetic rate constant $k_{MS,0}^{A}$ increases the slope of the (E_{app}, S_{app}) curve (Figure S5e). Again, all (E_{app}, S_{app})-curves exhibit monotonic decreases in E_{app} and increases in $S_{app}$with increasing load magnitude. Therefore, these data indicate that the (E_{app}, S_{app})-curve has differential

sensitivity to acceptor mechanical switching parameters, but that the overall up/left slanting (E_{app}, S_{app}) trend applies for all cases of acceptor mechanical switching in the loading regimes where it occurs.

Taken together, these data indicate that acceptor mechanical switching has a unique up/left slanting (E_{app}, S_{app}) signature that is robust to FP mechanical switching parameters and can be distinguished from cases of no acceptor mechanical switching as well as force-independent acceptor loss-of-function.

3. Effect of Donor Mechanical Switching in Dynamic MTSs

To assess the ability to detect donor mechanical switching inside MTS, we compared readouts for an MTS with no donor mechanical switching or other loss-of-function (Figure S6c, brown line), an MTS with force-independent donor loss-of-function such as due to photobleaching or large differences in FP maturation time (Figure S6c, grey line), and an MTS with donor mechanical switching (Figure S6c, black line; base parameters in Table S2). We looked at (E_{app}, S_{app})-curves for load magnitude F from 0 to 30 pN and a load duration τ of 1 second. In the absence of donor mechanical switching (Figure S6c, brown line), the (E_{app}, S_{app})-curve starts at ($E_{app} = E_0(F = 0) = 0.286$, $S_{app} = 0.5$), corresponding to an unloadable tension sensor module, and as the load magnitude increases E_{app} decreases while S_{app} remains constant. Thus, an MTS without donor mechanical switching exhibits a horizontal (E_{app}, S_{app}) signature at $S_{app} = 0.5$. In the case of force-independent donor loss-of-function (Figure S6c, grey line), the (E_{app}, S_{app})-curve starts at the same E_{app} but a lower S_{app} than that of the unloaded tension sensor module. As load magnitude increases, E_{app} decreases but S_{app} does not change. Thus, an MTS with force-independent donor loss-of-function exhibits a horizontal (E_{app}, S_{app}) signature at $S_{app} < 0.5$. For the case of donor mechanical switching (Figure S6c, black line), the (E_{app}, S_{app})-curve again starts at the point corresponding to the unloaded tension sensor module. While E_{app} again decreases with load magnitude, S_{app} decreases with load magnitude for loads near and above the FPs threshold force ($F \geq F_{1/2}^{D}$). Thus, donor mechanical switching exhibits a down/left slanting (E_{app}, S_{app}) signature.
Furthermore, the response these data have to donor mechanical switching parameters resembles the response described for acceptor mechanical switching in the previous section. Briefly, donor force threshold ($F_{1/2}^{D}$) controls the E_{app} value at which the (E_{app}, S_{app})-curve diverges from $S_{app} = 0.5$ and the donor kinetic rate constant ($k_{MS,0}^{D}$) controls the slope of the (E_{app}, S_{app})-curve, but in all cases the down/left slanting (E_{app}, S_{app}) signature for donor mechanical switching remains (Figure S6d-e).

Taken together, these data indicate that donor mechanical switching has a unique down/left (E_{app}, S_{app}) signature that is robust to FP mechanical switching parameters and can be distinguished from cases of no donor mechanical switching as well as force-independent donor loss-of-function.

4. FP Mechanical Switching in MTSs is Sensitive to both Load Magnitude and Duration

The mechanical switching of single FPs in load-bearing proteins was sensitive to both load magnitude and duration (Figure S1), so we next assessed if FRET measurements of MTSs with acceptor or donor mechanical switching were sensitive to both loading parameters. To assess the effect of load duration at a given load magnitude, we varied the load duration τ over a range from 0.01 to 100 seconds at constant load magnitude F. For acceptor mechanical switching, the (E_{app}, S_{app})-curve moves up/left with increasing load duration, tracking along the tension isocline (Figure S7a). For donor mechanical switching, the (E_{app}, S_{app})-curve moves vertically down with increasing load duration, similarly tracking along the tension isocline (Figure S7b).

For comparison, we assessed the effect of load magnitude at a given load duration. To do so, we varied the load magnitude F over a range from 0 to 30 pN at constant load duration τ (Figure S7c-d). For the case of acceptor mechanical switching, S_{app} always increases and E_{app} always decreases in response to increases in either load magnitude (Figure S7c) or duration (Figure S7a). Thus, both produce up/left (E_{app}, S_{app})-curves, with slopes being steeper for load duration variation compared to load magnitude variation. For the case of donor mechanical switching, S_{app} always decreases in response to increases in either load magnitude (Figure S7d) or duration (Figure S7b), and E_{app} either decreases or remains constant, for changes in load magnitude or duration, respectively.

Taken together, this data suggests that the (E_{app}, S_{app}) signatures for FP mechanical switching in MTSs are sensitive to changes in both load magnitude and duration and that they respond to these loading parameters differently.

5. Dominant mechanical switching in one FP is detectable in presence of weaker mechanical switching in the other FP

We next assessed how the ability to detect mechanical switching in one FP is affected by the presence of weaker levels of mechanical switching in the other FP. To do so, we modeled one FP exhibiting mechanical switching with the base parameters (Table S2) and the other FP exhibiting lower levels of mechanical switching (lower rate constant $k^D_{MS,0}/k^A_{MS,0}$ or higher force threshold $F^D_{1/2}/F^A_{1/2}$). For acceptor mechanical switching in the presence of donor mechanical switching with lower rate constant ($k^D_{MS,0} < k^A_{MS,0}$) but equal force threshold ($F^D_{1/2} = F^A_{1/2}$), increasing amounts of donor mechanical switching (increasing $k^D_{MS,0}$) leads to a reduction in S_{app} (Figure S8a, blue and orange lines) compared to case of acceptor mechanical switching only (Figure S8a, black line). The up/left (E_{app}, S_{app})-curve is preserved but with a reduced slope. Further increases in donor mechanical switching up to the level of acceptor mechanical switching causes S_{app} to return to 0.5 and the (E_{app}, S_{app})-curve to have zero slope (Figure S8a, yellow line; data signatures of identical mechanical switching parameters for donor and accepter are discussed further in Section IV). Donor mechanical switching in the presence of acceptor mechanical switching with lower rate constant ($k^A_{MS,0} < k^D_{MS,0}$) but equal force threshold ($F^A_{1/2} = F^D_{1/2}$) displays a similar behavior but with effects in the opposite direction (Figure S8b). Therefore, in both cases, (E_{app}, S_{app})-curves for dominant acceptor or donor mechanical switching in the presence of lower levels of mechanical switching in the other FP retain their up/left or down/left signatures, respectively.

We next investigated differences in the FP force threshold. For acceptor mechanical switching in the presence of donor mechanical switching with higher force threshold ($F^D_{1/2} > F^A_{1/2}$) but equal constant ($k^D_{MS,0} = k^A_{MS,0}$), effects on the (E_{app}, S_{app})-curves are only seen at load magnitudes near and above $F^D_{1/2}$ (Figure S8c). Above these load magnitudes, S_{app} reduces with increased load magnitude, approaching 0.5. A similar effect in the opposite direction is observed for the case of dominant donor mechanical switching (Figure S8d). Despite changes in the (E_{app}, S_{app})-curve at higher loads, the deviations in S_{app} from 0.5 as well as the shape of the (E_{app}, S_{app})-curve at lower loads remained unchanged. As such, they remain reliable indicators of the FP that exhibits dominant mechanical switching.

Taken together, this data demonstrates that dominant acceptor or donor mechanical switching in the presence of lower levels of mechanical switching in the other FP are detectable from their (E_{app}, S_{app}) signatures.

IV. Visualization of Experimental Data

To facilitate visualization of experimental data, we next conducted simulations that account for phenomena likely to be present in experimental data, including variability in protein loading dynamics and intrinsic noise due to inherent stochasticity of kinetic processes. Protein loading dynamics likely vary within and between cells. For instance, F-actin flow speeds and polymerization rates (two sources of protein loading in cells) vary spatially with distance from the cell edge [S30]. Additionally, traction stresses and vinculin molecular tension vary between and within focal adhesions, and heterogeneity of traction stresses across cell populations has also been reported [S2, S15, S31, S32, S33]. Together, this suggests subcellular heterogeneity in protein loading dynamics (i.e. differences in protein loading dynamics between populations of mechanical proteins in different cells and at different subcellular locations in the same cell). Therefore, we conducted simulations where the load magnitude and/or duration for each ensemble were drawn from distributions.

A. Model Formulation

1. Stochastic Simulations

We simulated ensembles of MTSs consisting of $n_{sensors}$ sensors that are subject to dynamic loading and undergo FP mechanical switching according to the kinetic model for FP mechanical switching in MTSs described in Section III.A. All MTSs in a given ensemble exhibit the same FP mechanical switching parameters and are subject to the same dynamic loading conditions, parameterized by the load magnitude F and a characteristic load duration τ ($\tau \equiv 1/k_{unbind}$). Stochastic simulations were performed using the Gillespie Algorithm [S34], starting with all MTSs in the D1A1 state and running until the number of sensors in each of the 4 MTS states reached a steady state. Then, the state of each sensor was sampled, and this information was used to compute the experimentally observable readouts of three channel FRET as described in Section III.A.

2. Simulations with Distributions in Load Magnitude and Duration Between Ensembles

For each parameter combination, we simulated $N_{sims} = 1000$ MTS ensembles each containing $n_{sensors} = 50$ total sensors. The apparent FRET Eff (E_{app}) and Stoichiometry (S_{app}) was computed for each simulation and displayed in ES histograms. As protein loading dynamics likely vary within and between cells [S2, S15, S31, S32, S33], we conducted simulations where the load magnitude and/or duration for each ensemble were drawn from distributions. As little is known about the distribution of forces on proteins inside cells, and because we sought to interpret the data for both synthetic MTSs and MTSs for naturally occurring proteins, we chose simple generic distributions. Specifically, the k-th ensemble is assigned a load magnitude F_k that is drawn from a uniform distribution on the interval 0 to 10 pN, i.e. $F_k \sim Uniform(0,10)$. Likewise, the characteristic load duration τ_k was drawn from a log-uniform distribution from $10^{-0.5}$ to $10^{0.5}$ s, i.e. $\log_{10}(\tau_k) \sim Uniform\big(\log_{10}(-0.5), \log_{10}(0.5)\big)$. As previously defined, the unloading rate constant was $k_{unbind,k} = 1/\tau_k$. Within each single ensemble, all MTSs are subjected to the same loading conditions.

B. Results

To facilitate data visualization, we investigated signatures of FP mechanical switching in MTSs in the presence of variability in the protein loading conditions as well as intrinsic noise due to inherent stochasticity of kinetic processes. We considered four scenarios: no FP mechanical switching, only acceptor mechanical switching (with base parameters in Table S2), only donor mechanical switching (with base parameters in Table S2), and both acceptor and donor mechanical switching at equal levels (with base parameters in Table S2). For each scenario, we investigated the (E_{app}, S_{app})-distribution for

variable load magnitude, variable load duration, and variable load magnitude and load duration. The histograms presented in this section match all trends described in Section III, but the histograms are expected to provide more realistic data signatures for comparison to experimental data as they account for phenomena likely present in experimental data, including variability in protein loading dynamics and intrinsic noise due to inherent stochasticity of kinetic processes.

We first considered variations in load magnitude only. Here, the (E_{app}, S_{app})-distribution in the absence of FP mechanical switching is horizontal along $S_{app} = 0.5$ to the left of the unloaded $E_{app} = 0.286$ (Figure S9a). For acceptor only mechanical switching, the (E_{app}, S_{app})-distribution has an up/left sloping signature (Figure S9d). For donor only mechanical switching, the (E_{app}, S_{app})-distribution has a down/left sloping signature (Figure S9g). These results match the trends described in detail in Figures S5-S6 and Section III.B.2-3. For both acceptor and donor mechanical switching at equal levels, the (E_{app}, S_{app})-distribution is centered horizontally along $S_{app} = 0.5$ with increasing spread in S_{app} at lower E_{app} (Figure S9j). This case of acceptor and donor mechanical switching at equal levels (Figure S9j) is clearly distinguishable from the case of no FP mechanical switching (Figure S9a) by the significantly increased spread in S_{app} at lower E_{app}.

We next considered variations in load duration only. Here, the (E_{app}, S_{app})-distribution in the absence of FP mechanical switching occupies a single point at $S_{app} = 0.5$ and the $E_{app} = E_0(F)$ (Figure S9b), and the cases of acceptor only (Figure S9e) or donor only (Figure S9h) mechanical switching have up/left or vertical down (E_{app}, S_{app})-distributions, as described in detail in Figure S7 and Section III.B.4. For both acceptor and donor mechanical switching at equal levels, the (E_{app}, S_{app})-distribution lies on and to the left of an (E_{app}, S_{app}) point with spreads in both E_{app} and S_{app} (Figure S9k).

We lastly considered variations in both load magnitude and load duration (Figure S9c,f,i,l). For all four cases of FP mechanical switching, the (E_{app}, S_{app})-distributions closely resemble the corresponding distributions for variations in load magnitude only, except that there is increased spread in S_{app} at lower E_{app} for the three cases of FP mechanical switching (Figure S9f,i,l).

Taken together, these data provide unique data signatures for experimental data containing no FP mechanical switching, only acceptor mechanical switching, only donor mechanical switching, and both acceptor and donor mechanical switching at equal levels in the presence of cell-to-cell and/or subcellular heterogeneity in protein loading as well as intrinsic noise.

V. Force-Dependent Bonds and Variable Loading Rates

Mechanical forces affect the lifetime of most intermolecular bonds [S35]. Many of the mechanical proteins that transmit forces within the cytoskeleton or between the cytoskeleton and the extracellular environment exhibit force-sensitive bonds, and force-sensitive bond dynamics play an important role in mechanosensitive processes [S4, S7]. For example, the mechanical linker protein vinculin exhibits a force-activated bond with F-actin [S17], and its turnover at focal adhesions is stabilized by molecular tension [S3]. Furthermore, cells transmit forces to the ECM and sense mechanical properties of the ECM through molecular linkages at FAs [S4, S7, S36]. These linkages couple the ECM to the actin cytoskeleton, transmitting forces from retrograde flowing actin [S4, S7, S36]. Importantly, alterations in ECM stiffness are thought to be sensed through changes in the loading rate of molecular linkages in FAs [S7]. Therefore, force-sensitive bond dynamics and loading rate are two important aspects of protein loading

dynamics. In this section we extend our model of FP mechanical switching in MTSs to assess effects of force-sensitive bond dynamics and loading rate.

A. Model Formulation

1. Force-Sensitive Unbinding Rate Constants

Three generic bond models are commonly used to represent the major responses of bonds to mechanical force: insensitivity, destabilization, and stabilization. An **ideal bond**, identical to k_{unbind} in the preceding sections, represents a bond that is insensitive to load magnitude F on the scale of those experienced by load-bearing proteins inside cells:

$$k_{unbind}(F) = k_{off,0} \tag{S20}$$

A **slip bond** represents a destabilizing bond whose lifetime decreases with load magnitude F on the scale of those experienced by load-bearing proteins inside cells:

$$k_{unbind}(F) = k_{off,0} e^{F/F_b} \tag{S21}$$

where $k_{off,0}$ is the intrinsic unbinding rate constant and F_b determines the sensitivity of the bond to force. Lastly, a two-pathway **catch-slip bond** is often used to represent a stabilizing bond whose lifetime initially increases with load magnitude F before decreasing at higher load magnitudes. We define a rate constant that fits this form as follows:

$$k_{unbind}(F) = k_{off,0}\left(0.9e^{-2F/F_b} + 0.1e^{F/F_b}\right) \tag{S22}$$

where $k_{off,0}$ is the intrinsic unbinding rate constant and F_b determines the sensitivity of the bond to force.

2. Incorporation of Force-Sensitive Bonds into the Model of FP Mechanical Switching in MTSs

An additional model was implemented exactly as described in Section III but with replacing the unbinding rate constant for the MTS, k_{unbind}, with one of the three $k_{unbind}(F)$ functions (Equations S20-S22) in the steady state analysis (Equations S6-S9). E_{app} and S_{app} were computed as in Section III using Equations S18-S19.

3. Loading Rate Control

These methods apply to the data in Section V.B.2 only. Instead of subjecting each MTS to the same load magnitude F as before, each MTS was now subjected to the same loading rate dF/dt. All MTSs in an ensemble exhibit the same FP mechanical switching parameters and have the same unbinding rate constant $k_{unbind}(F)$. Stochastic simulations were conducted to analyze this model. Specifically, MTS ensembles were simulated according to the methods and parameters in Section IV, except for the following modifications. For each sensor i in an ensemble, the force F_i was updated at each timestep dt using the equation $F_i = (dF/dt) \cdot dt$. Upon unbinding, which occurred with a rate $k_{unbind}(F_i)$, F_i was reset to 0, corresponding to the unloaded state, followed by FP recovery (if applicable) and immediate re-binding and loading. In this scenario, each MTS inside a single ensemble can have a different F_i value, and thus different E_i value. As a result, E_{app} and S_{app} must be computed directly from the channel

intensities using Equations S12-S17. Additionally, due to the enhanced complexity, no analytical expressions for average steady state species abundances or E_{app} and S_{app} were derived. Instead, (E_{app}, S_{app})-curves were plotted using the averages from stochastic simulations. For each parameter combination, we simulated $N_{sims} = 100$ MTS ensembles each containing $n_{sensors} = 50$ total sensors.

B. Results

1. Effect of Force-Sensitive Bond Dynamics on FP Mechanical Switching

To assess how FP mechanical switching in an MTS is affected by force-dependent bond dynamics, we investigated bonds whose durations are insensitive (ideal; Equation S20), destabilized (slip; Equation S21), or stabilized (catch-slip; Equation S22) by forces on the scale of those experienced by load-bearing proteins inside cells (Figure S10a-c). Acceptor or donor mechanical switching parameters were held constant at the base values from Table S2.

We first assessed effects associated with the functional form of the three bond models. To do so, we compared bonds with identical intrinsic rate constants ($k_{off,0} = 1$ sec) and with equal force-sensitivities for the slip and catch-slip bonds ($F_b = 5$ pN) (Figure S10d). The up/left slanting (E_{app}, S_{app}) signature of acceptor mechanical switching for the ideal bond has already been described (Section III). At low and intermediate loads, the slip and catch-slip bonds both match the up/left slanting (E_{app}, S_{app}) signature of the ideal bond (Figure S10e). Over this range of loads, slip bonding reduces the amount of FP mechanical switching by reducing the loading duration, while catch bonding increases the amount of FP mechanical switching by increasing the loading duration. At higher loads, both the slip and catch-slip bond exhibit decreased S_{app} (i.e. a return toward 0.5) due to large reductions in bond duration at high forces, leading to rapid MTS unbinding and recovery of FP function. The sensitivity of FP mechanical switching to force-sensitive bonds is thus consistent with the previously determined importance of load duration (Figure S1 and Figure S7). For donor mechanical switching, a similar effect of slip and catch-slip bonding is observed, although with S_{app} moving to lower values before increasing back toward 0.5 at higher loads (Figure S10f). Together, these results indicate that FP mechanical switching is sensitive to force-sensitive bond dynamics at load magnitudes near the characteristic force sensitivity of the bond, with slip bonding reducing FP mechanical switching and catch bonding enhancing FP mechanical switching.

To comprehensively assess effects of force-dependent bond dynamics on the (E_{app}, S_{app}) signatures, we next looked at slip (Figure S10g-i) and catch-slip (Figure S10j-l) bonds with a wide range of characteristic force sensitivities (F_b from 1 to 25 pN). Slip and catch-slip bonds that rapidly destabilize at load magnitudes below the characteristic force threshold of the FP ($F_b \ll F_{1/2}^A$ or $F_b \ll F_{1/2}^A$) do not permit FP mechanical switching (e.g. orange line in Figure S10h-j,i-k). For slip and catch-slip bonds with higher F_b values, FP mechanical switching is enhanced. At these higher F_b values, slip and catch-slip bonds resemble the signatures of ideal bonds: up/left slanting (E_{app}, S_{app}) signatures for acceptor mechanical switching (Figure S10h,k) and down/left slanting (E_{app}, S_{app}) signatures for donor mechanical switching (Figure S10i,l), up to the load magnitude at which both slip and catch-slip bonds begin to rapidly destabilize causing decreases in S_{app} toward 0.5 at the highest load magnitudes. We again see differences in the absolute position of the (E_{app}, S_{app}) data for ideal, slip, and catch-slip bonds at load magnitudes near F_b, confirming the response of FP mechanical switching to force-sensitive bond dynamics. Lasty, for sufficiently high values of F_b, slip and catch-slip bonds approach the behavior of an ideal bond, which is expected because as F_b tends to infinity both bond models become ideal bonds.

Lastly, we assessed the effect of force-dependent bonds on ES-histograms of MTS populations subject to variable load magnitudes (analogous to Figure S9a,d,g,j), which represent effects of cell-to-cell and/or subcellular heterogeneity in protein loading as well as intrinsic noise (see Section IV). Specifically, we simulated populations of MTSs with ideal, slip, or catch-slip bonds subjected to a load magnitude ranging from 0 to 10 pN (uniformly distributed) with the cases of neither, acceptor only, donor only, or both FPs undergoing FP mechanical switching (Figure S11). Compared to the ideal bond (Figure S11d,g,j), the slip bond reduces the amount of FP mechanical switching for cases of acceptor only (Figure S11e), donor only (Figure S11h), and acceptor and donor (Figure S11k) mechanical switching, as indicated by S_{app} values closer to 0.5 at intermediate and lower E_{app} values. In contrast, the catch-slip bond increases the amount of FP mechanical switching at intermediate forces for cases of acceptor only (Figure S11f), donor only (Figure S11i), and acceptor and donor (Figure S11l) mechanical switching, as indicated by S_{app} values farther away from 0.5 at intermediate E_{app} values compared to ideal and slip bonds. As weaking of the catch-slip bond occurs above the maximum load magnitude (10 pN) simulated here, a restoration of S_{app} values back toward 0.5 is not observed here but would exist for weaker catch-slip bonds and/or higher maximum forces.

Together, these analyses identify the effects of force-sensitive bonds on FP mechanical switching. Across low and intermediate loads, MTSs with slip or catch-slip bonding retain the general (E_{app}, S_{app}) signatures for acceptor (up/left) and donor (down/left) mechanical switching reported for ideal bonds (Sections III and IV). However, in this force regime, slip bonding reduces the amount of FP mechanical switching in comparison to ideal bonds by reducing the loading duration, while catch bonding increases the amount of FP mechanical switching by increasing the loading duration. Lastly, at high loads, both slip and catch-slip bonds lead to reductions in FP mechanical switching compared to ideal bonds due to large reductions in load duration. Overall, these results suggest that perturbations to force-sensitive bonding of an MTS can lead to drastic changes in the amount of FP mechanical switching within the MTS.

2. Effect of Changes in Loading Rate on FP Mechanical Switching

To assess the effect of load rate, ensembles of MTS were simulated in which each MTS was loaded at a constant rate dF/dt and was unloaded upon unbinding/rebinding (Figure S12a). As there are no direct measurements of protein loading rates inside cells, a range of loading rates (0.1 to 100 pN/s) was chosen to encompass recent estimates for the loading rate of integrin-based linkages (1-8 pN/s based on actin retrograde flow speeds and talin domain unfolding tensions) [S37]. For these simulations, acceptor or donor mechanical switching parameters were held constant at the base values from Table S2. Unbinding rate constants for ideal, slip, or catch-slip bonds were used, all with identical intrinsic rate constants ($k_{off,0} = 1$ sec) and with equal force-sensitivities for the slip and catch-slip bonds ($F_b = 5$ pN) (Figure S12b). For acceptor mechanical switching in an MTS with an ideal bond, increasing the loading rate produces an up/left movement of the (E_{app}, S_{app}) data (simulated MTS populations for 4 different loading rates shown separately in Figure S12c, and averages are plotted together in Figure S12f). This indicates that acceptor mechanical switching increases with loading rate across all probed rates when MTSs have an ideal bond. This high degree of FP mechanical switching occurs for an ideal bond because higher load magnitudes are reached at higher loading rates when bond lifetime (and thus load duration) is independent of load rate. For the slip bond, increases in loading rate produce a flatter up/left movement of the (E_{app}, S_{app}) data across lower loading rates, i.e. S_{app} remains closer to 0.5 as E_{app} decreases, and S_{app} returns to 0.5 at higher loading rates due to reduced load duration (Figure S12d,f). For the catch-slip bond, increases in loading rate produce a steeper up/left movement of the (E_{app}, S_{app}) data across low and intermediate loading rates (compared to both the ideal and slip bonds), with S_{app} again moving back toward 0.5 at the highest loading rates due to reduced load duration (Figure

S12e,f). These trends arise for force-sensitive bonds because the distributions of load magnitude and duration are now set by the competition between loading rate and unbinding rate. For the slip bond this results in the highest levels of FP mechanical switching at lower loading rates. For the catch-slip bond this results in the highest levels of FP mechanical switching at intermediate loading rates. For donor mechanical switching, increased loading rate has analogous effects for all three types of bonds (ideal, slip, or catch-slip), although with S_{app} moving to lower values before increasing back toward 0.5 (Figure S12g-j).

Overall, consistent with the previously demonstrated sensitivity to variations in load magnitude and/or duration (Figure S7), this data indicates that FP mechanical switching in MTSs is sensitive to changes in loading rate, and that the sensitivity to loading rate depends on the force-sensitivity of the bond mediating loading. As ECM stiffness is one factor that controls the loading rate of proteins in FAs [S7], this data also suggests the existence of regimes where FP mechanical switching in MTS is sensitive to substrate stiffness.

VI. Assumptions and Limitations

Here we discuss model assumptions and limitations. First, we cover those of the kinetic model of FP mechanical switching in MTSs. Then, we cover those of sensitized emission-based FRET measurements.

1. Kinetic Model of Protein Loading Dynamics and FP Mechanical Switching

As little is known about the time-dependent loading profiles of proteins inside cells, we considered as a starting point two simple loading profiles, constant load magnitude or constant loading rate. In the first case, MTSs are subjected to a constant load magnitude F for a load duration τ, driven by stochastic unbinding from a loading source ($\tau \equiv 1/k_{unbind}$). This step function loading profile is analogous to the force-clamp loading profile commonly used in single molecule experiments in vitro [S8]. In the second case, MTSs are subjected to linear ramp loading (at constant loading rate dF/dt), again with stochastic unbinding from the loading source. This is analogous to the force-ramp loading profile used in single molecule experiments in vitro [S38]. The loading profiles of mechanical linkages in cells are likely more complex than the step or ramp profiles used here, possibly involving forces or extensions that vary nonlinearly with time and/or saturate. Although differences in these loading profiles will affect the extent of FP mechanical switching, the simplified models presented here are sufficient for assessing how protein loading dynamics affect FP mechanical switching and thereby provide insight into the response of FP mechanical switching in more complex loading conditions.

Furthermore, the model focuses on the competing timescales of FP mechanical switching and protein loading dynamics. As such, following the unloading of an MTS, we used the simplifying assumption that FPs that underwent mechanical switching are immediately restored to the functional state. We note that this is consistent with the rapid recovery of FPs in unloaded MTSs and/or the exchange of unloaded MTSs with a cytoplasmic pool of MTSs in the D1A1 state. In reality, a mechanical protein at a specific structure in the cell (e.g. a focal adhesion or actin fiber) engages/disengages from a loading source (e.g. actin), potentially undergoing multiple loading cycles before exchanging from the disengaged state with a pool of freely diffusing cytoplasmic proteins. In this context, the characteristic load duration ($\tau \equiv 1/k_{unbind}$) represents the duration over which the MTS continuously experiences loads and neither FP recovery nor MTS turnover occurs. For a protein that rapidly turns over following disengagement, like a rapidly diffusing actin binding protein, τ corresponds more closely to the turnover timescale of the protein. On the other hand, for a protein that undergoes many cycles of engagement/disengagement (loading/unloading), like a slowly diffusing trans-membrane protein, τ corresponds more closely to the

disengagement timescale of the protein, which would be driven by the unbinding rate constant for the shortest-lived bond in the mechanical linkage (e.g. ECM:integrin:talin:vinculin:F-actin). Overall, the model is sufficient to assess the competing timescales of FP mechanical switching versus MTS loading dynamics. In the future, more complex models explicitly incorporating binding, unbinding, and turnover as separate processes could be used to explore the interactions between more processes, like MTS rebinding versus FP recovery or sensor turnover.

To investigate subcellular and cell-to-cell heterogeneity in protein loading [S2, S15, S32, S33], we implemented distributions in load magnitude and duration between MTS populations. As little is known about the distribution of forces on proteins inside cells, we chose simple generic distributions for these two parameters. Other load magnitude distributions, such as those with long tails at higher forces, will produce similar results for cases where the FP force thresholds ($F_{1/2}^{D}$ and $F_{1/2}^{A}$) are close to the mode of the distribution. Alternatively, if the FP force thresholds are considerably higher than the mode of the distribution, long tails at higher forces could result in rare FP mechanical switching events occurring exclusively at very high load magnitudes.

For the constant magnitude loading profile, we used the simplifying assumption that all MTSs in a single population (corresponding to a measured pixel) are each engaged and loaded to the same load magnitude and duration values. However, MTSs within single ensembles could experience variation in loading. For instance, mixed populations of engaged/loaded and disengaged/unloaded talin proteins have been reported [S39]. In this case, each MTS will have a unique $E_0(F)$, meaning E_{app} and S_{app} must be computed directly from raw three channel FRET intensities (Equations 12-17), as was done for the constant loading rate simulations. An implication of sub-ensemble load variation is that MTSs under higher load magnitudes and longer load durations will preferentially undergo FP mechanical switching. This highlights that the presence of FP mechanical switching is likely to impact estimation of load magnitude from E_{app} for all cases of acceptor and/or donor mechanical switching, i.e. not just for acceptor mechanical switching as would already be expected for a system with excess donors. However, we do not expect the trends for detecting acceptor and/or donor mechanical switching reported here to be affected by this.

Lastly, we assumed that the entire load applied across the MTS is felt by both FPs, consistent with both FPs being in series in the line of loading, and that mechanical switching of the two FPs are independent processes. This ignores possible changes to the applied force caused by deformations or unfolding of one FP, as well as potential state-dependent interactions between the FPs.

2. Sensitized emission-based FRET measurements of MTS populations containing mechanically switched FPs

Next, we discuss assumptions and limitations related to measurements of FRET-based MTSs. First, to determine the signal contribution for each sensor state in three channel sensitized emission-based FRET measurements, we made assumptions about the effect of FP mechanical switching on the photophysical properties of FPs. To our knowledge, forced-induced changes in the excitation or emission wavelengths of FPs have not been described. Therefore, we assumed that donor FPs that have undergone mechanical switching cannot be excited by any excitation light in the optical system, and that acceptor FPs that have undergone mechanical switching cannot be excited by any excitation light in the optical system and also cannot accept energy from donor FPs. If this assumption is not met, a substantially more complex formalism is needed.

Furthermore, the FRET Efficiency-force relationship for sensors in the D1A1 state was modeled according to the original TSMod, mTFP1-$(GPGGA)_8$-mVenus, to facilitate comparisons to experimental data elsewhere in this paper using this module. However, the framework here can be applied immediately to TSMods based on other FPs and other genetically encoded FRET-based MTS using calibrated, unstructured tension sensing elements (e.g. repeats of GGSGGS [S2]), whose FRET-force relationships are loading rate-independent and have no hysteresis [S40]. Additionally, the framework should also be adaptable to threshold-like tension sensing elements that operate at or near equilibrium with calibrated FRET-force relationships that are loading rate-independent and have no hysteresis, such as those based on a single ultra-fast unfolding/refolding transition (e.g. HP35 and HP35st [S41]). In contrast, the framework is not readily applicable for tension sensing elements exhibiting loading rate-dependence or hysteresis.

Regarding the inability to make quantitative measurements of molecular tension magnitude in the presence of FP mechanical switching, we focused on the effects of FP mechanical switching on E_{app}, i.e. that $E_{app} \neq E_0$ in the presence of any acceptor mechanical switching. In addition to this effect, a second way in which FP mechanical switching can invalidate quantitative measurements of molecular tension magnitude is that, in the presence of variable loading in the cell, FP mechanical switching is more likely at higher versus lower tension magnitudes, which could bias measurements of tension magnitude distributions. This additional possibility further supports the guideline that, in the presence of any FP mechanical switching, quantitative measurements of molecular tension magnitude are not possible.

Lastly, there are limitations associated with very high levels of FP mechanical switching that may affect experimental data interpretation. First, if all sensors in some MTS ensembles (pixels) exist in the D0A0 state due to high levels of both acceptor and donor mechanical switching, some of the data will be undetectable and lead to an underestimation of FP mechanical switching in the system. Second, if there are especially low numbers of sensors in the D1A1 state, low signal-to-noise could cause uninterpretable E_{app} values in real experiments. However, it should be noted that these very high levels of FP mechanical switching do not pose a limitation to the mathematical model itself. The concentration of sensors in the D1A1 state mathematically remained non-zero in the ODE models (Sections III and V), and the parameter values explored in the stochastic models resulted in non-zero numbers of sensors in the D1A1 state (Sections IV and V). If the number of sensors in the D1A1 state reaches zero, E_{app} and S_{app} can still be computed directly from raw three channel FRET intensities (Equations S12-S17), as the simplified expressions for E_{app} and S_{app} (Equations S18-S19) become invalid.

VII. Interpretation of Experimental Data

Our experimental data, combined with modeling of a wide set of FP mechanical switching parameters (Figure S1 and Figure S5), suggest that mVenus undergoes mechanical switching *in cellulo* at lower load magnitudes and/or durations than would be expected for GFP in vitro [S8]. This is reflected by a reduction in one or both of the key parameters ($F_{1/2}$ and $k_{MS,0}$) for the acceptor FP in the MTS model that most closely resembled the *in cellulo* experimental data from this paper compared to the estimated values for GFP in vitro (Figure S5 and Table S2). Specifically, the $F_{1/2}$ values for acceptor FP in the MTS model (called $F_{1/2}^{A}$) that most closely resembled the *in cellulo* experimental data from this paper were 3 to 8 pN (with a base value of 5 pN), compared to the estimated value of 28.3 pN for GFP in vitro. The $k_{MS,0}$ values for acceptor FP in the MTS model (called $k_{MS,0}^{A}$) that most closely resembled the in cellulo experimental data from this paper were 0.316 to 3.16 1/s (with a base value of 1 1/s), compared to the estimated value of 0.33 1/s for GFP in vitro. The other two FP parameters (m and Δx_{MS}) were similar or

identical for acceptor FP in the MTS model compared to estimates for GFP in vitro. Overall, this suggests differences in the mechanical switching properties of GFP versus mVenus and/or differences in mechanical switching for single FPs in vitro versus FPs inside sensors *in cellulo*. At the same time, given the differences in the two experimental systems and that they are different FPs, the fact that the parameter estimates for GFP and mVenus are within a factor of 1 to 6 is notable.

VIII. Conclusions

In this supplemental note we developed and applied mathematical models of fluorescent protein (FP) mechanical switching in load-bearing proteins and MTSs. To investigate the process of FP mechanical switching in the context of protein loading in cells, we first modeled the reversible mechanical switching of a single FP integrated into a load-bearing protein and assessed the extent of FP mechanical switching across load magnitudes and durations estimated for protein loading in cells (Section II). This model indicated that FP mechanical switching can occur at the load magnitudes and durations estimated for protein loading in cells for a range of FP parameters ($F_{1/2} \leq F$ and $1/k_{ms,0} \leq \tau$), and that the process exhibits sensitivity to both load magnitude and duration. Next, to assess how FP mechanical switching affects FRET-based MTSs, we extended the model of FP mechanical switching to an MTS containing a donor and an acceptor FP (Section III). Using three channel FRET measurements analogous to experimentally accessible readouts, we developed and applied a framework for detecting FP mechanical switching in MTSs. We found that acceptor mechanical switching has a unique up/left slanting (E_{app}, S_{app}) signature that is robust to FP mechanical switching parameters and can be distinguished from force-independent acceptor loss-of-function. Donor mechanical switching has a unique down/left (E_{app}, S_{app}) signature that is robust to FP mechanical switching parameters and can be distinguished from force-independent donor loss-of-function. Both acceptor and donor FP mechanical switching signatures remain detectable in the presence of lower levels of mechanical switching in the other FP. Also, the (E_{app}, S_{app}) signature for FP mechanical switching in MTSs are sensitive to changes in both load magnitude and duration, and they respond to these loading parameters differently. To facilitate the data visualization, we conducted simulations that account for phenomena expected in real experimental data, including subcellular and cell-to-cell variation in protein loading dynamics and intrinsic noise in FP mechanical switching (Section IV). These data provide unique data signatures for comparison to experimental data. Lastly, consistent with the effects of loading dynamics on FP mechanical switching, we also demonstrate that FP mechanical switching is sensitive to force-sensitive bond dynamics and changes in loading rate (Section V), both of which are thought to underly stiffness sensing by FAs [S7]. Overall, our model of FP mechanical switching in MTSs establishes a framework for the detection of FP mechanical switching in MTSs. Using this framework, existing and new MTSs can be assessed for the existence of FP mechanical switching, which should become a new step in the development and interpretation of all MTSs. Furthermore, as FP mechanical switching in MTSs is sensitive to various aspects of protein loading dynamics, we expect that FP mechanical switching could be leveraged in the to probe force-sensitive protein function in the cellular context.

Note S2: Steered Molecular Dynamics Simulations of FPs, related to Figures 4 and S16-S18

I. Introduction

Our experimental findings suggest that mVenus has a lower mechanical stability than mTFP1. As an independent means of testing this, we performed steered molecular dynamics (SMD) on the two FPs.

II. Methods

Structures of mTFP1, mVenus, and αGFP were all obtained using AlphaFold [S42]. SMD simulations were prepared on a laptop computer using the QwikMD plugin [S43] of VMD 1.9.4a53 [S44]. Default "Easy Run" settings were used (T=27 °C, 0.15 mol/L salt concentration, and implicit solvent). The C-terminal residue was selected as the pulling residue, and the N-terminal residue was selected as the anchoring residue. The prepared simulation files were then transferred to the Duke Compute Cluster (DCC) at Duke University. Each simulation was then run on the DCC on 24 cores with 2GB of RAM per core. The completed simulation results were then transferred back to a laptop computer and re-loaded in VMD. Force-extension curves were calculated within the "Advanced Analysis" tab of the QwikMD plugin and subsequently analyzed using MATLAB 2020b. All simulation results were visually inspected to ensure that beta-strand pullout occurred within the simulation. The unfolding force for each simulation was characterized as the maximum force between the initial timepoint and the user-identified timepoint at which the first beta strand was pulled out of the beta barrel. Visual snapshots were prepared in VMD. The initial state (i) snapshot was selected as a very early timepoint, the Δα snapshot was chosen as a timepoint just before the maximum force values shown via red circles in Figures S16-S17, and the Δαβ snapshot was selected as a timepoint where the force was close to zero and the full removal of one β strand from the β-barrel could be clearly seen.

III. Results

We performed SMD on FPs using an implicit solvent at pulling speeds ranging from 0.3 to 10 nm/ns using the QwikMD plugin of the Visual Molecular Dynamics software [S44]. Simulations started with a relaxed FP structure at zero-force, and then pulled the N- and C-termini of the FP apart until at least one beta strand was pulled out of the FP's beta barrel. Rupture force was defined as the maximum force experienced by the FP before full pullout of the first beta-strand.

To validate our approach, we first simulated mechanical unfolding of αGFP, which has previously been studied using SMD by Saeger et al. [S45] as well as by experimental and computational means in other studies [S8, S10]. The αGFP simulations had an average maximum rupture force of 412±64 pN (Figure S16 and Movie S1), which resembles rupture forces obtained via SMD on similar timescales in prior work [S45, S46]. Note that it is typical for force estimates obtained from SMD to be higher by roughly an order of magnitude than experimental estimates [S8, S10] because the pulling speeds used in SMD are much higher (~nm/ns) than typical experimental pulling speeds (~nm/ms), and molecular unfolding is a stochastic, time-dependent process. Such high SMD pulling speeds are necessary because MD simulations performed with readily accessible computational resources can generally only access ns timescales.

We then simulated mechanical unfolding of mTFP1 and mVenus (Figure S17 and Movies S2-S3). Consistent with our experimental results, mTFP1 exhibited a significantly higher (p = 0.047, paired T-test) maximum force (409±61 pN) than mVenus (340±39 pN) (Figure S18). Notably, despite large differences in

primary sequence between the two FPs, the same structural transitions occurred, albeit at different average forces. In both cases, the FP's handle was unfurled (called the Δα state based on prior work [S10]), followed by the removal of the FP's N-terminal beta-strand (called the Δαβ state based on prior work [S10]).

Note S3: Supporting Tables for Statistical Tests, related to Figures 4-7

Table S5. P-value from Wilcoxon Rank Sum Test for ABDTS and ABDTL in Live Condition in Figure 4, related to Figure 4.

Data were considered not normal, so the two samples were compared by the Wilcoxon Rank Sum Test.

Level	- Level	p-Value
ABDTS_Live_None	ABDTL_Live_None	<.0001

Table S6. P-value from Wilcoxon Rank Sum Test for ABDTS and ABDTL in Fixed Condition in Figure S15, related to Figure S15.

Data were considered not normal, so the two samples were compared by the Wilcoxon Rank Sum Test.

Level	- Level	p-Value
ABDTS_Fix_None	ABDTL_Fix_None	<.0001

Table S7. P-values from Steel-Dwass Test for ABDTS and ABDTL Data in Figure 5, related to Figure 5.

Data were considered not normal and therefore were compared with a Kruskal-Wallis test (non-parametric one-way ANOVA on ranks). The Kruskal-Wallis test was significant (p<.0001), so Steel-Dwass non-parametric multiple comparisons test was conducted.

Level	- Level	p-Value
ABDTS_Fix_DMSO	ABDTL_Fix_DMSO	<.0001
ABDTS_Fix_DMSO	ABDTL_Fix_LatA	<.0001
ABDTS_Fix_LatA	ABDTL_Fix_DMSO	<.0001
ABDTL_Fix_LatA	ABDTL_Fix_DMSO	<.0001
ABDTS_Fix_LatA	ABDTL_Fix_LatA	0.0546
ABDTS_Fix_LatA	ABDTS_Fix_DMSO	<.0001

Table S8. P-values from Steel-Dwass Test for VinTS Variants on Glass in Figure 6, related to Figure 6.

Data were considered not approximately normal and therefore were compared with a Kruskal-Wallis test (non-parametric one-way ANOVA on ranks). The Kruskal-Wallis test was significant (p<.0001), so Steel-Dwass non-parametric multiple comparisons test was conducted.

Level	- Level	p-Value
VinTS E1015A_Glass	VinTS_Glass	0.8863
VinTS I997A_Glass	VinTS E1015A E1021A_Glass	0.9578
VinTS E1021A_Glass	VinTS_Glass	0.0732
VinTS I997A_Glass	VinTS E1021A_Glass	0.0067
VinTS I997A_Glass	VinTS_Glass	<.0001
VinTS E1021A_Glass	VinTS E1015A_Glass	0.0003
VinTS E1015A E1021A_Glass	VinTS E1021A_Glass	<.0001
VinTS I997A_Glass	VinTS E1015A_Glass	<.0001
VinTS E1015A E1021A_Glass	VinTS_Glass	<.0001
VinTS E1015A E1021A_Glass	VinTS E1015A_Glass	<.0001

Table S9. P-value from Wilcoxon Rank Sum Test for VinTS Variants on PA Gels in Figure 7, related to Figure 7.

Data were considered not normal, so the two samples were compared by the Wilcoxon Rank Sum Test.

Level	- Level	p-Value
VinTS E1015A E1021A_PAGel	VinTS_PAGel	0.3266

Supplemental References

S1. Grashoff, C., Hoffman, B.D., Brenner, M.D., Zhou, R., Parsons, M., Yang, M.T., McLean, M.A., Sligar, S.G., Chen, C.S., Ha, T., and Schwartz, M.A. (2010). Measuring mechanical tension across vinculin reveals regulation of focal adhesion dynamics. Nature *466*, 263-266. 10.1038/nature09198.

S2. LaCroix, A.S., Lynch, A.D., Berginski, M.E., and Hoffman, B.D. (2018). Tunable molecular tension sensors reveal extension-based control of vinculin loading. Elife *7*. 10.7554/eLife.33927.

S3. Rothenberg, K.E., Scott, D.W., Christoforou, N., and Hoffman, B.D. (2018). Vinculin Force-Sensitive Dynamics at Focal Adhesions Enable Effective Directed Cell Migration. Biophys J *114*, 1680-1694. 10.1016/j.bpj.2018.02.019.

S4. Hoffman, B.D., Grashoff, C., and Schwartz, M.A. (2011). Dynamic molecular processes mediate cellular mechanotransduction. Nature *475*, 316-323. 10.1038/nature10316.

S5. Roca-Cusachs, P., Iskratsch, T., and Sheetz, M.P. (2012). Finding the weakest link: exploring integrin-mediated mechanical molecular pathways. J Cell Sci *125*, 3025-3038. 10.1242/jcs.095794.

S6. Hoffman, B.D., and Yap, A.S. (2015). Towards a Dynamic Understanding of Cadherin-Based Mechanobiology. Trends Cell Biol *25*, 803-814. 10.1016/j.tcb.2015.09.008.

S7. Elosegui-Artola, A., Trepat, X., and Roca-Cusachs, P. (2018). Control of Mechanotransduction by Molecular Clutch Dynamics. Trends Cell Biol *28*, 356-367. 10.1016/j.tcb.2018.01.008.

S8. Ganim, Z., and Rief, M. (2017). Mechanically switching single-molecule fluorescence of GFP by unfolding and refolding. Proc Natl Acad Sci U S A *114*, 11052-11056. 10.1073/pnas.1704937114.

S9. Wolfenson, H., Bershadsky, A., Henis, Y.I., and Geiger, B. (2011). Actomyosin-generated tension controls the molecular kinetics of focal adhesions. J Cell Sci *124*, 1425-1432. 10.1242/jcs.077388.

S10. Dietz, H., and Rief, M. (2004). Exploring the energy landscape of GFP by single-molecule mechanical experiments. Proc Natl Acad Sci U S A *101*, 16192-16197. 10.1073/pnas.0404549101.

S11. Bustamante, C., Chemla, Y.R., Forde, N.R., and Izhaky, D. (2004). Mechanical processes in biochemistry. Annu Rev Biochem *73*, 705-748. 10.1146/annurev.biochem.72.121801.161542.

S12. Finer, J.T., Simmons, R.M., and Spudich, J.A. (1994). Single myosin molecule mechanics: piconewton forces and nanometre steps. Nature *368*, 113-119. 10.1038/368113a0.

S13. Molloy, J.E., Burns, J.E., Kendrick-Jones, J., Tregear, R.T., and White, D.C. (1995). Movement and force produced by a single myosin head. Nature *378*, 209-212. 10.1038/378209a0.

S14. Footer, M.J., Kerssemakers, J.W., Theriot, J.A., and Dogterom, M. (2007). Direct measurement of force generation by actin filament polymerization using an optical trap. Proc Natl Acad Sci U S A *104*, 2181-2186. 10.1073/pnas.0607052104.

S15. Gardel, M.L., Sabass, B., Ji, L., Danuser, G., Schwarz, U.S., and Waterman, C.M. (2008). Traction stress in focal adhesions correlates biphasically with actin retrograde flow speed. J Cell Biol *183*, 999-1005. 10.1083/jcb.200810060.

S16. Buckley, C.D., Tan, J., Anderson, K.L., Hanein, D., Volkmann, N., Weis, W.I., Nelson, W.J., and Dunn, A.R. (2014). Cell adhesion. The minimal cadherin-catenin complex binds to actin filaments under force. Science *346*, 1254211. 10.1126/science.1254211.

S17. Huang, D.L., Bax, N.A., Buckley, C.D., Weis, W.I., and Dunn, A.R. (2017). Vinculin forms a directionally asymmetric catch bond with F-actin. Science *357*, 703-706. 10.1126/science.aan2556.

S18. Owen, L.M., Bax, N.A., Weis, W.I., and Dunn, A.R. (2022). The C-terminal actin-binding domain of talin forms an asymmetric catch bond with F-actin. Proc Natl Acad Sci U S A *119*, e2109329119. 10.1073/pnas.2109329119.

S19. Kong, F., Garcia, A.J., Mould, A.P., Humphries, M.J., and Zhu, C. (2009). Demonstration of catch bonds between an integrin and its ligand. J Cell Biol *185*, 1275-1284. 10.1083/jcb.200810002.
S20. Rakshit, S., Zhang, Y., Manibog, K., Shafraz, O., and Sivasankar, S. (2012). Ideal, catch, and slip bonds in cadherin adhesion. Proc Natl Acad Sci U S A *109*, 18815-18820. 10.1073/pnas.1208349109.
S21. Ferrer, J.M., Lee, H., Chen, J., Pelz, B., Nakamura, F., Kamm, R.D., and Lang, M.J. (2008). Measuring molecular rupture forces between single actin filaments and actin-binding proteins. Proc Natl Acad Sci U S A *105*, 9221-9226. 10.1073/pnas.0706124105.
S22. Yao, M., Goult, B.T., Chen, H., Cong, P., Sheetz, M.P., and Yan, J. (2014). Mechanical activation of vinculin binding to talin locks talin in an unfolded conformation. Sci Rep *4*, 4610. 10.1038/srep04610.
S23. Yao, M., Qiu, W., Liu, R., Efremov, A.K., Cong, P., Seddiki, R., Payre, M., Lim, C.T., Ladoux, B., Mege, R.M., and Yan, J. (2014). Force-dependent conformational switch of alpha-catenin controls vinculin binding. Nat Commun *5*, 4525. 10.1038/ncomms5525.
S24. Perez-Jimenez, R., Garcia-Manyes, S., Ainavarapu, S.R., and Fernandez, J.M. (2006). Mechanical unfolding pathways of the enhanced yellow fluorescent protein revealed by single molecule force spectroscopy. J Biol Chem *281*, 40010-40014. 10.1074/jbc.M609890200.
S25. Snapp, E.L. (2009). Fluorescent proteins: a cell biologist's user guide. Trends Cell Biol *19*, 649-655. 10.1016/j.tcb.2009.08.002.
S26. Chen, H., Puhl, H.L., Koushik, S.V., Vogel, S.S., and Ikeda, S.R. (2006). Measurement of FRET efficiency and ratio of donor to acceptor concentration in living cells. Biophys J *91*, L39-L41. 10.1529/biophysj.106.088773.
S27. Gates, E.M., LaCroix, A.S., Rothenberg, K.E., and Hoffman, B.D. (2019). Improving Quality, Reproducibility, and Usability of FRET-Based Tension Sensors. Cytometry A *95*, 201-213. 10.1002/cyto.a.23688.
S28. Coullomb, A., Bidan, C.M., Qian, C., Wehnekamp, F., Oddou, C., Albiges-Rizo, C., Lamb, D.C., and Dupont, A. (2020). QuanTI-FRET: a framework for quantitative FRET measurements in living cells. Sci Rep *10*, 6504. 10.1038/s41598-020-62924-w.
S29. LaCroix, A.S., Rothenberg, K.E., Berginski, M.E., Urs, A.N., and Hoffman, B.D. (2015). Construction, imaging, and analysis of FRET-based tension sensors in living cells. Methods Cell Biol *125*, 161-186. 10.1016/bs.mcb.2014.10.033.
S30. Ponti, A., Machacek, M., Gupton, S.L., Waterman-Storer, C.M., and Danuser, G. (2004). Two distinct actin networks drive the protrusion of migrating cells. Science *305*, 1782-1786. 10.1126/science.1100533.
S31. Rajagopalan, P., Marganski, W.A., Brown, X.Q., and Wong, J.Y. (2004). Direct comparison of the spread area, contractility, and migration of balb/c 3T3 fibroblasts adhered to fibronectin- and RGD-modified substrata. Biophys J *87*, 2818-2827. 10.1529/biophysj.103.037218.
S32. Trepat, X., Wasserman, M.R., Angelini, T.E., Millet, E., Weitz, D.A., Butler, J.P., and Fredberg, J.J. (2009). Physical forces during collective cell migration. Nat Phys *5*, 426-430. 10.1038/Nphys1269.
S33. De La Pena, A., Mukhtar, M., Yokosawa, R., Carrasquilla, S., and Simmons, C.S. (2021). Quantifying cellular forces: Practical considerations of traction force microscopy for dermal fibroblasts. Exp Dermatol *30*, 74-83. 10.1111/exd.14166.
S34. Gillespie, D.T. (1977). Exact stochastic simulation of coupled chemical reactions. The Journal of Physical Chemistry *81*, 2340-2361. 10.1021/j100540a008.
S35. Evans, E. (2001). Probing the relation between force--lifetime--and chemistry in single molecular bonds. Annu Rev Biophys Biomol Struct *30*, 105-128. 10.1146/annurev.biophys.30.1.105.

S36. Wolfenson, H., Yang, B., and Sheetz, M.P. (2019). Steps in Mechanotransduction Pathways that Control Cell Morphology. Annu Rev Physiol *81*, 585-605. 10.1146/annurev-physiol-021317-121245.
S37. Liu, J., Le, S., Yao, M., Huang, W., Tio, Z., Zhou, Y., and Yan, J. (2023). Tension Gauge Tethers as Tension Threshold and Duration Sensors. ACS Sens *8*, 704-711. 10.1021/acssensors.2c02218.
S38. Staple, D.B., Hanke, F., and Kreuzer, H.J. (2008). Dynamics of single-molecule force-ramp experiments: The role of fluctuations. Physical Review E *77*, 021801. 10.1103/PhysRevE.77.021801.
S39. Ringer, P., Weissl, A., Cost, A.L., Freikamp, A., Sabass, B., Mehlich, A., Tramier, M., Rief, M., and Grashoff, C. (2017). Multiplexing molecular tension sensors reveals piconewton force gradient across talin-1. Nat Methods *14*, 1090-1096. 10.1038/nmeth.4431.
S40. Ham, T.R., Collins, K.L., and Hoffman, B.D. (2019). Molecular Tension Sensors: Moving Beyond Force. Curr Opin Biomed Eng *12*, 83-94. 10.1016/j.cobme.2019.10.003.
S41. Fischer, L.S., Rangarajan, S., Sadhanasatish, T., and Grashoff, C. (2021). Molecular Force Measurement with Tension Sensors. Annu Rev Biophys *50*, 595-616. 10.1146/annurev-biophys-101920-064756.
S42. Jumper, J., Evans, R., Pritzel, A., Green, T., Figurnov, M., Ronneberger, O., Tunyasuvunakool, K., Bates, R., Zidek, A., Potapenko, A., et al. (2021). Highly accurate protein structure prediction with AlphaFold. Nature *596*, 583-589. 10.1038/s41586-021-03819-2.
S43. Ribeiro, J.V., Bernardi, R.C., Rudack, T., Stone, J.E., Phillips, J.C., Freddolino, P.L., and Schulten, K. (2016). QwikMD - Integrative Molecular Dynamics Toolkit for Novices and Experts. Sci Rep *6*, 26536. 10.1038/srep26536.
S44. Humphrey, W., Dalke, A., and Schulten, K. (1996). VMD: visual molecular dynamics. J Mol Graph *14*, 33-38, 27-38. 10.1016/0263-7855(96)00018-5.
S45. Saeger, J., Hytonen, V.P., Klotzsch, E., and Vogel, V. (2012). GFP's mechanical intermediate states. PLoS One *7*, e46962. 10.1371/journal.pone.0046962.
S46. Cheng, C.-L., Zhang, M.-Z., and Zhao, G.-J. (2014). Mechanical stability and thermal conductivity of β-barrel in green fluorescent protein by steered molecular dynamics. RSC Advances *4*, 6513-6516. 10.1039/C3RA42679C.